The Dissertation Committee for Meghan Jill McAteer
certifies that this is the approved version of the following dissertation:

Linear Optics Measurements in the Fermilab Booster and the CERN PS Booster

Committee:

Sacha Kopp, Supervisor

Karol Lang

Jack Ritchie

Roy Schwitters

Chris Sneden

Linear Optics Measurements in the Fermilab Booster and the CERN PS Booster

by

Meghan Jill McAteer, B.A.Art, B.S.Phy.

DISSERTATION

Presented to the Faculty of the Graduate School of

The University of Texas at Austin

in Partial Fulfillment

of the Requirements

for the Degree of

DOCTOR OF PHILOSOPHY

THE UNIVERSITY OF TEXAS AT AUSTIN

December 2014

To Cara, Patrick, Jane, Richard, and Nathan.

Acknowledgments

This document is the result of six years of incredibly difficult and equally rewarding work. It is the culmination of a journey which has taken a long time, on a crooked road.

I am deeply grateful to my advisor, Sacha Kopp, who taught me so much about all aspects of physics and played such a large role in my decision to follow this path. He always offered a clear perspective and unfailing support in the face of the many obstacles that arose along the way, and this would not have been possible without him.

I am also very fortunate to have been able to work closely with and learn from Eric Prebys and Mike Syphers at Fermilab and Christian Carli and Rogelio Tomás at CERN, whose insights and enthusiasm were always inspiring.

There are numerous people at Fermilab and CERN without whom this work would not have been possible, including, among many others, all of the operators and machine specialists. In particular, thanks to Kent Triplett, Salah Chaurize, Todd Sullivan, Craig Drennan, and Brian Hendricks at Fermilab, and to Bettina Mikulec and Alan Findlay at CERN, for their knowledge and patience in helping me figure out how to coax the information I needed out of those idiosyncratic machines.

Special thanks is due to Nick Evans; not only has he always been a

source of excellent conversation about physics or any other topic, but without his repeated help clearing bureaucratic hurdles at UT while I was out of the country, this degree quite literally would not have happened.

And finally, I am inexpressibly grateful to Nathan Sellers, who provided constant support and encouragement throughout the highs and lows of this long journey.

Linear Optics Measurements in the Fermilab Booster and the CERN PS Booster

Publication No. _____

Meghan Jill McAteer, Ph.D.
The University of Texas at Austin, 2014

Supervisor: Sacha Kopp

The future experimental programs both at FNAL and at CERN will have a strong focus on the search for new physics at the intensity frontier. In order to provide beams of unprecedented intensities to the various experiments at these labs, the booster accelerators in which the beams originate must perform far beyond their original design specifications. The optical properties of the booster accelerator lattices will need to be carefully controlled in order to deliver these high-intensity proton beams.

This thesis presents the results of linear optics measurements made with unprecedented precision in the FNAL Booster and the CERN PS Booster using LOCO and K-modulation techniques. In the FNAL Booster, corrections to the observed optics distortions were also successfully implemented. The implications of these results for future high-intensity operations are discussed.

Table of Contents

List of Figures

Chapter 1

High-intensity proton beams for fundamental physics research

Particle accelerators are used in a wide variety of fields, from fundamental physics research to more practical applications such as medical and materials sciences. Probing new frontiers in physics research requires constantly pushing the boundaries of accelerator capabilities. This chapter will give an overview of some of the demands placed on accelerators for physics at the intensity frontier and discuss some of the difficulties inherent in creating beams with such high brightness and intensity.

This chapter will also introduce the two machines studied for this thesis: The Booster synchrotron at FNAL, and the PS Booster synchrotron at CERN. Both of these machines have been in operation for over forty years and have been made to perform far beyond their original specifications, and upgrades to these machines are still underway in order to meet the ever-increasing demands placed on them by the physics experiments that they supply beam to. We will give a detailed discussion of the purpose of, the structure of, and the challenges faced by each of these machines.

1.1 Physics at the intensity frontier

The search for new physics involves observing particles which are created rarely, such as the Higgs boson, or which interact rarely with detectors, such as neutrinos. The amount of time for which an experiment must run in order collect enough events to make precise measurements of new particles can be considerable, and to make these sorts of experiments feasible is is necessary to minimize the run time by maximizing the number of interactions per time.

Figure 1.1 shows cross sections of various products of proton-proton collisions. The number of events per time in a collider, such as the LHC, is defined by the luminosity,

$$\mathcal{L} = f\frac{N_1 N_2}{4\pi\sigma_x\sigma_y} \tag{1.1}$$

where $N_1,\ N_2$ are the number of particles in the colliding beams, $\sigma_x,\ \sigma_y$ are the transverse sizes of the beam, and f is the frequency with which the two beams collide. The nominal annual integrated luminosity of the LHC is about $\mathcal{L} = 40\ fb^{-1}$ and the total Higgs cross section at 14 TeV is 57 pb [1], giving an annual Higgs production rate of about 2 million per year.

Figure 1.2 shows the expected integrated luminosity in the LHC over the next decade, as well as the amount of run time needed to reduce the statistical uncertainty of physics measurements by half. By the end of this decade, the amount of additional run time needed to double the precision of measurements will exceed ten years; without an upgrade to higher luminosity, the statistical gain from continuing to run the accelerator will become

marginal [2]. In order to exploit the full potential of the machine and keep the rate of scientific progress high, planned Hi-Luminosity LHC upgrades will increase the annual integrated luminosity to 250 fb^{-1}. Achieving this increase in luminosity requires careful control of the beam properties throughout the whole chain of accelerators that delivers beam to the experiments.

1.2 Preparation of high-intensity beams in an accelerator chain

Accelerating a proton beam to high energy must be done in stages by transferring the beam through a series of accelerators with increasing energy. A rule of thumb is that the energy can be increased by no more than a factor of twenty between when a batch of protons is injected into a machine and when it is extracted and passed to the next machine [4]. This limitation is due to the field quality in the magnets that are used to steer the beam, which must change strength proportionally to the beam momentum. Because the saturation properties of the steel are different at low and at high field for normal-conducting magnets, and eddy current and hysteresis effects are different at low and high field for superconducting magnets, the shape of the magnetic field produced by a magnet when the beam is injected with low energy would be distorted relative to the magnetic field produced by the magnet when the beam reaches its maximum energy. These small imperfections in the field quality of the magnets can make the beam less stable, leading to beam loss. In the past some machines, such as the Main Ring at Fermilab or the Proton Synchrotron at

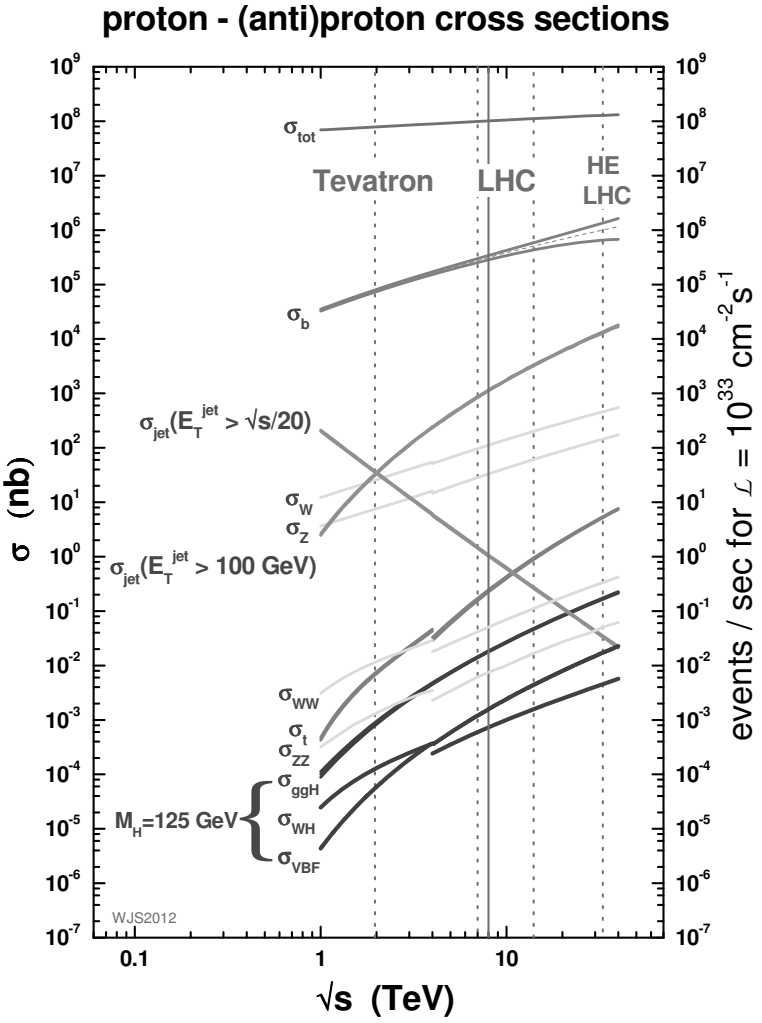

Figure 1.1: Cross sections for various products of proton-proton collisions as a function of center-of-mass collision energy. At $\sqrt{s} = 14TeV$ the total Higgs cross section is 57 pb, which corresponds to a production rate of about two million per year at the nominal annual integrated LHC luminosity of $\mathcal{L} = 40fb^{-1}$. Image from [3].

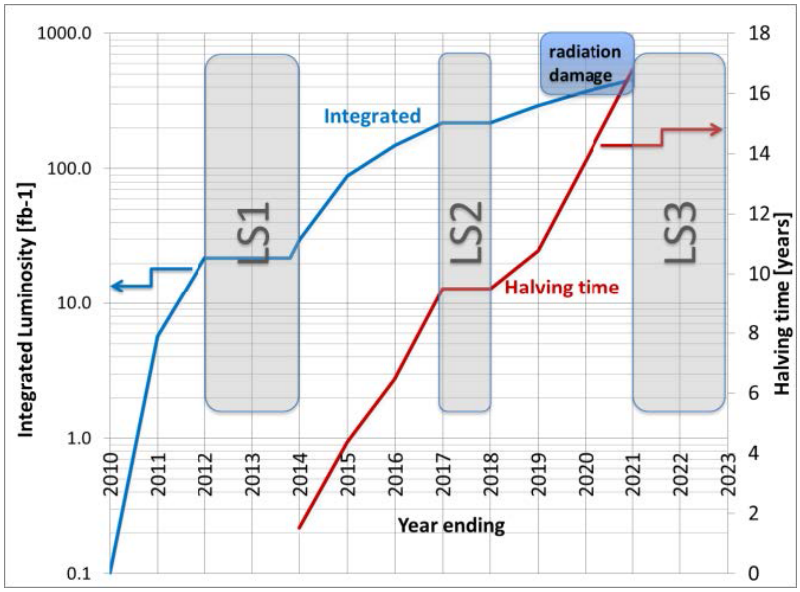

Figure 1.2: The blue line and the left-hand axis show the expected integrated luminosity in the LHC for the next decade. The red line and the right-hand axis show the running time that would be required to reduce the statistical uncertainty of measurements by half, assuming the given luminosity. By the end of this decade, the amount of additional run time needed to double the precision of measurements will exceed ten years; without an upgrade to higher luminosity, the statistical gain from continuing to run the accelerator will become marginal. Image from [2].

Figure 1.3: Arial view of the accelerator complex at FNAL. Protons are accelerated to 400 MeV in a linear accelerator (linac) and then injected into the Booster, where they are accelerated to 8 GeV. From the Booster they are either sent directly to the Booster Neutrino Beam (BNB) or transferred to the Main Injector for further acceleration. From the Main Injector they are transferred to either the Neutrinos at the Main Injector (NuMI) beamline or to fixed-target experiments. Within the next several years the main injector will also supply beam to more experiments that require high-intensity beam, including g-2 and Mu2e. To meet the demands of all of these experiments, the Booster's total proton throughput will have to be twice what it was at the end of the Tevatron's last run.

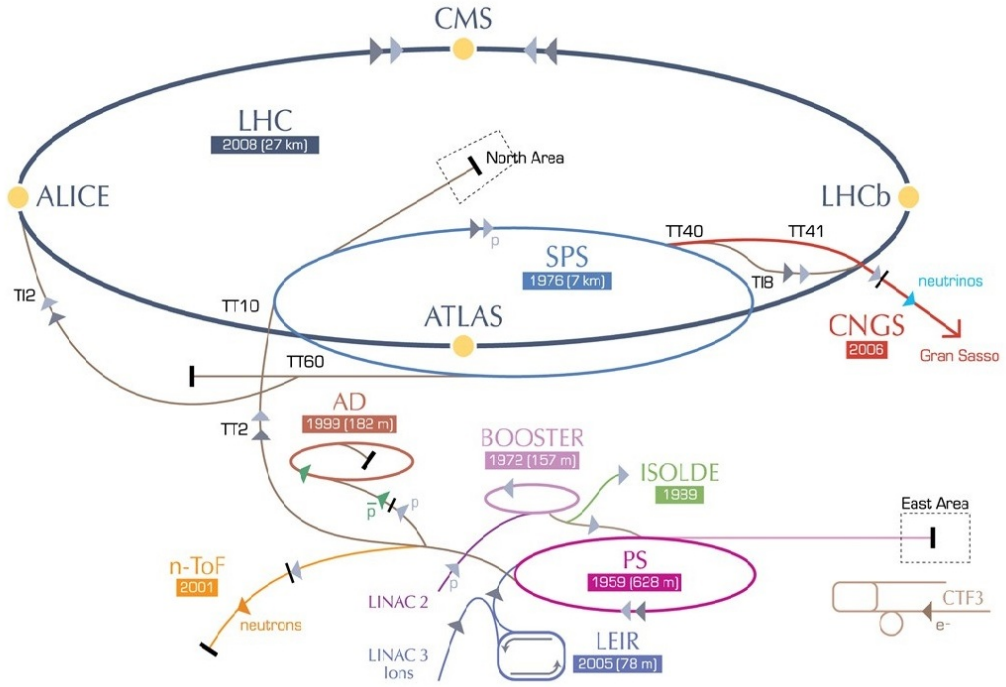

Figure 1.4: Schematic view of the accelerator complex at CERN. Protons are accelerated to 50 MeV in a linear accelerator (linac) before being injected into the PS Booster (PSB), where they are accelerated to 1.4 GeV. After acceleration in the PSB, protons are sent either to the ISOLDE radioactive ion beam facility or to the Proton Synchrotron (PS), where they are accelerated further. After acceleration in the PS, the beam is either sent to various fixed-target and neutrino experiments, or it is further accelerated through the Super Proton Synchrotron (SPS) and then transferred to the Large Hadron Collider (LHC). Upgrades to the LHC are planned which will increase its luminosity by a factor of ten, and to achieve this the beam intensity in the PSB will have to double while maintaining the current beam size and loss rate.

CERN, had energy increases larger than a factor of twenty, but this resulted in beam loss at low energy and a limitiation on the total number of protons that could be accelerated. To produce a beam with the energies and intensities currently required at FNAL or at CERN, the beams are accelerated through a series of machines with energy increases of no more than about a factor of fifteen.

Figure 1.3 show the accelerator complex at FNAL. Protons are accelerated to 400 MeV in a linear accelerator before being delivered to the Booster, where the energy is increased to 8 GeV. After extraction from the Booster, the beam is delivered either directly to the Booster Neutrino Beam (BNB) or passed to the main injector, where it is accelerated further before being delivered to the Neutrinos at the Main Injector (NuMI) beamline or to fixed target experiments. Within the next several years more high-intensity experiments will become operational, requiring even greater proton output from the Booster. Plans for the laboratory's future high-intensity experimental program demand that the total Booster throughput must roughly double relative to the levels at the end of the Tevatron run [5].

Figure 1.4 show the accelerator complex at CERN. Protons are accelerated to 50 MeV in a linear accelerator before being delivered to the PS Booster, where the energy is increased to 1.4 GeV. After extraction from the PS Booster, beam that is destined for the LHC will be accelerated in stages through two more machines, the Proton Synchrotron (PS) and the Super Proton Synchrotron (SPS). To reach the goal of increasing the luminosity in the

LHC by a factor of ten, it will be necessary to increase the intensity of the beam in the PSB by a factor of two with little allowable increase in the beam size or losses [6].

At each stage of the acceleration process there is the risk of introducing an irreversible growth in beam size, which would reduce the luminosity of the beam delivered to the experiments and increase the amount of time it takes to observe a given number of events. While Liouville's theorem states that the area in phase space occupied by an ensemble of particles is a constant of the motion, it is possible for the beam to undergo an apparent increase in phase space area due to filamentation. For every accelerator in the chain that produces high-energy beams, there will be strict requirements for how much beam size growth is acceptable. In many accelerator complexes the low-energy booster accelerator is the "bottleneck" which limits the intensity that can be achieved without allowing excessive beam size growth. In the next section we will discuss the challenges inherent in accelerating high-intensity beams in a booster accelerator, how particles in the beam are controlled and the problems that can arise as a result of poor control of the beam, and the steps one can take to prevent these problems.

1.3 Optimization of booster performance

The motion of particles in an accelerator is controlled using a system of magnets to bend and to focus the beam. The properties of this lattice of magnets in the accelerator are referred to as the optics, in analogy with a system

of lenses for focusing a beam of light. This system is similar to a harmonic oscillator, and ideally the trajectories of the particles in the machine will undergo stable oscillations around the design trajectory which passes down the center of the vacuum chamber that contains the beam. Any small imperfection in a magnetic field creates a perturbing force which acts periodically on the beam as it makes repeated passes around the machine, and if certain resonance conditions are met this perturbation can drive a large-amplitude oscillation. If this oscillation grows too large particles will strike the vacuum chamber or magnets. Transverse dynamics in an ideal machine, and the effects of magnetic field imperfections on the motion of particles in the beam, will be the subject of Chapter 2.

A major reason why booster accelerators present a restriction for accelerating intense beams is because of the effects of repulsive forces among particles within the beam, which are referred to as space charge forces. There are two effects to consider regarding interactions among particles within the beam: (1) the repulsive Coulomb force between particles, whose strength is independent of the energy of the particles, and (2) the attractive magnetic force such as is present between two current-carrying wires, which grows stronger as the beam energy increases. When the beam energy is low, as it is in a booster accelerator, the repulsive Coulomb force is dominant, and particles in the beam experience highly nonlinear space charge forces. These nonlinear space charge forces can exacerbate the effects from any small imperfections in the machine, leading to beam loss and beam size growth.

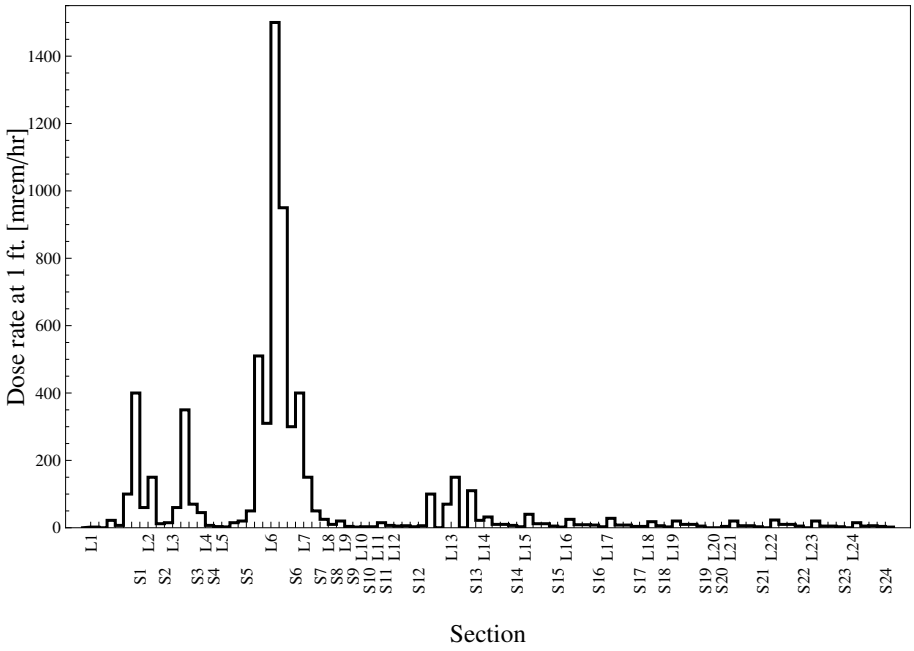

Figure 1.5: Residual radiation measured at various locations around the Booster ring at a distance of one foot from the machine. These measurements were made at the beginning of a maintenance access, about two hours after beam had stopped running, to assure the safety of personnel who would conduct maintenance or repairs. The hotspots correspond to high-loss regions where the beam is injected or extracted. The goal at FNAL is to keep the annual dose for personnel below 1500 mrem, so the doses received can be significant if repairs must be made near a hotspot.

In a booster accelerator 10% or more of beam particles can be lost, which is detrimental for two reasons. The first problem is simply the reduction in the number of particles that are successfully accelerated and then transferred to the next machine in the accelerator complex, which decreases the luminosity of the beam finally delivered to experiments. Secondly, each particle deposits energy into the material which it strikes, causing damage to equipment and creating radioactive isotopes that present a safety concern for personnel who must access the tunnel for maintenance or repairs.

Figure 1.5 shows the results of a tunnel radiation survey in the FNAL Booster in December 2011, which was performed at the beginning of a tunnel access in order to assure the safety of personnel who would carry out maintenance or repairs. The measurements were made about two hours after the beam was turned off. The hotspots correspond to areas of heavy beam loss in the machine near injection and extraction regions or near collimators, where beam losses are directed in a controlled fashion to an area that is well-shielded. The goal at FNAL is to keep the annual dose for personnel below 1500 mrem, so the doses received can be significant if repairs must be made near a hotspot. To prevent tunnel activation from increasing further when the Booster's total proton throughput is doubled within the next few years, it will be necessary to reduce the rate of beam loss.

One step to take in reducing beam loss and beam size growth is to carefully measure the optical properties of the accelerator, and then correct any imperfections in the magnet lattice which distort the optics and could

drive resonant growth in the amplitude of particles' oscillations around the ideal trajectory. In this dissertation we will discuss beam-based methods of optics measurements, in which the optical properties of the machine and the presence of magnetic field errors are deduced from observing the motion of the beam after we perturb it in specific ways. The details of these optics measurement methods will be the subject of Chapter 3. After measuring the optics, one can then compensate for any observed magnetic field errors using a set of corrector magnets that has been installed in the machine for this purpose. When the effects of these magnetic field imperfections have been compensated, if becomes possible to accelerate a more intense beam while still avoiding excessive losses or beam size growth. This is a necessary step in meeting ambitious goals for providing increased luminosity to high-energy, high-intensity physics experiments.

1.4 The FNAL Booster

This section will give a detailed overview of the structure and operation of the FNAL Booster, and of the hardware that is installed which can be used for diagnostics and for fine-tuning the machine. The results of optics measurements in the machine will be presented in Chapter 4.

The FNAL accelerator complex was shown in Figure 1.3. The output of the Booster has increased dramatically since it was commissioned 40 years ago. Figure 1.6 shows the daily and the integrated proton output from the Booster over the last twenty years [7]. The machine is expected to continue

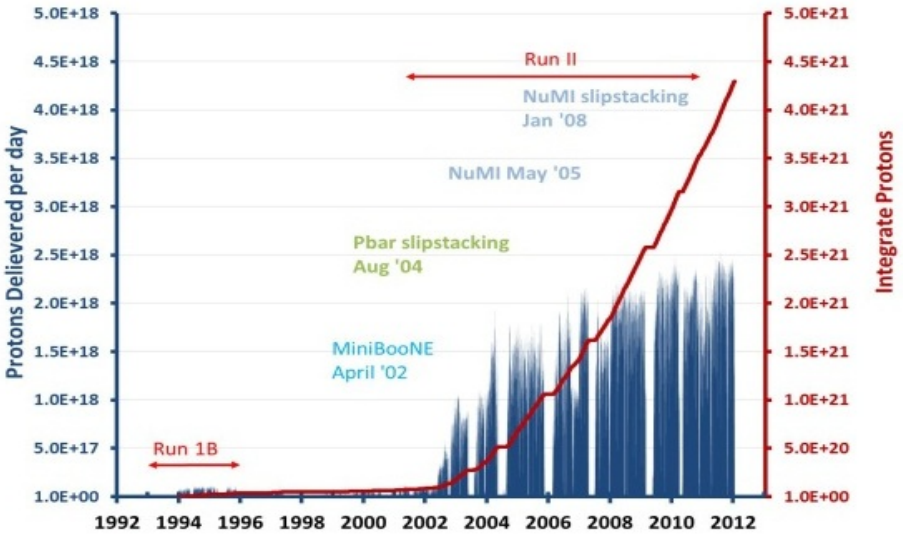

Figure 1.6: Proton throughput in the FNAL Booster during the last twenty years. The blue bars show the daily proton production, and the red line shows the integrated total number of protons delivered. Large increases in proton throughput have been made during the last decade to provide beam for various neutrino experiments at FNAL. To meet the needs of the lab's planned high-intensity experimental physics program for the next decade, the Booster's total daily throughput will have to be increased to double that achieved in 2012. Image from [7].

to improve its performance so that it may provide beam to meet the demands of the physics program at FNAL for at least the next decade [8]. To achieve, the total proton throughput of the machine will have to be doubled relative to the levels at the end of the Tevatron's last run [5]. This further improvement to the performance of a machine that is already operating so far beyond its originally intended capacity presents many challenges, including the need to control beam losses.

1.4.1 Structure of the machine

The FNAL Booster is a fast-ramping synchrotron which accelerates protons from 400 MeV to 8 GeV in 33 milliseconds. The circumference of the machine is 474 meters, and it is composed of 24 nearly-identical periods. The transverse motion of protons in the machine is controlled by a lattice of combined function magnets, which are magnets that produce a field that both bends the proton beam and also focuses particles within the beam. The magnets contain 28 turns of current-carrying wire wound around each pole of a steel core that is laminated to reduce the effects of eddy currents. Figure 1.7 shows the transverse profile of one of the magnets (top) and the magnetic field lines that are produced by the current in the wires (bottom). The poles are contoured to produce a field whose strength varies across the transverse aperture, so the force on a particle is proportional to its transverse position and a focusing effect results. Each of the 24 periods contains four combined function magnets, and the direction of the magnetic field gradient is oriented

to have a focusing effect on the beam in two of the magnets and a defocusing effect in the other two magnets, arranged in an F-D-D-F pattern. The overall effect of this arrangement of focusing and defocusing magnets is to focus the beam in both the horizontal and vertical planes, as will be discussed in detail in Section 2.1.

Figure 1.8 shows the measured magnetic field gradient as a function of transverse position (in inches) across the aperture of the magnet, relative to the strength of the gradient at the center of the aperture. The three traces, labeled I, II, and III correspond to measurements made at low, medium, and high field strengths. Ideally the gradient should be constant across the aperture, but in reality some deviation is inevitable. In the Booster the gradient varies by as much as five percent throughout the part of the aperture that can be occupied by the beam, depending on which part of the aperture the beam passes through. Efforts are made to ensure that the magnets are aligned as well as possible so that the beam passes through the center of the aperture, but some alignment errors are always present. Figure 1.9 shows a histogram of the horizontal, vertical, and rotational alignment errors measured for the 96 main magnets in the Booster [11]. The RMS transverse displacement errors are around two millimeters, and larger errors exist for some magnets. These alignment errors, the variability in field strength across the transverse aperture, and also as any small differences among the field in individual magnets resulting from the manufacturing processes can contribute to driving resonant amplitude growth in the transverse motion of particles in the beam.

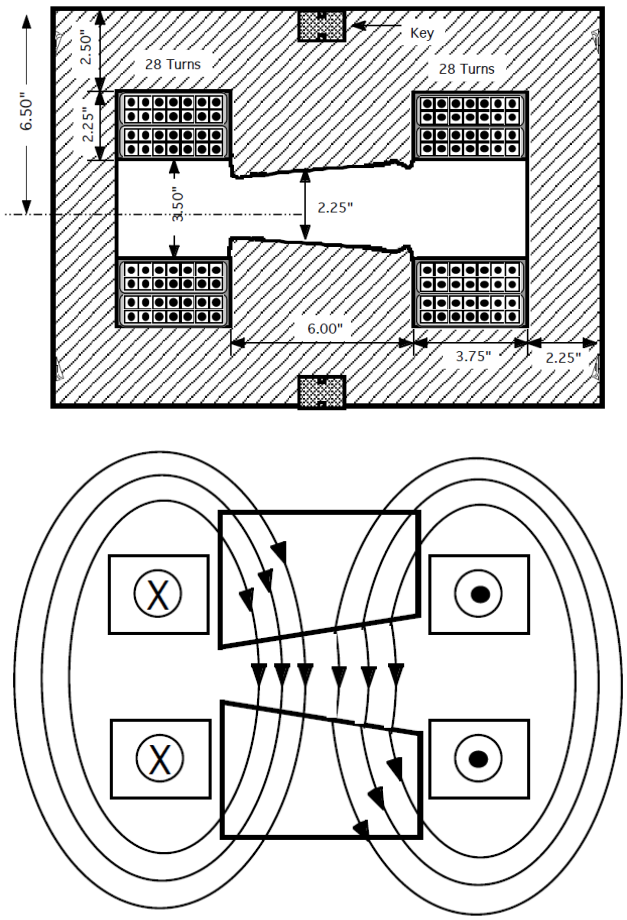

Figure 1.7: Drawing of a combined function magnet used in the Fermilab Booster (top) and of the magnetic field lines that are produced when current flows through the coils that are would around the poles (bottom). The body of the magnet is made of laminated steel to reduce eddy currents, with 28 turns of copper windings around each pole. There is no beam pipe passing through the center of the magnet; the entire gap is under vacuum. The pole faces are shaped to produce both a dipole field which bends the whole beam, and a quadrupolar field which focuses the particles within the beam. These types of magnetic fields are discussed in more detail in Section 2.1. Image from [9].

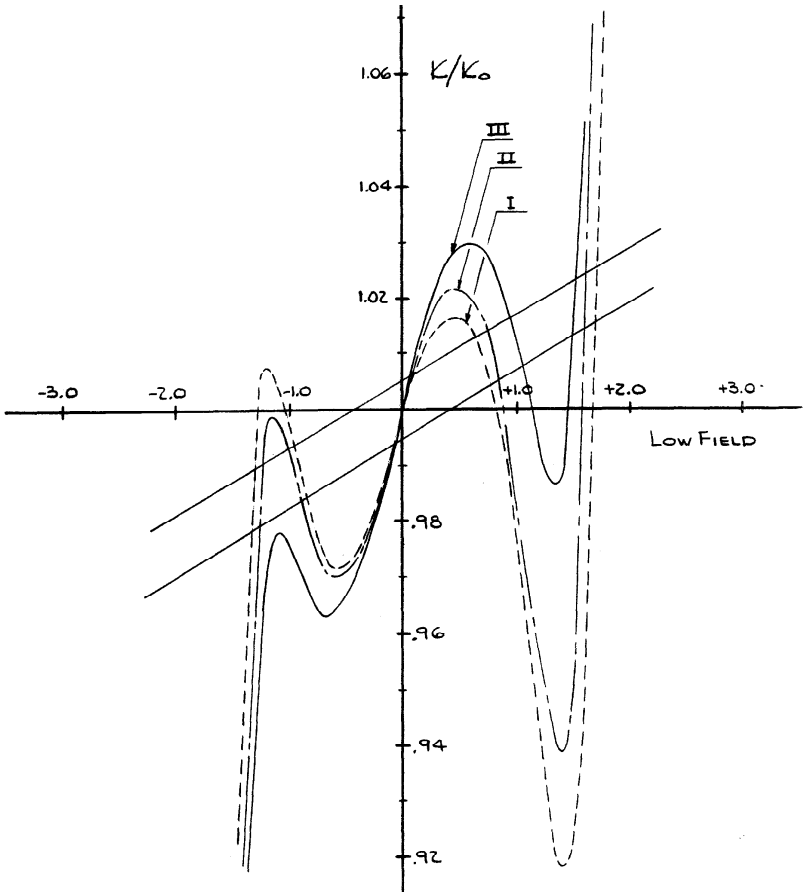

Figure 1.8: Measurement of the gradient in one of the Fermilab Booster's defocusing combined function magnets. The figure shows the ratio of the field gradient at varying radial positions, as a fraction of the gradient at $x = 0$. Ideally, the gradient should be constant at all radial positions. If the beam passes through far from the center of the magnet and experiences a field gradient significantly different from the design value, the transverse dynamics of the beam will be perturbed. Image from [10].

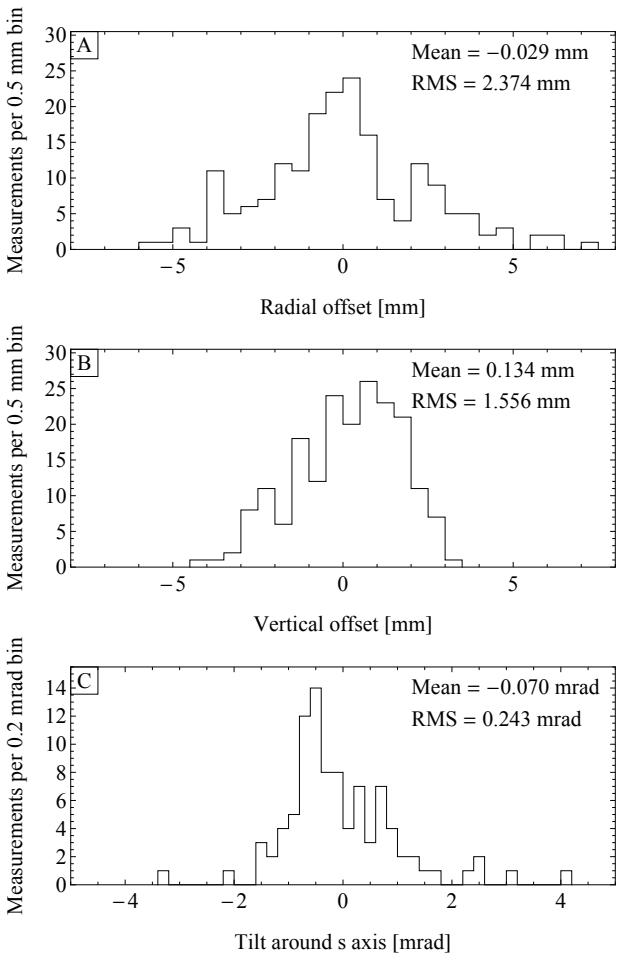

Figure 1.9: Measured alignment errors of magnet elements in the FNAL Booster, from 2005 tunnel survey. (A) shows the radial displacement of the ends of each of the 48 combined function magnets from the reference trajectory. (B) shows the vertical displacement of the ends of each combined function magnet from the reference trajectory. (C) shows the rotation of each combined function magnet along the longitudinal axis.

The Booster's combined function magnets are powered on a 15 Hz resonant circuit. Currently beam is accelerated through the machine only on about half of the fifteen cycles per second, but part of the plan for achieving higher total throughput includes upgrades that will allow beam to be accelerated during all fifteen cycles per second.

Beam is injected from the linac into the Booster using a scheme called H- injection, which allows for more intense beam in the machine. The linac accelerates H- ions rather than protons, and after injection into the Booster a set of three bending magnets is used to make a small localized bump in the orbit of the beam so that the ions pass through a stripping foil and the electrons are removed. After injection, these three magnets are turned off and the orbit bump is removed.

A batch of beam from the linac fills the circumference of the Booster, and this method allows for multiple batches of beam from the linac can be injected into the Booster to create beams of varying intensity. This scheme circumvents the conservation of phase space density described by Liouville's theorem, allowing the H- ions to be injected into the same phase space area that is occupied by the proton beam that is already circulating in the machine.

After acceleration the beam is extracted from the machine using a magnetic septum. During acceleration the beam is kept on the side of the septum that has no field, and after full energy is reached the beam is given a kick that moves it to the other side of the septum and into a transfer line. While the beam is being accelerated, a system of four bending magnets is used to

create a localized orbit bump that ensures that the beam stays far from the extraction septum. These bending magnets, called the dogleg magnets, have an unwanted side effect of distorting the optics of the machine, as will be seen in Chapter 4.

1.4.2 Hardware for diagnostics and corrections

Any accelerator contains hardware that can be used to observe the beam for diagnostic purposes, as well as magnets that can be used to correct imperfections in the machine's lattice. Here we describe the corrector magnet packages in the Booster as well as one of the diagnostic tools most relevant for optics measurements, the beam position monitor.

A new system of 48 corrector magnets, two in each of the 24 periods, was installed in the Booster during the last few years [12]. Each magnet consists of twelve steel poles that are wound with six sets of wire coils in such a way as to produce six independently-controllable field components in the same package: horizontal and vertical orbit correction dipoles for steering the beam, normal and skew quadrupoles for focusing the beam, and nonlinear sextupole fields for correcting higher-order perturbations. Each field component of each magnet can be independently powered with an arbitrary function of current vs. time. The magnets are designed to be strong enough and to slew quickly enough to provide complete and flexible control of the beam throughout its full energy ramp. These replaced an older system of corrector magnets that was less effective for correcting imperfections because they were weaker and

they were powered in groups, rather than each magnet being independently controllable. The greater flexibility provided by these new magnet packages allows for making more precise optics measurements than were previously possible, using methods that will be described in Chapter 3, and for correcting the observed imperfections in the machine optics.

Each of the Booster's corrector magnet packages also contains an integrated beam position monitor (BPM). The BPMs contain four parallel pickups, positioned at the upper, lower, outer, and inner areas of the beam pipe. When the beam passes through it induces a voltage on each of these pickups, which is proportional to both the charge of the beam and to the distance of the beam from the pickup. The horizontal and vertical transverse positions of the beam are calculated by comparing the difference in voltage between the horizontal and vertical pairs of pickups. The electronics for the pickups in the Booster are capable of recording the position of the beam on each turn that it makes around the machine, or of averaging the position of the beam on several consecutive turns and recording the average position of the closed orbit. There are three additional BPMs installed in the Booster besides the 48 in the corrector magnet packages, giving a total of 51 BPMs for each plane.

1.5 The CERN PS Booster

This section will give a detailed overview of the structure and operation of the CERN PS Booster, and of the hardware that is installed which can be used for diagnostics and for fine-tuning the machine. The results of optics

measurements in the machine will be presented in Chapter 5.

The CERN accelerator complex was shown in Figure 1.4. Like the FNAL Booster, the CERN PSB was built forty years ago and now performs far beyond its original design specifications. Figure 1.10 shows the proton intensity in the machine since its commissioning. Many improvements have been made throughout the years, allowing the machine to reach higher and higher intensities, and it now operates at about four times the design intensity. Plans for luminosity increases in the LHC will require the intensity to be increased by a further factor of two, while maintaining small beam size and keeping levels of beam loss low.

1.5.1 Structure of the machine

The CERN PSB operates at lower energy and has a slower ramp time than the FNAL Booster, accelerating protons from 50 MeV to 1.4 GeV in 525 milliseconds. To make up for its slower repetition rate, the PSB has an unusual structure in which four separate vertically-stacked rings accelerate beam simultaneously. When these four beams are extracted from the PSB they are recombined into a single beam before being transferred to the Proton Synchrotron.

The PSB has a circumference of 157 meters and is composed of sixteen nearly identical periods. The lattice structure is made up of separate bending magnets and focusing magnets, as opposed to the combined function magnet structure used in the FNAL Booster. Each period of the lattice contains two

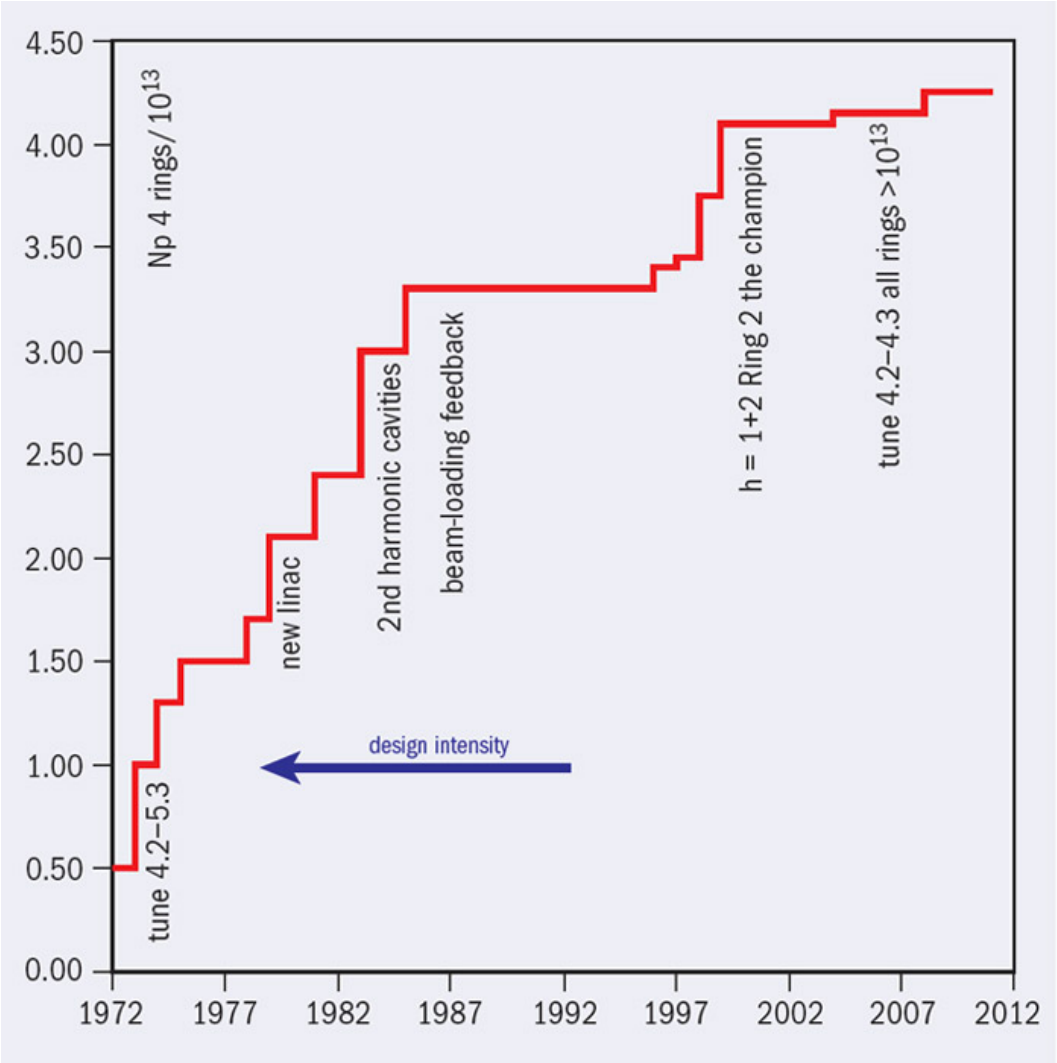

Figure 1.10: Beam intensity in the CERN PS Booster since its commissioning in 1970. The vertical axis shows the number of protons per batch $\times 10^{13}$. The machine is currently able to accelerate more than four times its design intensity of 1×10^{13} protons per batch. Image from [13].

bending magnets and a triplet of focusing magnets in an F-D-F configuration. Figure 1.12 shows a diagram of a PSB triplet magnet. Each magnet has four gaps, through which the beam in the four rings passes [14]. Figure 1.11 shows a histogram of the measured alignment deviations for the 32 bending magnets and 48 focusing magnets in the PSB. The RMS transverse displacement errors are about one millimeter, and larger errors exist for some magnets. These alignment errors, along with variability in field strength across the transverse aperture and any small differences among the field in individual magnets resulting from the manufacturing processes, can contribute to driving resonant amplitude growth in the transverse motion of particles in the beam.

Protons are injected from the linac into the PSB using a scheme referred to as phase space painting. The proton beam from the linac can't occupy the same phase space area as the beam that is already circulating in the PSB. Instead, each new batch from the linac is injected in such a way as to fill a larger and larger phase space area in the PSB. The intensity of the circulating beam can be increased by injecting more turns from the linac, but there is necessarily a corresponding growth in transverse beam size because the phase space density can't be increased. In a few years the injection will be upgraded to an H- injection scheme, similar to that used in the FNAL Booster. This upgrade will make it possible to produce more intense beams while maintaining a small beam size. The changes to the lattice structure necessary for the injection upgrade will introduce perturbations to the optics, so after the upgrades it will be especially important to measure and correct

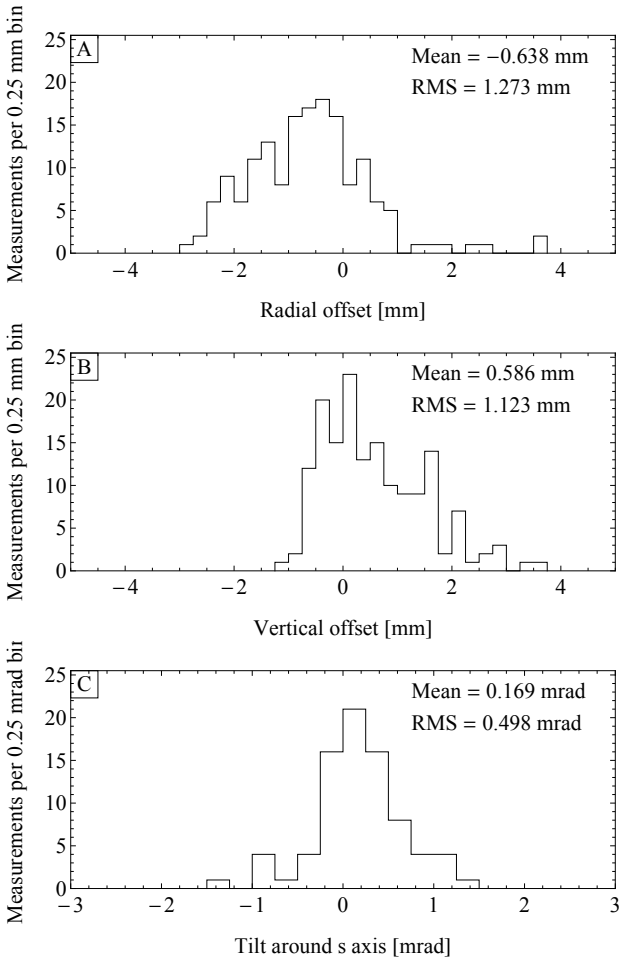

Figure 1.11: Measured alignment errors of magnet elements in the CERN PS Booster, from 2013 tunnel survey. (A) shows the radial displacement of the ends of each of the 32 bending magnets and 48 focusing magnets from the reference trajectory. (B) shows the vertical displacement of the ends of each bending magnet and focusing magnet from the reference trajectory. (C) shows the rotation of each bending magnet and focusing magnet along the longitudinal axis.

any optics distortions.

1.5.2 Hardware for diagnostics and correction

The PSB is equipped with sixteen BPMs for each of the transverse planes, located in each of the machine's sixteen periods. The system of corrector magnets in the PSB is somewhat less comprehensive than that available in the FNAL Booster. There are orbit corrector dipoles installed in thirteen of the sixteen periods in each ring, but each ring has only four pairs of quadrupole corrector magnets. Therefore only one of the optics measurement methods that will be discussed in Chapter 3 can be applied in the PSB, and the possibility to correct and observed optics distortions with the current set of corrector magnets is limited.

Further details about the hardware used for optics measurements can be found in Appendix 1.

1.6 Summary

In this chapter we have explained why brighter and more intense beams are needed for physics research and highlighted some of the difficulties inherent in producing such beams. We have presented the two machines that will be studied in the rest of this work, discussed the role of each in their respective experimental complexes, and described the structure of each machine and the diagnostic or corrective hardware available in each.

The next chapter gives a detailed treatment of transverse beam dynam-

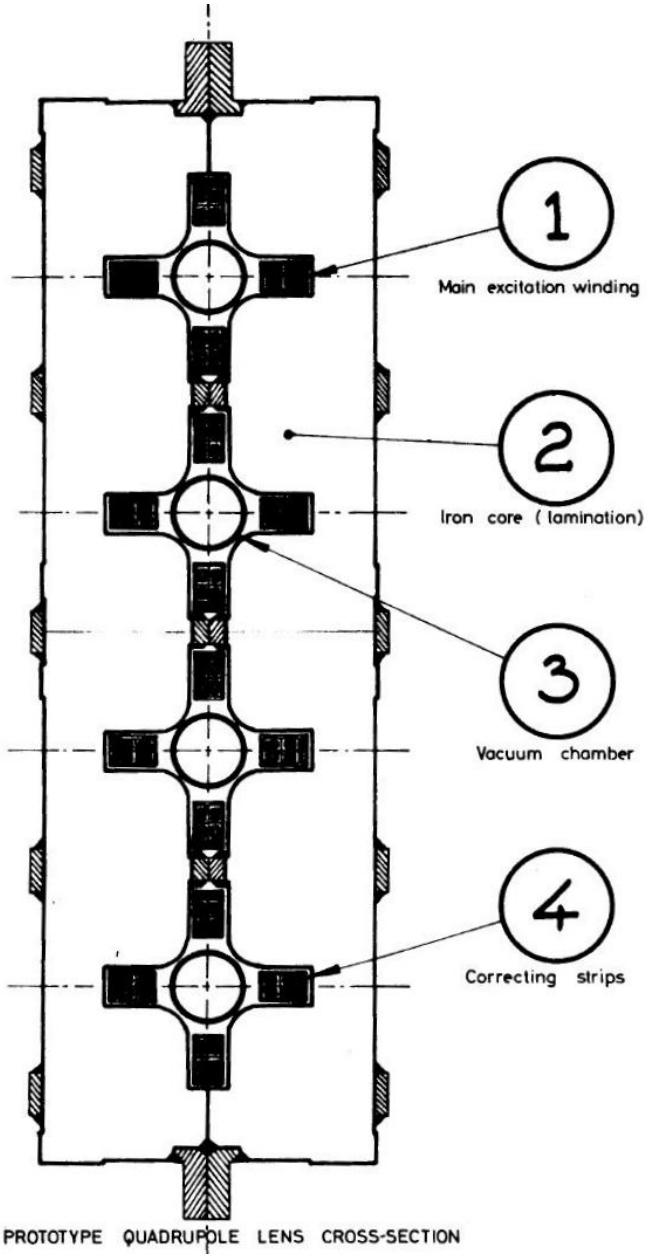

Figure 1.12: Drawing of a prototype for the focusing magnets in the CERN PSB. The magnet is composed of an iron core with four gaps, with current-carrying wires wound around each gap to create a quadrupolar field. A beam pipe passes through each of these gaps, and beam is accelerated concurrently in each of the four pipes. The PSB's dipole magnets have a similar four-gap structure. Image from [14].

ics in a synchrotron. This foundation will allow us to develop a quantitative understanding of some of the challenges involved in creating high-intensity, high-brightness beams which we discussed qualitatively in this chapter, as well as to explore the techniques that can be used for measuring and correcting optics perturbations.

Chapter 2

Transverse Beam Dynamics in a Synchrotron

The motion of particles in an accelerator must be carefully controlled in order to produce small and intense beams. Some divergence will always be present in the statistical distribution of particles in the ensemble, so if the beam were not focused its transverse size would quickly become too large to fit in the machine. This chapter will give an overview of transverse beam dynamics in a synchrotron, starting with a discussion of transverse magnetic fields and the effect that they have on the motion of charged particles. We will first examine the trajectories of particles by tracking them piecewise through a lattice of magnets, and then find a closed-form solution to the equations of motion by treating the accelerator as a modified harmonic oscillator.

In the last section we will move beyond the simplified picture of an ideal machine and discuss how small perturbations to the magnetic fields affect beam dynamics. In a real machine, in order to accelerate intense beams while avoiding beam loss or beam size growth, one must measure and possibly compensate for the effects of these imperfections. In Chapter 3 we will use the relationships between magnet errors and observable beam parameters to develop techniques for measuring the optical properties of the beam.

2.1 Magnetic fields in synchrotrons

In its simplest form, a synchrotron is made up of accelerating cavities which give energy to a proton beam and dipole magnets which bend the beam along a roughly circular orbit so that it passes repeatedly through the accelerating cavities. Figure 2.1 shows the trajectory of a particle as it passes through a bending magnet, which has a uniform magnetic field. A co-moving coordinate system is used here, in which the longitudinal coordinate s follows the ideal trajectory of the beam, and the horizontal and vertical coordinates x and y are perpendicular to s. The force on the particle due to the magnetic field is

$$\vec{F} = q\vec{v} \times \vec{B} = \frac{\gamma m \vec{v}^2}{\rho} \tag{2.1}$$

For small bending angles, $\Delta\theta \approx \frac{l}{\rho} = \frac{Bl}{(B\rho)}$, where B is the magnitude of the transverse magnetic field, l is the length of the magnet, and $(B\rho)$ is the magnetic rigidity, defined as [15]

$$(B\rho)[T \cdot m] = \frac{p}{q} = \frac{10}{2.9979} p[GeV/c] \tag{2.2}$$

In a real machine there is a statistical distribution in both the position and angle of particles in the beam, and no particle follows exactly along the ideal closed orbit. Figure 2.2 shows the closed orbit and the trajectory of a single proton as it oscillates around the ideal closed orbit. As in Fig. 2.1, the longitudinal coordinate s follows the ideal path of a particle around the machine, and the transverse coordinates x and y measure the radial and vertical

displacement of the particle from ideal path. The coordinates used for transverse momentum are derivatives of the transverse positions with respect to s: $x' = \frac{dx}{ds}$, and $x' = \frac{dx}{ds}$.

Magnetic fields beyond dipoles are needed to focus the beam, compensating for particles' deviations from the ideal trajectory. The magnet elements used in accelerators can be described using the notation of multipole expansion, in which an arbitrary transverse magnetic field is described as a sum of pure multipole components. The magnetic potential in a vacuum must satisfy the lapace equation, and the most general solution is the complex magnetic potential Ψ, defined as

$$\Psi = \sum_n \Psi_n = \sum_n (A_n + iB_n)(x + iy)^n \tag{2.3}$$

where x and y are the transverse coordinates, n is the order of the multipole component, A_n is a constant that defines the strength of the n^{th} normal multipole component, and B_n is a constant that defines the strength of the n^{th} skew multipole component [16]. The magnetic field lines for a given multipole are equipotentials of the the longitudinal component of the vector potential $A_s \equiv Re[\Psi_n]$. The pole face contours that produce the multipolar field lie along an equipotential of the the scalar potential $\phi \equiv Im[\Psi_n]$. Figure 2.3 shows the magnetic field lines and pole face shapes for the first two orders of multipoles. The skew field is essentially the same as the normal field rotated by $\frac{\pi}{2n}$ radians.

For the rest of this discussion, we will focus on the linear magnet ele-

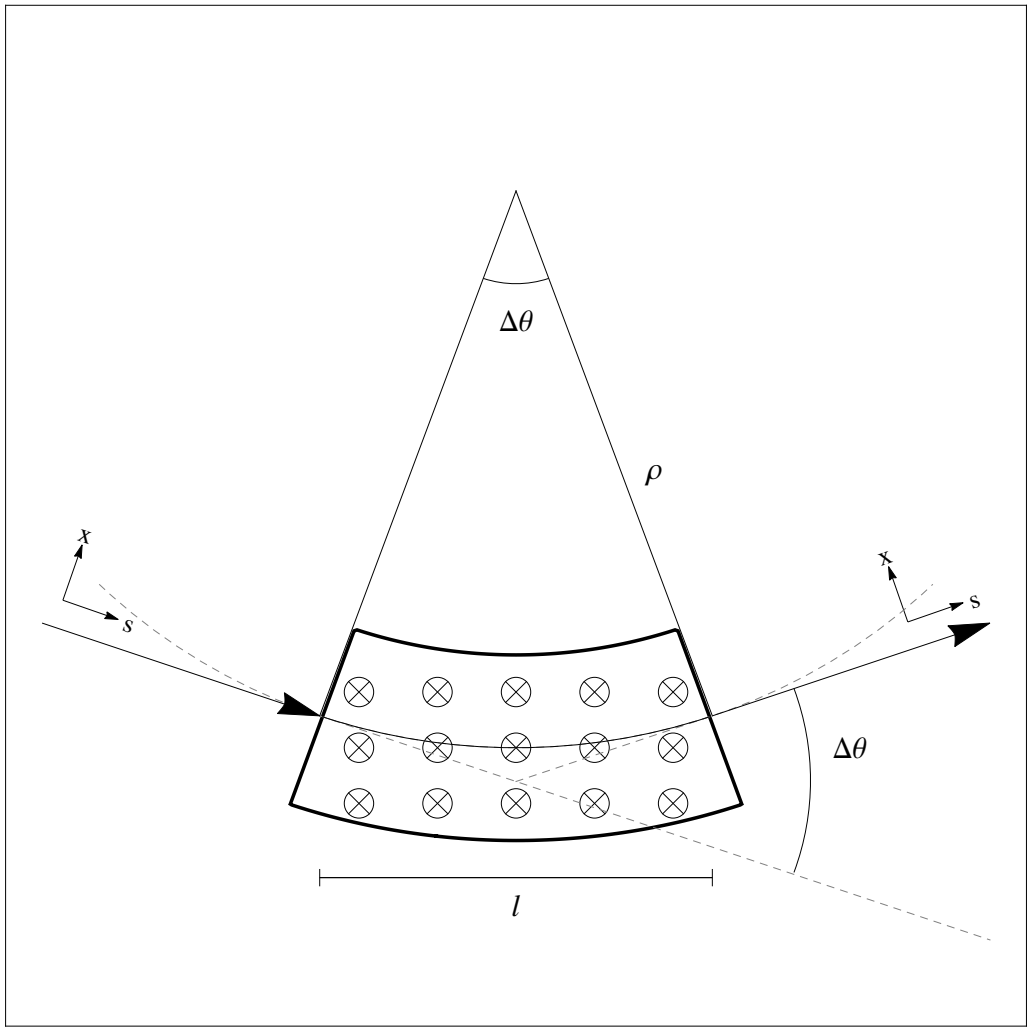

Figure 2.1: Trajectory of a particle passing through a uniform (dipolar) magnetic field, which is used to steer the beam along a roughly circular trajectory so that it passes many times through the accelerating cavities. For small bending angles, the angular deflection is proportional to the magnetic field integrated along the path of the beam through the magnet: $\Delta\theta \approx \frac{l}{\rho} = \frac{Bl}{(B\rho)}$ (see Eq. 2.1)

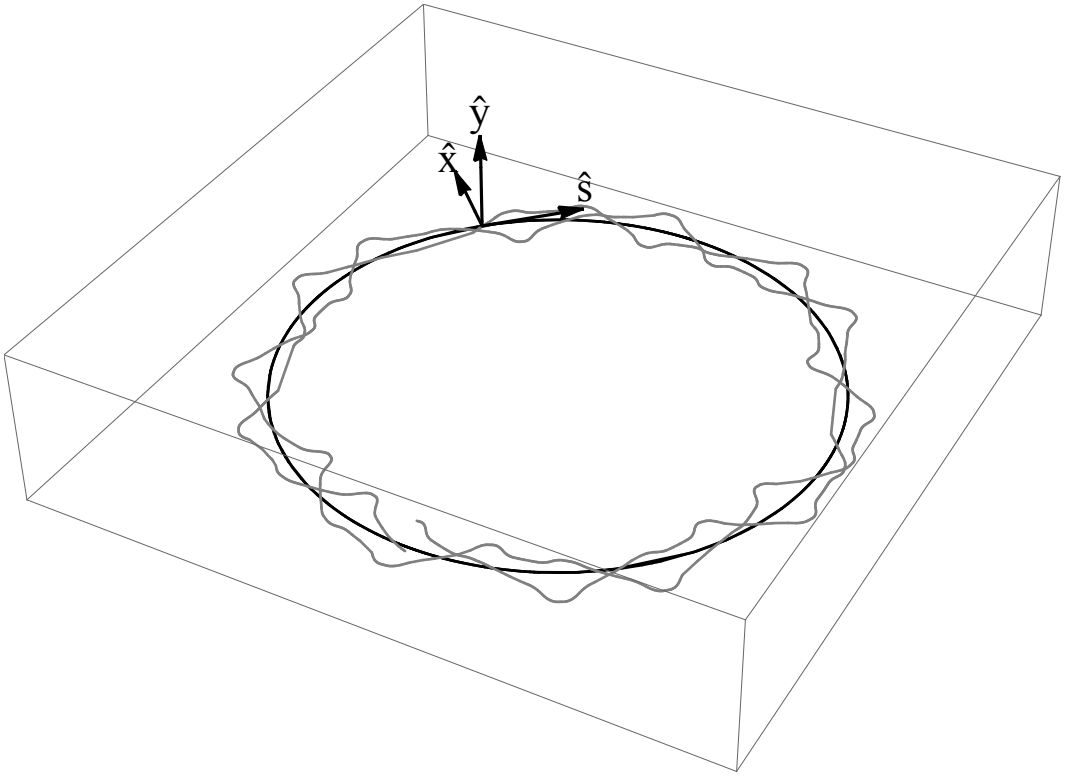

Figure 2.2: Horizontal trajectory of a proton beam in a synchrotron. The coordinate s follows along the beam's ideal closed orbit, the coordinate x describes the beam's radial displacement from the ideal trajectory, and the coordinate y describes the beam's vertical displacement from the ideal trajectory. The gray line is the ideal closed orbit, and the black line is the trajectory of a real particle in the machine, which oscillates around the ideal ideal closed orbit.

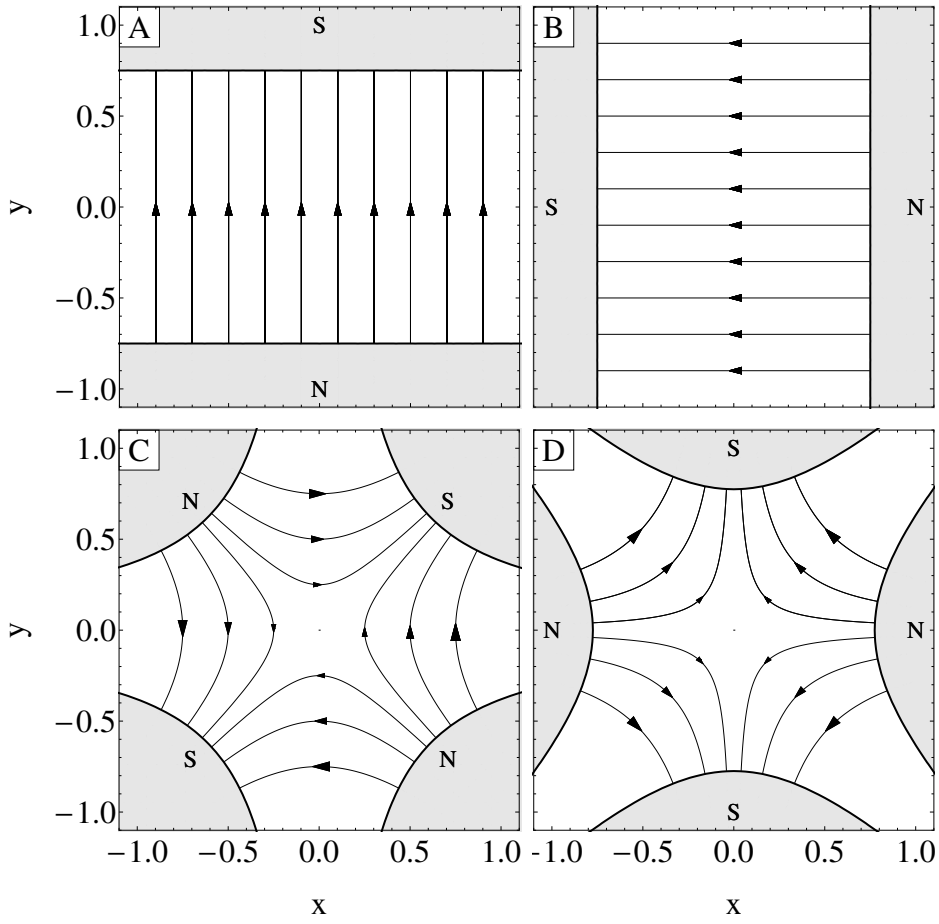

Figure 2.3: Pole face contours and magnetic fields for (A) normal (horizontal) dipole, (B) skew (vertical) dipole, (C) normal quadrupole, and (D) skew quadrupole magnet elements. The arrows indicate the direction and magnitude of the magnetic field. The magnetic field lines are equipotentials of the longitudinal vector potential A_s, and the pole face contours lie along equipotentials of the scalar potential ϕ (see Eq. 2.3).

ments (dipoles and quadrupoles). Figure 2.4 shows the horizontal trajectories of particles in a beam as they pass through a horizontal dipole magnet, which has uniform transverse field B_y, and through a normal quadrupole magnet, which has uniform gradient $B' = \frac{\partial B_y}{\partial x} = \frac{\partial B_x}{\partial y}$. The dipole bends all particles by the same angle, so the beam as a whole is bent. The quadrupole bends each particle proportionally to its transverse displacement, acting as a lens that focuses the beam in one plane and defocuses it in the other plane. The strength of a quadrupole is defined as

$$k_1 l \equiv \frac{1}{f} = \frac{B'l}{(B\rho)} \tag{2.4}$$

where f is the focal length, l is the length of the magnet, $B'l$ is gradient of the field integrated along the length of the magnet, and $(B\rho)$ is the magnetic rigidity.

2.2 Tracking a particle through a linear lattice

For a magnet lattice made up of only linear magnet elements (dipoles and quadrupoles), the transverse trajectory of a particle can be tracked using a map composed of transfer matrices. Each element in the lattice (dipole, quadrupole, or drift space) can be represented by a matrix M which relates the coordinates of the particle $\vec{z} \equiv (x, x', y, y')$ before and after passing through the element:

$$\vec{z}_{out} = M \cdot \vec{z}_{in} \tag{2.5}$$

When passing through a drift space, where no magnetic fields are

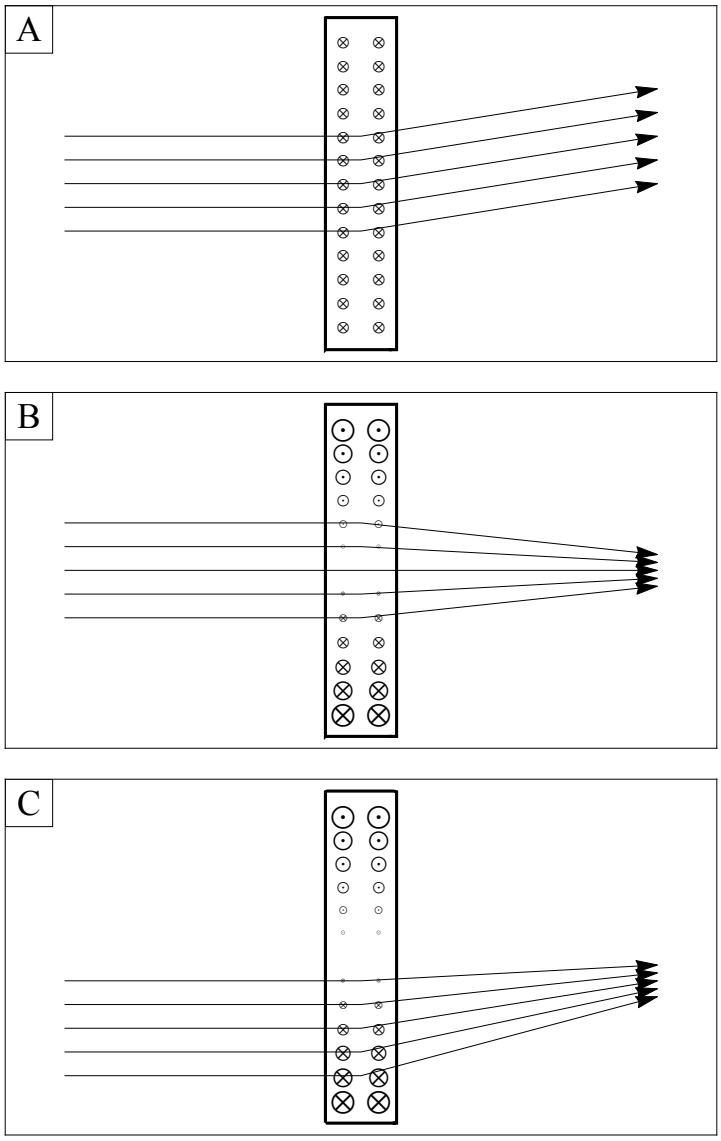

Figure 2.4: Horizontal trajectories of protons in a beam as they pass through (A) a thin dipole magnet, (B) the center of a thin quadrupole, and (C) the edge of a thin quadrupole. The magnitude and direction of the magnetic field are indicated by $\otimes$ and $\odot$. Passage through the dipole bends all beam particles by the same angle, passage through the center of the quadrupole focuses the beam, and passage off-center through the quadrupole both focuses and bends the beam.

present, the particle's angle is unaffected and the change in position depends on the initial angle, so the transfer matrix for a drift space of length L is

$$M_{drift} = \begin{pmatrix} 1 & L & 0 & 0 \\ 0 & 1 & 0 & 0 \\ 0 & 0 & 1 & L \\ 0 & 0 & 0 & 1 \end{pmatrix} \tag{2.6}$$

When passing through an infinitesimally thin quadrupole, the particle's position is unaffected and the change in angle depends on the transverse displacement, as was shown in Fig. 2.4. The transfer matrix for a thin quadrupole with strength $k_1 l$, which focuses the beam in the horizontal plane and defocuses the beam in the vertical plane, is

$$M_{quad} = \begin{pmatrix} 1 & 0 & 0 & 0 \\ -k_1 l & 1 & 0 & 0 \\ 0 & 0 & 1 & 0 \\ 0 & 0 & k_1 l & 1 \end{pmatrix} \tag{2.7}$$

The transfer matrix for a section of the lattice, or for the whole ring, is obtained by multiplying together the matrices for each individual element. For example, a common configuration of magnets in an accelerator is the focusing-drift-defocusing-drift (FODO) cell, and the transfer matrix for this set of elements is

$$M_{FODO} = M_{drift} \cdot M_{quadD} \cdot M_{drift} \cdot M_{quadF} \tag{2.8}$$

where M_{quadF} is the transfer matrix for a quadrupole which is focusing in the horizontal plane and defocusing in the vertical plane, M_{quadF} is the transfer matrix for a quadrupole which is defocusing in the horizontal plane and focusing in the vertical plane, and M_{drift} is the transfer matrix for the drift

space. Stable lattices can be designed using many other configurations besides FODO, such as the FNAL Booster's F-D-D-F structure or the CERN PSB's F-D-F structure.

Figure 2.5 shows a particle's (x, s) trajectory as it is tracked through fifty passes of one of the FNAL Booster's F-D-D-F lattice periods. After many passes, it becomes apparent that there is a maximum transverse excursion that the particle can make at a given longitudinal location, and the shape of the beam envelope becomes visible. If instead of tracking a single particle for many turns we tracked an ensemble of particles for one turn, the shape of the beam envelope would be the same. The shape of the beam envelope is proportional to the square root of a machine parameter called the beta function, and the size of the envelope depends on the initial conditions of the particles. The horizontal and vertical beta functions for one period of the FNAL Booster and one period of the CERN PS Booster are shown in figure 2.6. As expected, the horizontal beta function for the FNAL Booster has the same shape as the beam envelope in Fig. 2.5.

Figure 2.7 shows Poincare maps corresponding to the trajectories shown in Fig. 2.5. The points mark the (x, x') coordinates each time the particle passes through the first focusing or a defocusing quadrupole in the lattice. The particle's trajectory on each pass lies on an ellipse whose shape is determined by the focusing lattice and whose size is determined by the particle's initial conditions. If instead of tracking a single particle for many turns we tracked an ensemble of particles for one turn, the (x, x') coordinates for the ensemble

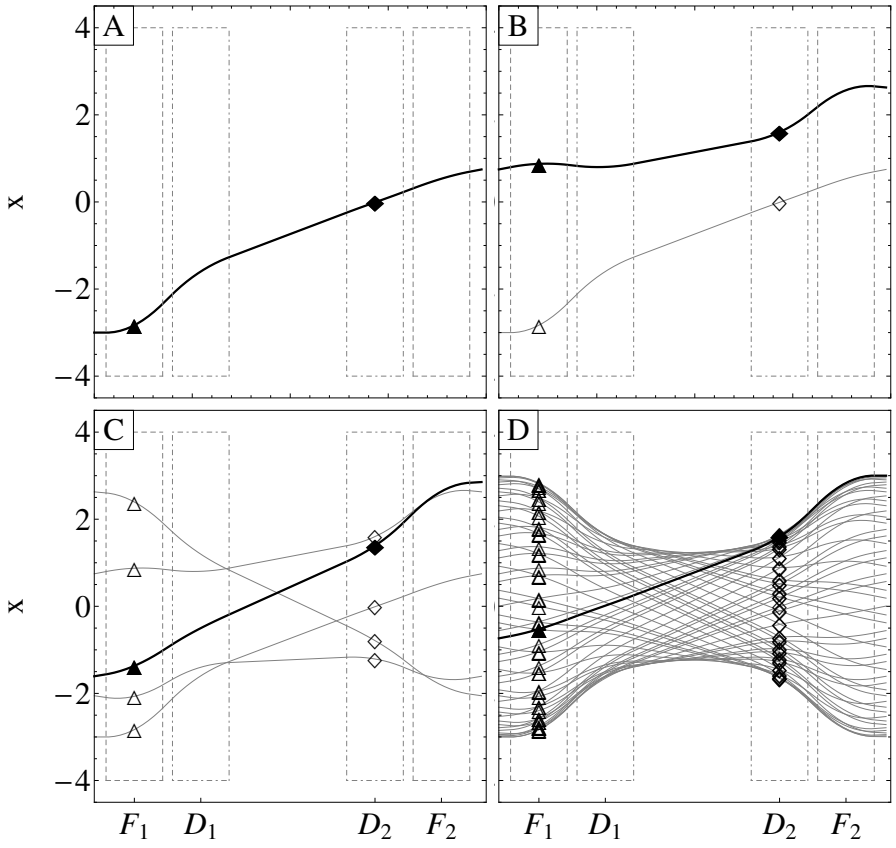

Figure 2.5: Trajectory of a particle after (A) one, (B) two, (C) five, and (D) fifty passes through one period of the FNAL Booster's F-D-D-F focusing lattice. The horizontal coordinate s is the longitudinal position of the particle along the reference trajectory, and the vertical coordinate x is the radial position relative to the reference trajectory. The diamonds and triangles show the position of the particle each time it passes two fixed longitudinal locations, and the particle's position in (x, x') phase space at these locations will be shown in Fig. 2.7. The shape of the beam envelope is described by the beta function, which is a property of the machine's focusing lattice structure, and the size of the envelope is determined by the initial oscillation amplitudes of the particles.

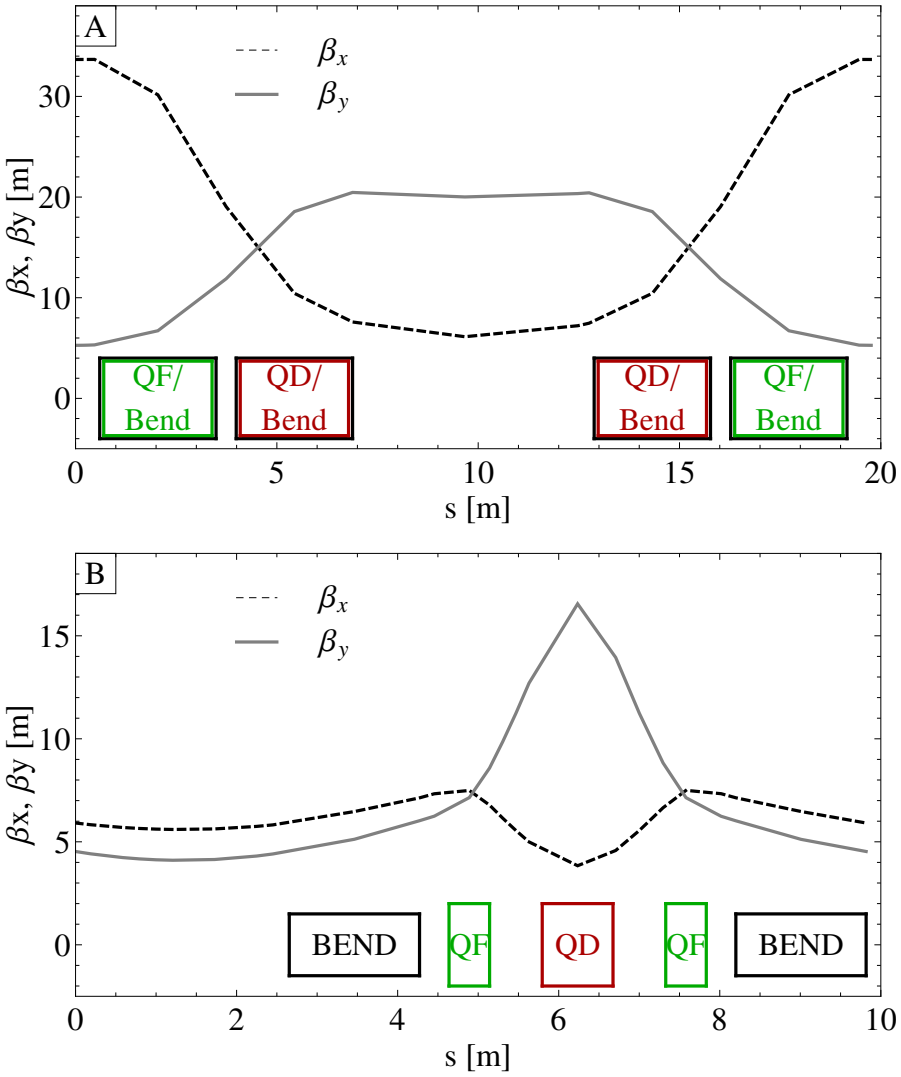

Figure 2.6: The magnet lattice structure and the beta functions for one period of (A) the FNAL Booster and of (B) the CERN PS Booster. The FNAL Booster is composed of focusing and defocusing combined function magnets (labeled "QF/Bend" or "QD/BEND) with an F-D-D-F structure in each period. The CERN PSB is composed of separate bending magnets (labeled "BEND") and focusing magnets (labeled "QF" or "QD") with a F-D-F focusing triplet structure in each period. The shape of the beam envelope is proportional to the square root of the beta function (see Fig 2.5).

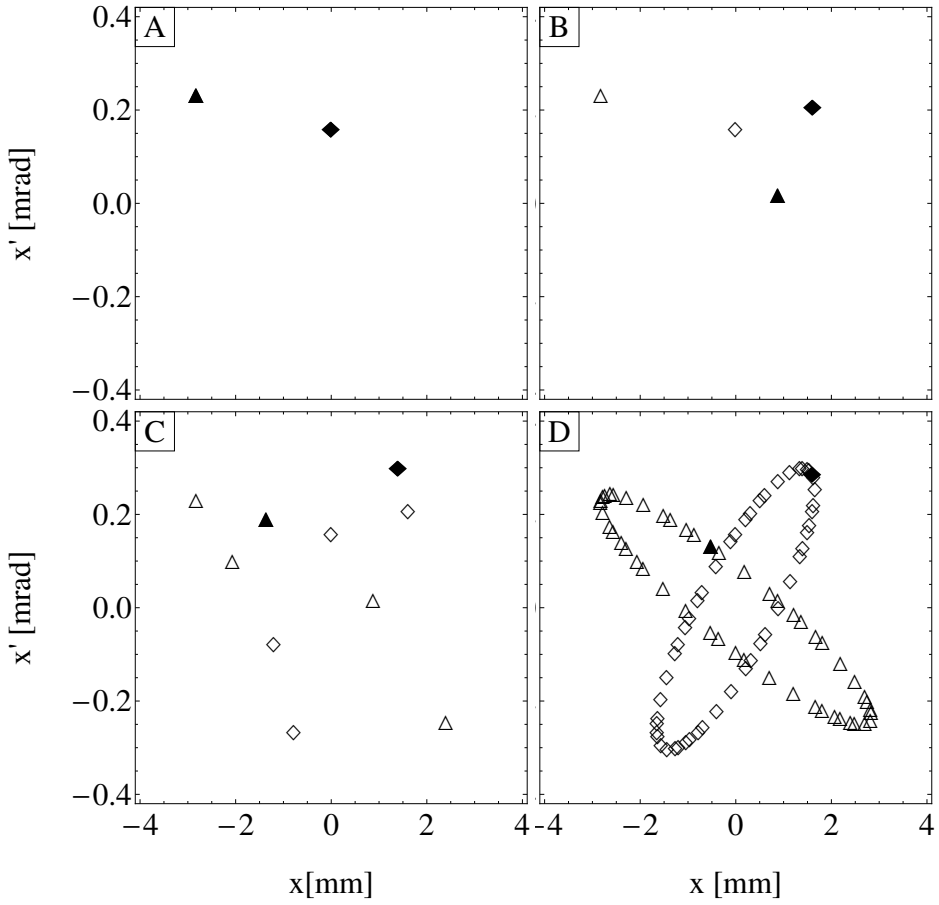

Figure 2.7: Poincare map showing the (x, x') coordinates of a particle after (A) one, (B) two, (C) five, and (D) fifty passes through one period of the FNAL Booster's F-D-D-F focusing lattice. The horizontal coordinate x is the radial position of the particle relative to the reference trajectory, and the vertical coordinate x' is the derivative of x with respect to the longitudinal coordinate s. These (x, x') coordinates correspond to the x, s trajectories shown in Fig. 2.5. The triangles mark the coordinates of the particle each time it passes through a focusing magnet F, and the diamonds mark the coordinates each time it passes through a defocusing magnet D. On every pass through a given longitudinal point, the particle's trajectory in x, x' phase space lies on an ellipse whose shape is determined by the focusing lattice, and whose size is determined by the particle's initial conditions. The coordinates of an ensemble of beam particles during a single turn also lie within an ellipse of this shape.

of particles would also lie within an ellipse of this shape. The beam parameter describing the size of the ellipse is called the emittance, which characterizes the initial distribution in phase space. The RMS emittance is defined as the average of the action of all particles in the beam, or, equivalently, as the area of the ellipse that encompasses the phase space coordinates of 39% of the particles in the beam.

2.3 Closed-form solution to equations of motion

Instead of tracking a particle's trajectory piecewise through each magnet element in the accelerator, it is also possible to find a closed-form solution to the equations of motion. An accelerator can be described as a modified simple harmonic oscillator, in which the restoring force varies periodically as a function of the longitudinal coordinate s. The restoring force $K(s)$ is positive within a focusing quadrupole, negative within a defocusing quadrupole, and zero in the drift spaces between magnets. The equation of motion for this system is Hill's equation,

$$x'' + K(s)x = 0 \tag{2.9}$$

The solution of Hill's equation for a single particle is similar to the solution of a simple harmonic oscillator, but with periodically variable amplitude function $\beta(s)$ and phase advance $\psi(s)$:

$$x(s) = \sqrt{2J\beta(s)}\sin(\psi(s) + \phi_0) \tag{2.10a}$$

$$x'(s) = \sqrt{2J}(-\frac{\alpha(s)}{\sqrt{\beta(s)}}\sin(\psi(s) + \phi_0) + \frac{1}{\sqrt{\beta(s)}}\cos(\psi(s) + \phi_0), \tag{2.10b}$$

where J and ϕ_0 are the particle's initial conditions in action-angle coordinates. The beta function $\beta(s)$ is the same envelope function that was introduced in the previous section. The functions $\beta(s)$, the slope of the beta function $\alpha(s) \equiv -\frac{1}{2}\frac{d\beta}{ds}$, and the phase advance $\psi(s)$ are collectively referred to as the Twiss parameters. These equations can be written in a more compact form:

$$\begin{pmatrix} x(s) \\ x'(s) \end{pmatrix} = \sqrt{2J} \begin{pmatrix} \sqrt{\beta(s)} & 0 \\ -\frac{\alpha(s)}{\sqrt{\beta(s)}} & \frac{1}{\sqrt{\beta(s)}} \end{pmatrix} \cdot \begin{pmatrix} \cos\left(\psi(s) + \phi_0\right) \\ \sin\left(\psi(s) + \phi_0\right) \end{pmatrix} \tag{2.11}$$

and in this form it is clear that the particle's phase space coordinates each time it passes through s will lie on a circle of radius $\sqrt{2J}$ which has been deformed into an ellipse defined by the Twiss parameters at s. This deformation matrix is referred to as the beta matrix:

$$B(s) = \begin{pmatrix} \sqrt{\beta(s)} & 0 \\ -\frac{\alpha(s)}{\sqrt{\beta(s)}} & \frac{1}{\sqrt{\beta(s)}} \end{pmatrix} \tag{2.12}$$

Figure 2.8 shows an ellipse in x, x' phase space whose shape is defined by Eq. 2.11, along with the x, x' coordinates of an ensemble of 5000 particles with normally-distributed action J and uniformly-distributed initial angle ϕ_0. The area of this ellipse, which encloses 39% of particles in the beam, defines the RMS emittace: $A = \pi\epsilon_{RMS}$. Other definitions of emittance are also commonly used, such as the 95% emittance, which corresponds to the area of an ellipse containing 95% of particles in the beam. The one-sigma transverse beam size envelope is

$$x_{RMS}(s) = \sqrt{\epsilon_{RMS}\beta(s)} \tag{2.13}$$

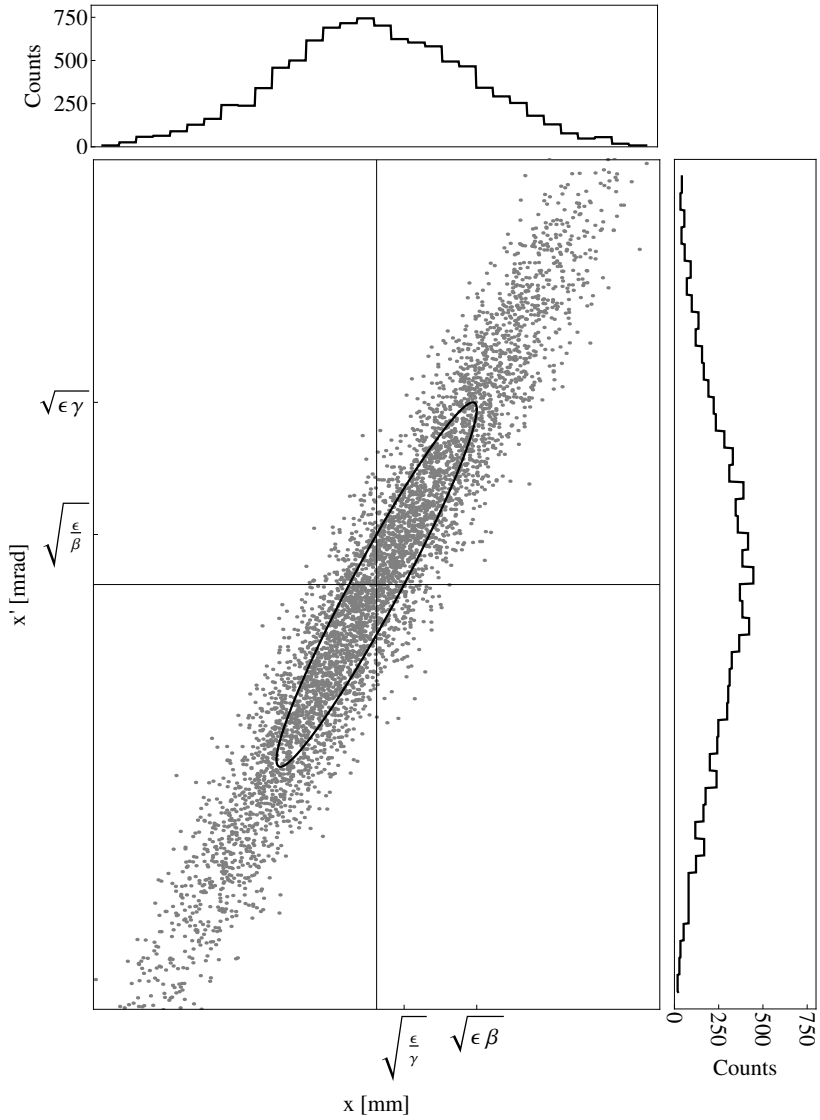

Figure 2.8: The gray points show the x, x' coordinates of 5000 particles in a beam, and the histograms show the particle density in x and x'. The black ellipse encompasses 39% of the particles in the beam and matches the Twiss parameters at this longitudinal position (see Eq. 2.11). The area of the ellipse is proportional to the RMS transverse emittance ($A = \pi\epsilon$), and the RMS beam size is $x_{rms} = \sqrt{\epsilon\beta}$

The map relating a particle's coordinates at two longitudinal positions s_0 and s can be described as a series of simple transformations, as illustrated in Fig. 2.9:

1. Transformation into action-angle coordinates using the inverse of the beta matrix (Eq. 2.12) for position s_0.

2. Rotation by the betatron phase difference between points s_0 and s_1.

3. Deformation from action-angle coordinates into a new ellipse using the beta matrix for position s_1.

Written in matrix form, this set of transformations that maps point s_0 to s_1 is

$$\begin{aligned} M_{s_0\to s_1} &= \begin{pmatrix} \sqrt{\beta_1} & 0 \\ -\frac{\alpha_1}{\sqrt{\beta_1}} & \frac{1}{\sqrt{\beta_1}} \end{pmatrix} \\ &\quad \cdot \begin{pmatrix} \cos\Delta\psi & \sin\Delta\psi \\ -\sin\Delta\psi & \cos\Delta\psi \end{pmatrix} \cdot \begin{pmatrix} \frac{1}{\sqrt{\beta_0}} & 0 \\ \frac{\alpha_0}{\sqrt{\beta_0}} & \sqrt{\beta_0} \end{pmatrix} \\ &= \begin{pmatrix} \sqrt{\frac{\beta_1}{\beta_0}}\left(\cos\Delta\psi + \alpha_0 \sin\Delta\psi\right) & \sqrt{\beta_0\beta_1}\sin\Delta\psi \\ -\frac{1+\alpha_1\alpha_0}{\sqrt{\beta_1\beta_0}}\sin\Delta\psi + \frac{\alpha_0-\alpha_1}{\sqrt{\beta_1\beta_0}}\cos\Delta\psi & \sqrt{\frac{\beta_0}{\beta_1}}(\cos\Delta\psi - \alpha_1\sin\Delta\psi) \end{pmatrix} \end{aligned} \tag{2.14}$$

where the subscript 0 or 1 indicates the value of the parameter at s_0 or s_1, and $\Delta\psi \equiv \psi_1 - \psi_0$ [17]. In the special case when $s_1 = s_0 + L$, where L is the circumference of the accelerator, the one-turn matrix reduces to

$$M_{s_0\to s_0+L} = \begin{pmatrix} \cos 2\pi\nu + \alpha_0 \sin 2\pi\nu & \beta_0 \sin 2\pi\nu \\ \gamma_0 \sin 2\pi\nu & \cos 2\pi\nu - \alpha_0 \sin 2\pi\nu \end{pmatrix} \tag{2.15}$$

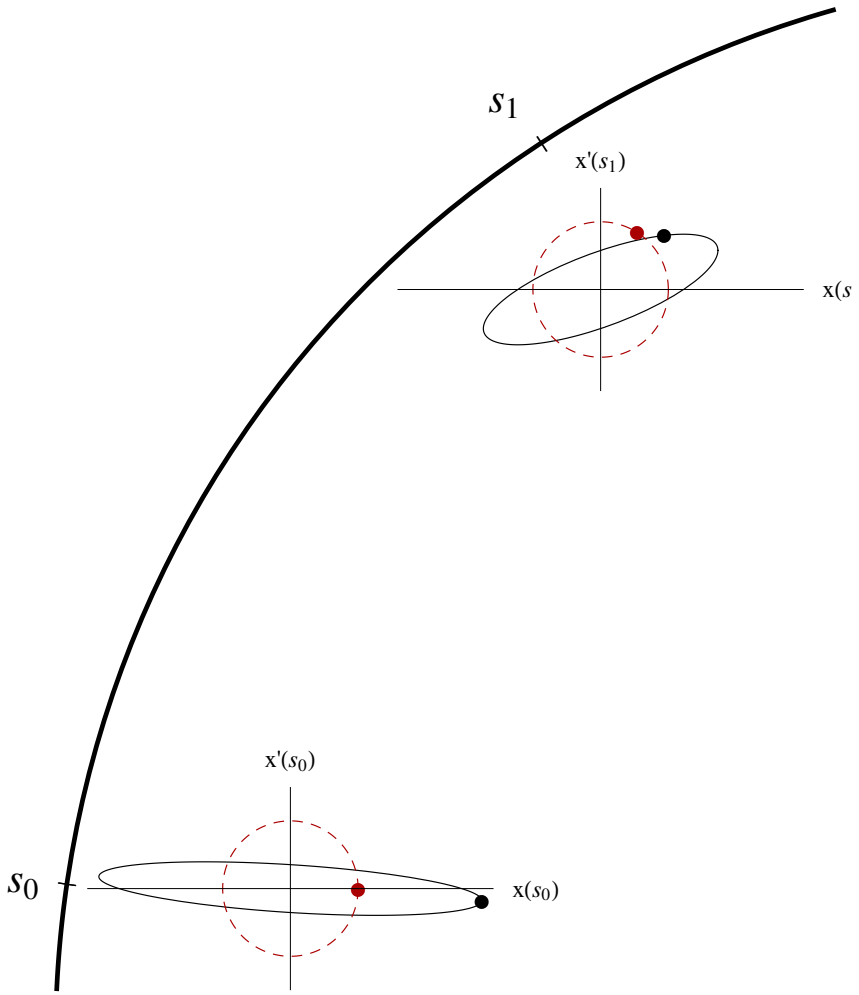

Figure 2.9: Phase space ellipses for a single particle at two longitudinal positions along the beam trajectory. The new coordinates at s_1 are found by first transforming the coordinates at s_0 (shown in black) into action/angle coordinates (shown in red) using the inverse beta matrix at s_0 (Eq. 2.12), then performing a rotation by an angle $\psi(s_1) - \psi(s_0)$ to propagate the action-angle coordinates to s_1 (shown in red), and then deforming into a new ellipse (shown in black) using the beta matrix at s_1. In this example the phase advance between s_0 and s_1, $\Delta\psi = \psi(s_1) - \psi(s_0)$, is 60 degrees.

where the Twiss parameter $\gamma \equiv \frac{1+\alpha(s)^2}{\beta(s)}$. The betatron tune ν is defined as the number of betatron oscillations made during one turn around the machine:

$$\nu = \frac{\psi(s+L) - \psi(s)}{2\pi} \tag{2.16}$$

The set of values for the horizontal and vertical betatron tune in accelerator is referred to as the working poing.

It is sometimes convenient to write this one-turn matrix in the form

$$M_{s \to s+L} = I \cos 2\pi\nu + J \sin 2\pi\nu = e^{J 2\pi\nu} \tag{2.17}$$

where I is the identity matrix and

$$J = \sqrt{-I} = \begin{pmatrix} \alpha(s) & \beta(s) \\ -\gamma(s) & -\alpha(s) \end{pmatrix} \tag{2.18}$$

We will use these three expressions for transfer matrices (Eqs. 2.14, 2.15, and 2.17) in the next section, when calculating the effects of magnet imperfections on beam dynamics.

The numerical values for the Twiss parameters in a machine can be determined by equating the element-by-element one-turn matrix (similar to Eq. 2.8) and the Twiss parameter one-turn matrix (Eq. 2.15). Once a numerical value for the one-turn matrix at s_0 is found by multiplying together the transfer matrices for each element in the lattice, the tune of the machine can be determined from the trace of the one-turn matrix:

$$Tr[M_{s_0 \to s_0+L}] = 2 \cos 2\pi\nu$$

Then, once the tune is known, the beta function at the given longitudinal position can be found from the upper right hand entry of the one-turn matrix:

$$\beta(s_0) = \frac{(M_{s_0 \to s_0+L})_{12}}{\sin 2\pi\nu} \tag{2.19}$$

These expressions (Eq. 2.19 and 2.19) will be used in the next section to compute the optics perturbations caused by magnet errors.

2.4 Effects of magnetic field imperfections on transverse dynamics

Any imperfections in the magnetic fields in an accelerator will affect the beam dynamics, potentially leading to emittance growth and beam loss. In this section we will discuss some of the sources of magnetic field imperfections in a real machine, and then calculate the effects that perturbations to dipolar and quadrupolar fields have on observable beam parameters.

2.4.1 Causes of magnetic field imperfections

While there will always be some small variations among magnets due to manufacturing processes, there are also some sources of field errors that are inherent in the design of magnets. Figure 2.3 shows the pole face contours needed to produce a pure multipole field, which must lie along a hyperbola that is an equipotential of the scalar potential. In order to leave space for the current-carrying coils, it may be necessary to truncate this hyperbolic contour in a way that causes distortions in the magnetic field far from the center of the magnet. Any beam particles passing outside of some "good field region" near

the center of the aperture will experience forces from unintentional higher-order magnetic multipole field components [18].

Small errors in the positioning of a magnet will also cause perturbations to the beam motion. If a magnet is offset transversely, a feed-down effect occurs which introduces lower-order multipole components. For example, consider a quadrupole magnet whose field is

$$\vec{B} = -\nabla \left(Im[C_2(x+iy)^2] \right) = -2C_2 \begin{pmatrix} y \\ x \end{pmatrix} \tag{2.20}$$

If the magnet is offset radially by some amount Δx, i.e. if we let $x \mapsto x + \Delta x$, then the field is

$$\vec{B} = -2C_2 \begin{pmatrix} y \\ x + \Delta x \end{pmatrix} = -2C_2 \begin{pmatrix} y \\ x \end{pmatrix} - 2C_2 \begin{pmatrix} 0 \\ \Delta x \end{pmatrix} \tag{2.21}$$

The dipole term proportional to the offset Δx appears in addition to the quadrupole term. This is illustrated in Fig. 2.4 C, which shows the trajectories of particles in a bunch passing through the outer edge of a quadrupole magnet. The particles in the beam are focused by the quadrupolar field, and the beam as a whole is also bent by an angle proportional to the transverse displacement. This feed-down effect occurs for all orders of multipoles; for example, a transverse offset in a sextupole magnet will produce a quadrupole term proportional to the offset Δx, and also a very small dipole term proportional to Δx^2.

2.4.2 Closed orbit distortion due to dipole errors

First we will examine the effect that a thin dipole field error has on the observable beam parameters. Suppose a thin dipole steering error $\Delta\theta$ is introduced to the lattice at longitudinal position s_0, as shown in Fig. 2.10. The new closed orbit of the beam will no longer lie along the reference orbit $(x = 0, x' = 0)$. The beam will get a transverse kick each time that it passes s_0, so the coordinates of the new closed orbit at $s = s_0$ will be the solution to the equation

$$\begin{pmatrix} x(s_0) \\ x'(s_0) \end{pmatrix} = M_{s_0 \to s_0+L} \cdot \begin{pmatrix} x(s_0) \\ x'(s_0) \end{pmatrix} + \begin{pmatrix} 0 \\ \Delta\theta \end{pmatrix} \tag{2.22}$$

where $M_{s_0 \to s_0+L}$ is the one-turn matrix at s_0. Inserting Eq. 2.17 and solving for (x, x') gives

$$\begin{aligned} \begin{pmatrix} x(s_0) \\ x'(s_0) \end{pmatrix} &= (I - M)^{-1} \begin{pmatrix} 0 \\ \Delta\theta \end{pmatrix} \\ &= (I - e^{J2\pi\nu})^{-1} \begin{pmatrix} 0 \\ \Delta\theta \end{pmatrix} \\ &= -(2J \sin \pi\nu)^{-1} (e^{J\pi\nu})^{-1} \begin{pmatrix} 0 \\ \Delta\theta \end{pmatrix} \end{aligned} \tag{2.23}$$

Inserting the expression for J given in Equation 2.18, we find the coordinates of the closed orbit at s_0 in terms of the Twiss parameters at s_0:

$$\begin{pmatrix} x(s_0) \\ x'(s_0) \end{pmatrix} = \frac{\Delta\theta(s_0)}{2 \sin \pi\nu} \begin{pmatrix} \beta_0 \cos \pi\nu \\ sin\pi\nu - \alpha_0 \cos \pi\nu \end{pmatrix} \tag{2.24}$$

where the subscript 0 indicates the value of the parameter at location s_0. The new closed orbit position at some arbitrary observation point s_1 is found

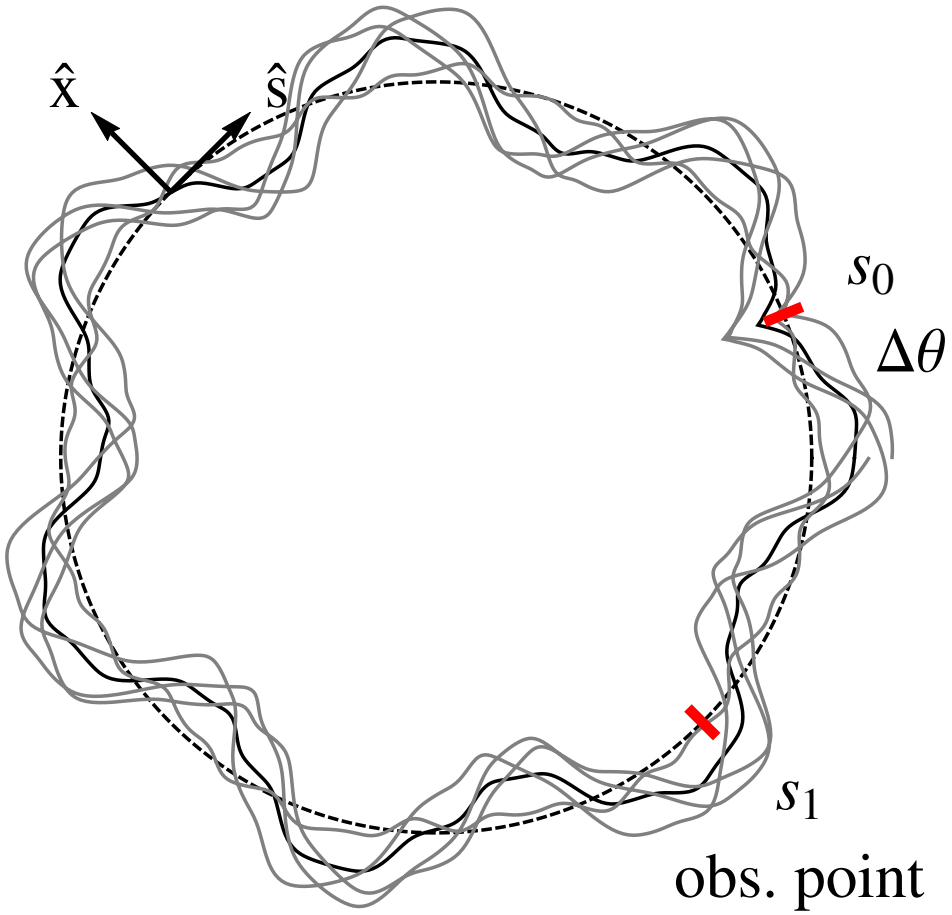

Figure 2.10: Horizontal orbit of a proton beam in the presence of a dipole error. The dashed black line is the closed orbit of the ideal, unperturbed machine, and the thick black line is the distorted closed orbit caused by the dipole error $\Delta\theta$ at position s_0. The gray line is the trajectory of an individual proton in the beam, which performs betatron oscillations around the new closed orbit. A calculation of the new closed orbit as observed from position s_1 is given in Eq. 2.26.

by propagating this trajectory using the transfer matrix $M_{s_0 \to s_1}$ as given in Equation 2.14:

$$\begin{aligned}\begin{pmatrix} x(s_1) \\ x'(s_1) \end{pmatrix} =& \frac{\Delta\theta(s_0)}{2\sin\pi\nu} \\ & \begin{pmatrix} \sqrt{\frac{\beta_1}{\beta_0}}(\cos\Delta\psi + \alpha_0 \sin\Delta\psi) & \sqrt{\beta_0\beta_1}\sin\Delta\psi \\ \gamma_1 \sin\Delta\psi & \sqrt{\frac{\beta_0}{\beta_1}}(\cos\Delta\psi - \alpha_1\sin\Delta\psi) \end{pmatrix} \\ & \cdot \begin{pmatrix} \beta_0 \; cos\pi\nu \\ \sin\pi\nu - \alpha_0 \cos\pi\nu \end{pmatrix} \end{aligned} \tag{2.25}$$

where $\Delta\phi$ is the betatron phase advance between s_0 and s_1. Solving for $x(s_1)$ gives the change to the closed orbit at longitudinal position s_1 due to a dipole error at longitudinal position s_0:

$$\Delta x(s_1) = \Delta\theta(s_0)\frac{\sqrt{\beta_1\beta_0}}{2\sin\pi\nu}\cos\left(|\Delta\psi| - \pi\nu\right) \tag{2.26}$$

The closed orbit distortion depends on the value of the beta function and the phase advance at both the location of the error s_0 and at the observation point s_1, and we will see in Chapter 3 that this fact can be exploited as a means of measuring the machine optics. The closed orbit distortion propagates around the ring with the same frequency as the betatron tune, and each particle will perform betatron oscillations around this new closed orbit, as shown in Fig. 2.10. As the tune approaches an integer value, the closed orbit distortion amplitude grows and even very small steering errors can cause large transverse oscillations and beam loss. For this reason, one must avoid setting the betatron tunes too close to the integer resonance.

2.4.3 Betatron tune shift due a quadrupole error

An imperfection in the focusing strength of magnets in the lattice will have two effects on the optical parameters of the machine: the betatron tune will change, and the value of the beta function all around the ring will be distorted. First we will calculate the change to the betatron tune due to a focusing error.

Suppose a thin quadrupole is inserted in the ring at longitudinal position s_0. The new one-turn transfer matrix M^* is obtained by multiplying together the unperturbed transfer matrix M_0 and the matrix for the thin quadrupole:

$$M^* = M_0 \cdot \begin{pmatrix} 1 & 0 \\ \Delta(k_1 l) & 1 \end{pmatrix} \tag{2.27}$$

Substituting the expression for the one-turn matrix from Eq. 2.15 yields

$$M^* = \begin{pmatrix} \cos(2\pi\nu_0) + \alpha_0 \sin(2\pi\nu_0) & \beta_0 \sin(2\pi\nu_0) \\ \gamma_0 \sin(2\pi\nu_0) & \cos(2\pi\nu_0) - \alpha_0 \sin(2\pi\nu_0) \end{pmatrix} \cdot \begin{pmatrix} 1 & 0 \\ \Delta(k_1 l) & 1 \end{pmatrix} \tag{2.28}$$

where the subscript "0" indicates the unperturbed Twiss parameters at s_0. The tune of the perturbed machine, $\nu^* \equiv \nu_0 + \Delta\nu$, can be found using Eq. 2.19:

$$Tr[M^*] = 2\cos 2\pi(\nu_0 + \Delta\nu) = 2\cos 2\pi\nu_0 + \Delta(k_1 l)\beta_0 \sin 2\pi\nu_0 \tag{2.29}$$

Expanding the cosine term on the left hand side and assuming $\Delta\nu$ is small (so $\sin 2\pi\Delta\nu \approx 2\pi\Delta\nu$ and $\cos 2\pi\Delta\nu \approx 1$), this yields

$$\cos 2\pi\nu_0 \cos 2\pi\Delta\nu - \sin 2\pi\nu_0 \sin 2\pi\Delta\nu = \cos 2\pi\nu_0 + \frac{1}{2}\Delta(k_1 l)\beta_0 \sin 2\pi\nu_0$$

$$\cos 2\pi\nu_0 - 2\pi\Delta\nu \sin 2\pi\nu_0 = \cos 2\pi\nu_0 + \frac{1}{2}\Delta(k_1 l)\beta_0 \sin 2\pi\nu_0$$

$$\Delta\nu = \frac{1}{4\pi}\Delta(k_1 l)\beta_0 \tag{2.30}$$

$$\Delta\nu = \frac{1}{4\pi}\Delta(k_1 l)\beta \tag{2.31}$$

The magnitude of the tune shift depends on both the size of the quadrupole error and on the value of the beta function at the location of the quadrupole error.

2.4.4 Beta beating due to a quadrupole error

In addition to changing the betatron tune, a focusing error also causes a distortion in the beta function, and therefore also in the size of the beam, all around the ring. Suppose a thin quadrupole error is introduced at longitudinal position s_0 and the beam is observed from position s_1, as shown in Fig. 2.11. The new one-turn matrix at s_1 is calculated from the unperturbed transfer matrices between points s_0 and s_1 and the transfer matrix for the thin quadrupole [19]:

$$M^*_{s_1 \to s_1+L} = M_{s_1 \to s_0+L} \cdot \begin{pmatrix} 1 & 0 \\ \Delta(k_1 l) & 1 \end{pmatrix} \cdot M_{s_0 \to s_1} \tag{2.32}$$

Inserting the expression for transfer matrices $M_{s_0 \to s_1}$ and $M_{s_1+L \to s_0}$ from Eq.2.14, and noting that if the phase advance from s_0 to s_1 is $\Delta\psi$ then the phase advance from s_1 to $s_0 + L$ is $2\pi\nu - \Delta\psi$, we then compare the upper right element of the matrices on both sides of Equation 2.32 to find the new

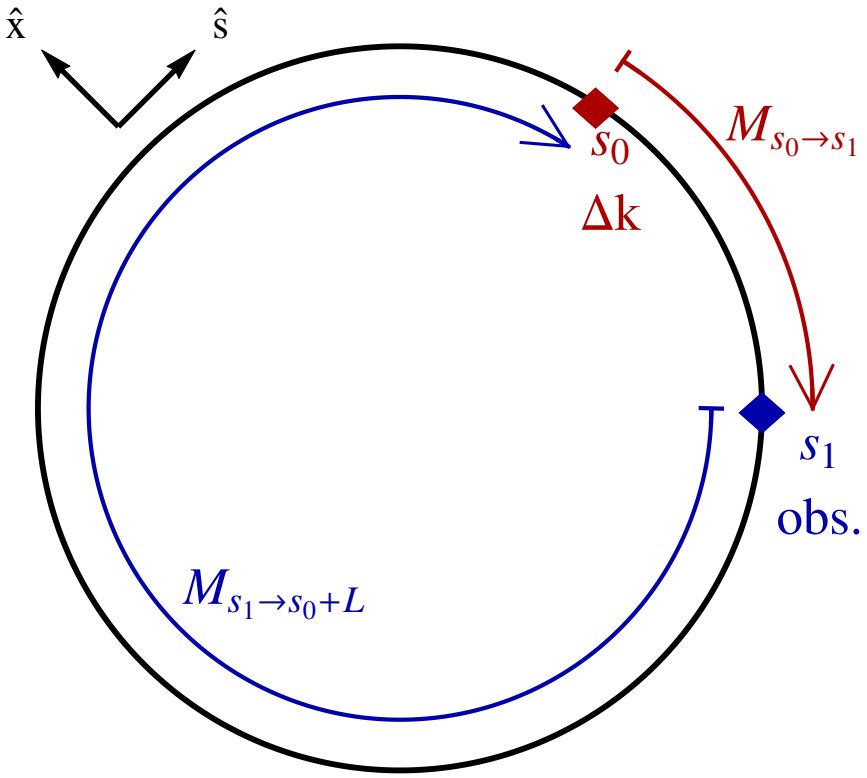

Figure 2.11: Diagram illustrating the method of calculating the effect of a quadrupole error on the beta function. A thin quadrupole element Δk is inserted in the ring at longitudinal position s_0, and the effect is observed from position s_1. The new one-turn matrix from point s_1, $M_{s_1 \to s_1 + L}$, is the product of the transfer matrix $M_{s_0 \to s_1}$, the matrix for the thin quadrupole, and the transfer matrix $M_{s_1 \to s_0 + L}$. The value of the perturbed beta function at s_1 can then be found from the upper right hand entry of the new one-turn transfer matrix (see Eq. 2.19).

beta function at s_1:

$$\begin{aligned}\beta_1^* \sin 2\pi\nu^* &= (\beta_1 + \Delta\beta_1) \sin 2\pi(\nu + \Delta\nu) \\ &= \beta_1 \sin 2\pi\nu + \Delta(k_1 l)\beta_0\beta_1 \sin(2\pi\nu - \Delta\psi) \sin\Delta\psi\end{aligned} \tag{2.33}$$

where the subscripts 0 and 1 indicate the values of the parameters at locations s_0 and s_1, and $\Delta\beta_1$ and $\Delta\nu$ indicate the change to the beta function and to the tune caused by the focusing error. Assuming again that $\Delta\nu$ is small (so $\sin 2\pi\Delta\nu \approx 2\pi\Delta\nu$ and $\cos 2\pi\Delta\nu \approx 1$) and neglecting terms of second order in small parameters $\Delta\beta$ or $\Delta\nu$, this reduces to an expression for the change in the beta function at s_1 due to a quadrupole perturbation at s_0:

$$\Delta\beta_1 = \Delta(k_1 l)\frac{\beta_0\beta_1}{2\sin 2\pi\nu}\cos(2|\psi_0 - \psi_1| - 2\pi\nu) \tag{2.34}$$

Figure 2.12 illustrates the distortion to the beam size, or equivalently, to the beta function when a focusing error is added to the machine lattice. The gray lines show the trajectory of a particle as it is tracked through fifty turns around the FNAL Booster lattice, with a focusing error added to a quadrupole at $s_0 = 57$ m. The black line is the expected beam size envelope, proportional to the square root of the unperturbed beta function. The distortion to the beta function, known as beta beating, propagates around the ring with twice the betatron frequency.

In the case where the tune is near a half integer, the sine term in the denominator approaches zero and even a very small focusing error can cause large beta beating with resulting beam loss. For this reason, tunes

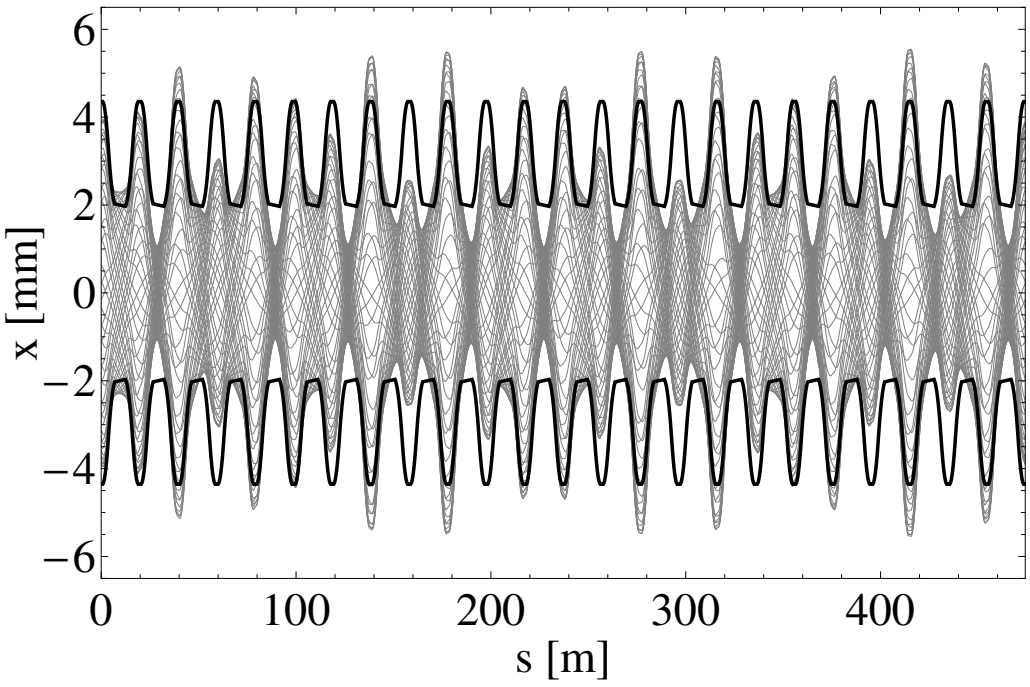

Figure 2.12: The gray lines show the trajectory of a particle (whose action corresponds to the 95% emittance of the beam) as it is tracked through fifty turns of the FNAL Booster lattice, with a focusing error added to a quadrupole at $s = 57$ m. The black line is the expected beam envelope in which 95% of beam particles are contained. The quadrupole error causes a distortion of the beta function and, equivalently, a distortion of the physical beam size all around the ring.

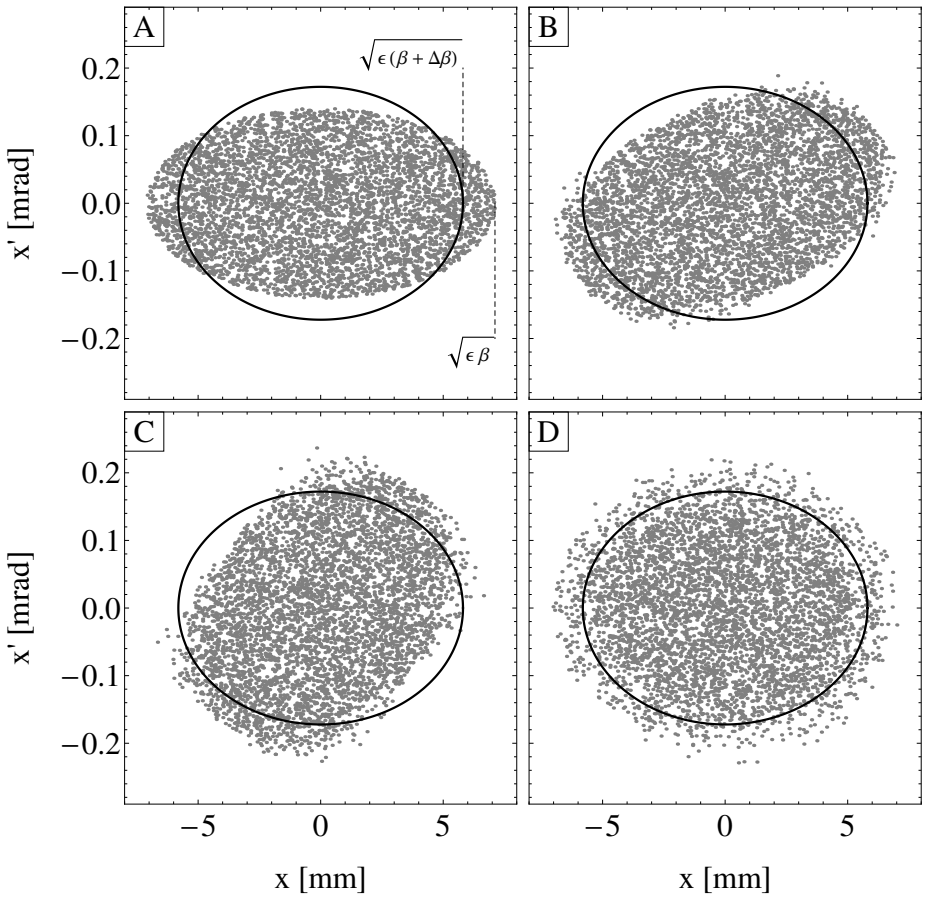

Figure 2.13: Simulated phase space distribution of a mismatched beam one turn (A), two turns (B), three turns (C), and two hundred turns (D) after injection. The gray points are the phase space coordinates of particles in a machine that has a focusing error and subsequent beta beating, as shown in Fig. 2.12. The black ellipse is defined by the distorted Twiss parameters in the machine (see Eq. 2.11). The initial distribution of particles is matched to the ideal, unperturbed Twiss parameters. Each particle travels on an ellipse defined by the distorted Twiss parameters, and over time the distribution will smear out to fill a larger ellipse whose shape matches the distorted Twiss parameters. This filamentation of phase space area is called emittance dilution.

near a half integer are typically avoided. This is similar to the result seen in Section 2.4.2, in which even a very small steering error can cause a large closed orbit distortion if the tune is near an integer. In general, resonant growth of beam oscillation can occur any time a multipolar magnet error of order n is present and the tune is near $\frac{1}{n}$ of an integer. Beta beating can be detrimental to the beam quality for several reasons. If it happens that the beta beating causes the beam size to be large in an area of the machine where the physical aperture is restricted, beam particles may impinge on the beam pipe or other machine hardware. This results in both a loss of beam intensity and also damaging and potentially dangerous irradiation of machine components.

Beta beating can also lead to emittance growth in a machine due to beam mismatch at injection. When beam is injected into the machine the shape of its phase space distribution must match the ellipse defined by the Twiss parameters, and if the Twiss parameters are distorted because of focusing errors then injection mismatch can occur. Figure 2.13 shows the phase space coordinates of particles tracked in a machine with a focusing error, as seen in Fig. 2.12. The initial distribution of particles is matched to the ideal Twiss parameters for the ideal machine, not the distorted Twiss parameters of the imperfect machine. Each particle will travel along an ellipse defined by the distorted Twiss parameters, and after many turns the particles will smear out to fill a larger ellipse with the shape determined by the distorted Twiss parameters.

2.4.5 Transverse coupling

Unintentional coupling between the transverse planes can arise due to accidental rotation of magnet elements around the longitudinal axis. If a normal quadrupole is rotated around the longitudinal axis, for example, the effect is the same as if a skew quadrupole is added to the lattice. The treatment of small accidental coupling perturbations in lattice can be done using variation of constants [20]. Coupling changes the observable tunes, and the relation between the observable eigentunes ν_+, ν_- and uncoupled tunes ν_x, ν_y is

$$\nu_\pm = \frac{1}{2}\left(\nu_x + \nu_y\right) \pm \frac{1}{2}\sqrt{\kappa^2 + \left(\nu_x + \nu_y\right)^2} \tag{2.35}$$

where κ is minimum tune separation, which characterizes strength of coupling. Figure 2.14 shows the measured tunes in the FNAL Booster as the focusing strength is changed. The black points show the average measured tunes over five beam pulses, and the error bars shown are the standard deviation of the five tune measurements. κ is the closest approach of the two measured tunes, which characterizes the magnitude of transverse coupling in the system. The dashed hyperbola show the theoretical expression for the observable coupled tunes, based on the uncoupled tunes and the measured minimum tune separation. The dashed lines are the asymptotes of the hyperbola, and they correspond to the tunes that would be observed if no transverse coupling was present in the magnet lattice.

Transverse coupling is generally undesirable because it complicates the beam dynamics and limits the ability to control the betatron tunes.

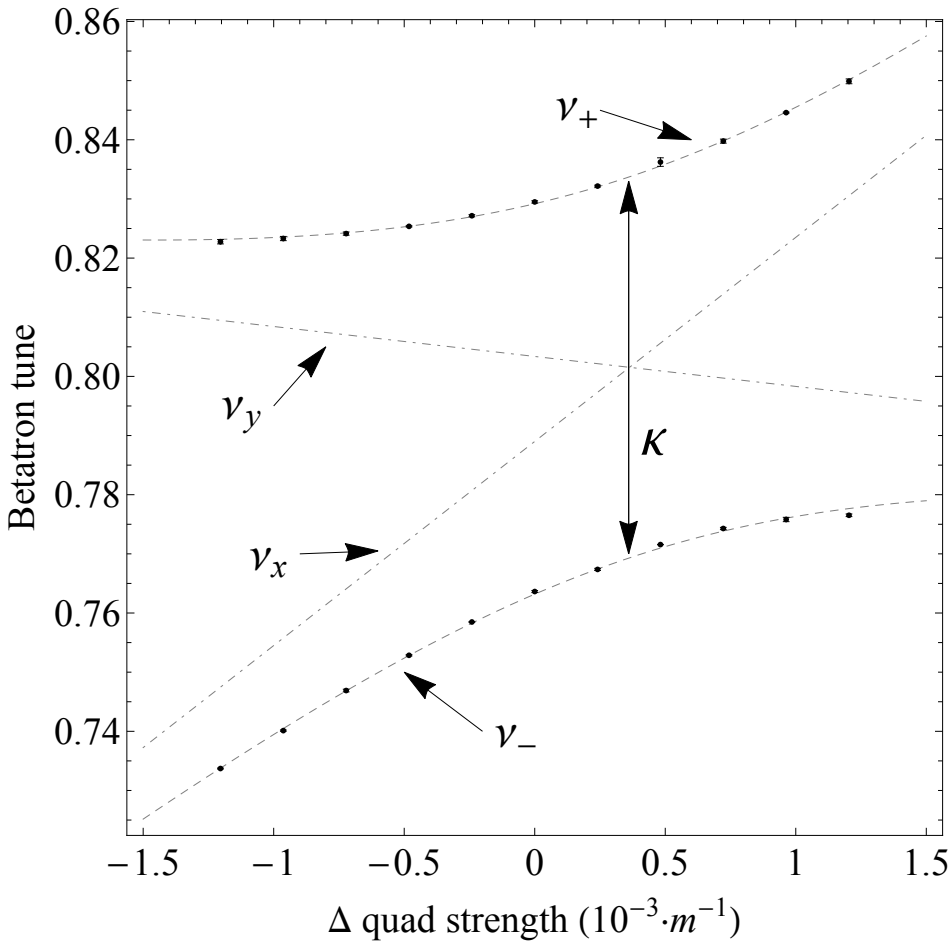

Figure 2.14: Tunes in the Fermilab Booster as a function of corrector quadrupole focusing strength. The black points show measured tunes as a function of quadrupole corrector magnet strength. Tunes were calculated using an interpolated FFT of 250-turn measured beam trajectory, and the error bars shown are the standard deviation of values from five measurements. κ is the closest approach of the two measured tunes, which characterizes the magnitude of transverse coupling in the system. The dashed hyperbola show the theoretical expression for the observable coupled tunes, based on the uncoupled tunes and the measured minimum tune separation (see Eq. 2.35). The dashed lines are the asymptotes of the hyperbola and correspond to the tunes that would be observed in the absence of transverse coupling.

2.5 Summary

This chapter has given an overview of linear transverse beam dynamics in an ideal synchrotron. We showed how a lattice of alternating focusing and defocusing magnets in an accelerator can be treated like a modified harmonic oscillator, whose solution has a non-constant but periodic amplitude function and phase advance function. The amplitude function, called the beta function, describes the shape of the maximum transverse particle excursion as a function of longitudinal position. The physical size of the beam is determined by both the beta function and by the emittance, which is a measure of the phase space area of the initial distribution of particles in the machine. The number of transverse oscillations that a particle makes per turn around the machine is called the betatron tune.

We also examined the effects of magnet imperfections on transverse beam dynamics. A dipole error will cause a distortion in the closed orbit, and the new closed orbit will oscillate around the design orbit with the same frequency as the betatron tune. The amplitude of this closed orbit distortion is inversely proportional to $\sin \pi\nu$, so the if the tune is near an integer even a very small steering error can cause a large closed orbit distortion. A quadrupole error will cause both a shift in the betatron tune and a distortion to the beta function. The beta function distortion, called beta beating, will oscillate around the ring at twice the frequency of the betatron tune. The amplitude of the beta beating is inversely proportional to $\sin 2\pi\nu$, so the if the tune is near a half integer even a very small focusing error can cause a large distortion to

the beta function, and therefore also to the physical beam size.

In the next chapter we will discuss in detail some methods for measuring the beta function, which is only indirectly observable, in a real machine lattice.

Chapter 3

Beam-based methods for optics measurements

In Chapter 2 we saw how small errors in dipolar or quadrupolar magnetic fields can distort the linear optics in a machine, potentially leading to beam loss and emittance growth. In this chapter we will discuss techniques for measuring distortions to the optical properties of the machine.

The beta function, which describes the physical size of the beam around the ring, is not directly observable, so we must develop ways to calculate the beta function based on observable quantities such as the transverse beam position and betatron tune. We will discuss two such methods for optics measurement: Linear Optics from Closed Orbits (LOCO), and K-modulation. The LOCO method [21] makes use of the fact that the closed orbit distortion caused by a dipole perturbation, measured at a given location, depends on the value of the beta function and the betatron phase advance at the location of both the error and the observation point. K-modulation [22] makes use of the fact that the change in tune caused by a quadrupole perturbation is proportional to the value of the beta function at the location of the quadrupole.

The remaining chapters will discuss the application of these optics measurement techniques in the FNAL Booster and the CERN PS Booster.

3.1 Linear Optics from Closed Orbits (LOCO)

The purpose of LOCO is to calibrate the element-by-element lattice model of an accelerator, making it more accurately reproduce some directly observable quantity in the real machine. The underlying assumption is that if the model accurately predicts a large set of directly observable quantities, its predictions for quantities which are not directly observable, such as the beta function, will also be accurate.

Closed orbit response to dipole perturbations is a good choice for the observable to use for model calibration because one can easily measure a large set of data points in the machine. We showed in 2.4.2 how to calculate the closed orbit response to a kick from a dipole at location s_j, observed at a BPM at location s_i, given the values of the beta and phase advance functions at s_i and s_j (see Eq. 2.26). LOCO inverts this process, allowing one to calculate Twiss parameters based on measured closed orbit responses to dipole kicks.

3.1.1 Measurement method

The measurements for LOCO are done by varying the current to each orbit corrector dipole magnet in the machine, one at a time, and measuring the new position of the closed orbit at all BPMs in the machine. Figure 3.1 shows the distortion to the closed orbit caused by changing the strength of a single orbit corrector dipole, for four different orbit corrector dipoles. The new orbit position at each BPM depends on the values of the beta function and phase advance at both the location of the dipole s_j and at the location of

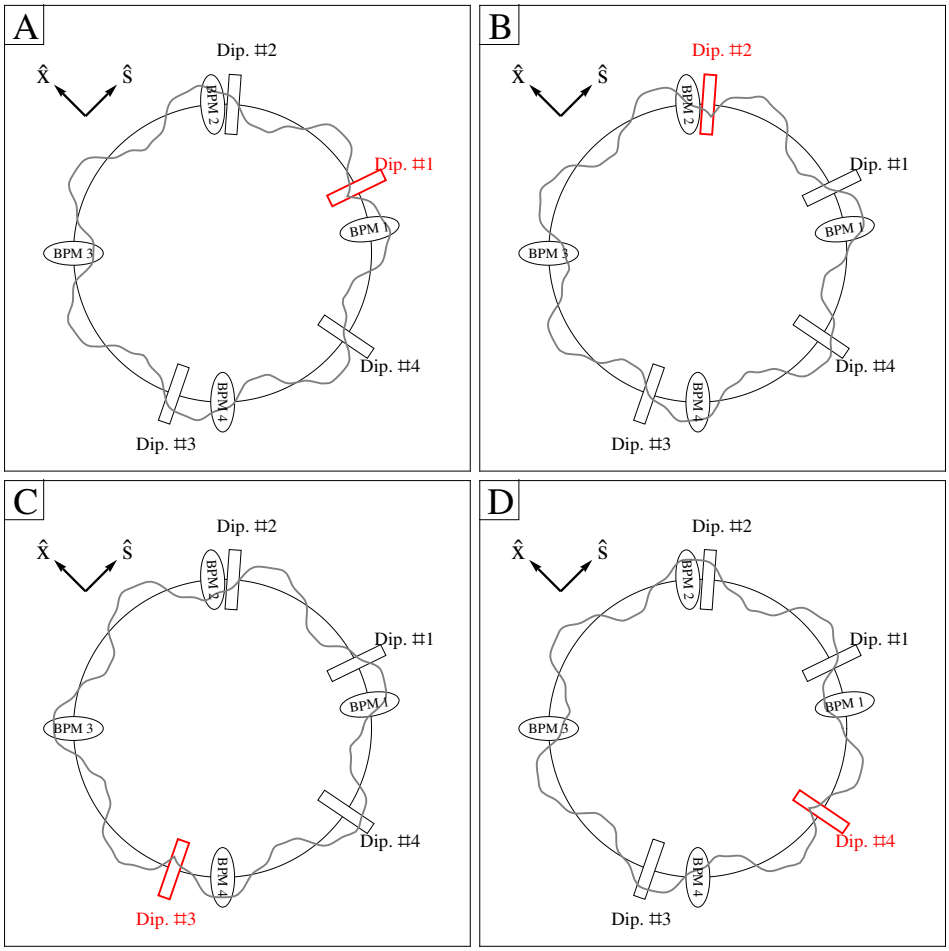

Figure 3.1: Closed orbit distortion resulting from perturbation to four different orbit corrector dipoles in the FNAL Booster. The ovals indicate beam position monitors, the rectangles indicate orbit corrector dipoles, the black circle is the unperturbed closed orbit, and the gray line is the distorted closed orbit due to a steering error in the dipole shown in red. The change in the closed orbit observed at each BPM depends on the beta function and phase advance at the location of the BPM and at the location of the dipole (see Eq. 3.1). A full set of orbit response measurements includes measuring the orbit response to all of the j orbit corrector dipoles available in the machine, as observed at each of the i beam position monitors, which yields a matrix of $i \times j$ measured data points.

the BPM s_i:

$$\left(\frac{\Delta x(s_i)}{\Delta\theta(s_j)}\right)_{model} = \frac{\sqrt{\beta(s_i)\beta(s_j)}}{2\sin(\pi\nu)}\cos(|\psi(s_i)-\psi(s_j)|-\pi\nu) \tag{3.1}$$

Measuring the orbit response to i dipoles at the location of j BPMs yields an Orbit Response Matrix (ORM) of $i \times j$ observable data points, each of which contains information about the Twiss parameters at two longitudinal positions in the ring.

Figure 3.2 is an example of an orbit response measurement in the FNAL Booster. (A) shows the measured x and y position of the closed orbit as a function of the angular kick from a dipole (labeled "Dip. #1" in Fig. 3.1A), as observed at one BPM (labeled "BPM 1" in Fig. 3.1A). The slope of the linear fit of the beam position at the ith BPM vs. the strength of the jth corrector makes up one entry in the $i \times j$ orbit response matrix. (B) shows the orbit response to one dipole (labeled "Dip. #1" in Fig. 3.1A) at all BPMs around the ring. The value of each point is the slope of position vs. dipole strength, and the error bars indicate one sigma confidence intervals of the fitted value of the slope. The 102 values in (B) make up one column of the $i \times j$ orbit response matrix.

3.1.2 Dependence of orbit response on lattice model parameters

LOCO uses a model of the accelerator that is built up of the matrices for each magnet element in the machine, as is discussed in Section 2.2. If the parameters of any lattice elements, such as the strengths of quadrupoles

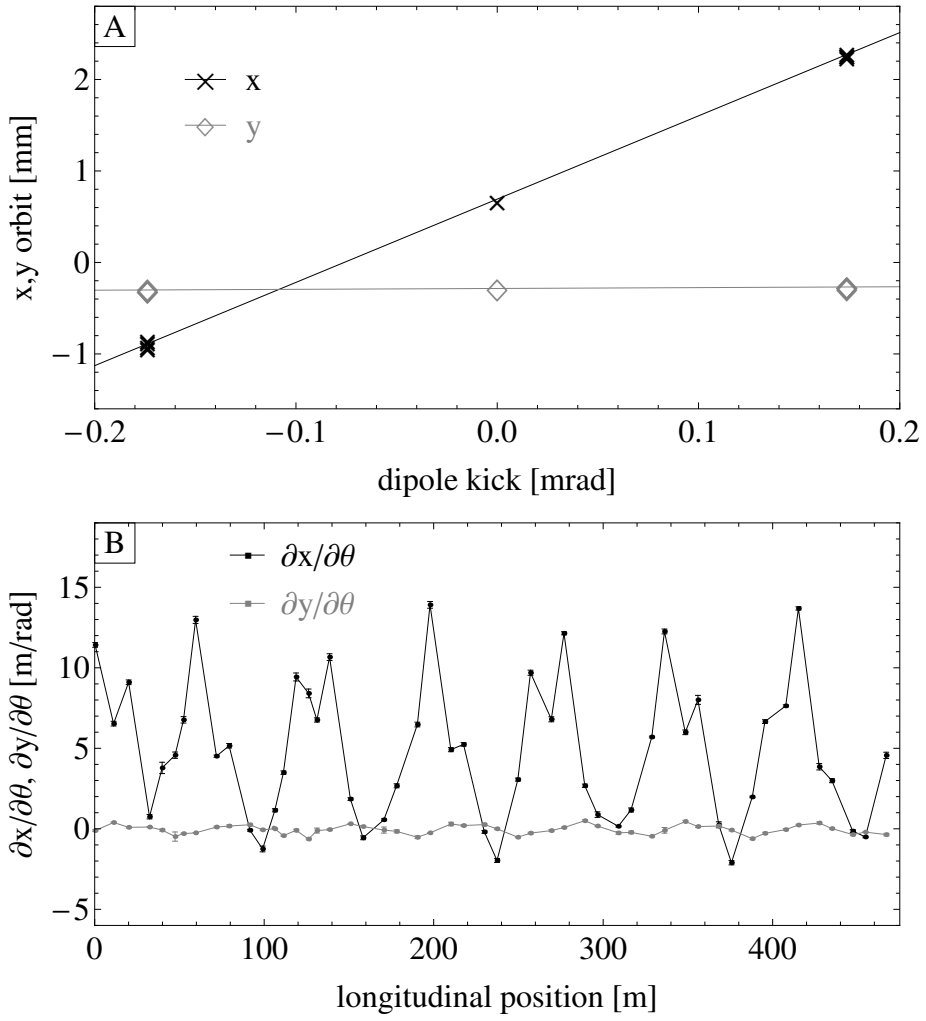

Figure 3.2: (A) shows the measured x and y beam orbit position at one BPM (labeled "BPM1" in Fig. 3.1) as a function of the strength of one horizontal dipole corrector magnet (labeled "Dip. #1" in Fig. 3.1), and linear fits of position vs. dipole strength. Each orbit measurement was repeated five times to reduce the effects of random fluctuations in the machine from pulse to pulse. Figure (B) shows the slopes of the position vs. dipole strength for that dipole at the 51 horizontal and 51 vertical BPMs in the FNAL Booster. The error bars on each point correspond to 1σ confidence intervals for the linear fits. The values shown in Fig. (B) make up one column of the (96 BPMs $\times$ 96 dipoles) Orbit Response Matrix.

and dipoles or the scaling factor of BPMs, are different in the real machine from what is assumed in the lattice model of the accelerator, then the measured orbit response will differ from the model prediction. There are six types of parameter errors that we will use for LOCO analysis: normal and skew quadrupole strength errors, dipole strength errors and tilts (i.e. rotations around the longitudinal axis), and BPM scaling errors and tilts. Below, we describe the effects that each of these types of errors has on the measured orbit response matrix.

Figure 3.3 shows how a 1% error in the strength of one normal quadrupole changes the ORM. The horizontal axes are the indices of the 32 BPMs and 26 dipoles in the CERN PSB, and the vertical axis is the absolute difference in the calculated orbit response with and without the focusing error. Focusing errors change the phase advance and beta function everywhere in the machine and therefore affect the orbit response to dipole perturbations everywhere in the machine. The diagonal portions of the orbit response matrix (horizontal orbit response to horizontal dipoles and the vertical orbit response to vertical dipoles) are most affected because there is little transverse coupling in the lattice, and therefore there is little off-plane orbit response.

The dependence of the orbit response on focusing strength or the tilt of elements is nonlinear. Figure 3.4 shows a simulation of the closed orbit response to a dipole error when there is also a focusing error $\Delta k_1 L$ in one of the quadrupoles. Ten closed orbits are shown in Fig. (A), each corresponding to a different focusing strength error. Figure (B) shows the position of the closed

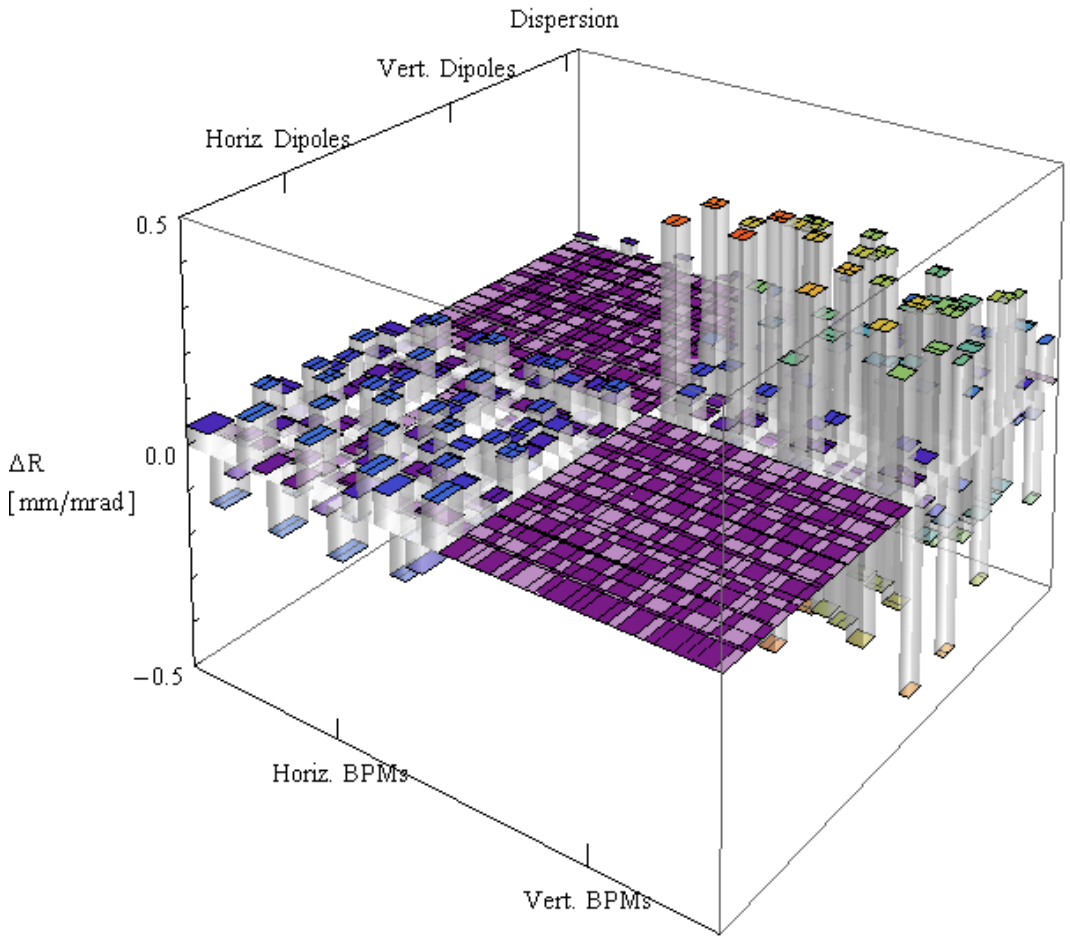

Figure 3.3: Simulation showing the change to the ORM caused by a 1% focusing strength error in one normal quadrupole, located near BPM #11. The horizontal axes are indices of horizontal and vertical BPMs and dipoles, and the vertical axis ΔR is the difference between calculated $\partial x/\partial\theta$ or $\partial y/\partial\theta$ with and without the focusing error. A focusing error primarily affects the diagonal portions of the orbit response matrix (horizontal orbit response to horizontal dipole perturbations, and vertical orbit response to vertical dipole perturbations).

orbit as measured by one BPM, as a function of the focusing error $\Delta k_1 L$. The orbit response is a nonlinear function of $\Delta k_1 L$ but is approximately linear for small focusing errors.

Figure 3.5 shows the change in the ORM caused by a 5 milliradian rotation of one normal quadrupole around the longitudinal axis, which is equivalent to adding a thin skew quadrupole element to the lattice model next to the normal quadrupole. This tilt error primarily affects the off-diagonal portions of the orbit response matrix (the horizontal orbit response to vertical dipole perturbations and the vertical orbit response to horizontal dipole perturbations) because it introduces coupling between the transverse planes.

Figure 3.6 shows how a 10% error in the strength of one dipole corrector magnet affects the ORM. A dipole calibration error does not affect the Twiss parameters in the machine, but it causes the measured orbit response to a dipole perturbation to be larger or smaller than expected. Only the same-plane part of one column of the response matrix is affected. A miscalibrated BPM produces a very similar effect in the ORM, except that the same-plane portion of one row of the response matrix is affected.

Figure 3.7 shows the change in the ORM caused by a 10 milliradian rotation of one BPM around the longitudinal axis. A tilted BPM has no real effect on the dynamics of the machine, but it introduces apparent transverse coupling in the position measured by the BPM and so affects the opposite-plane portion of two rows of the response matrix. A tilt in a dipole has a very similar effect, except that the opposite-plane portion of one column of

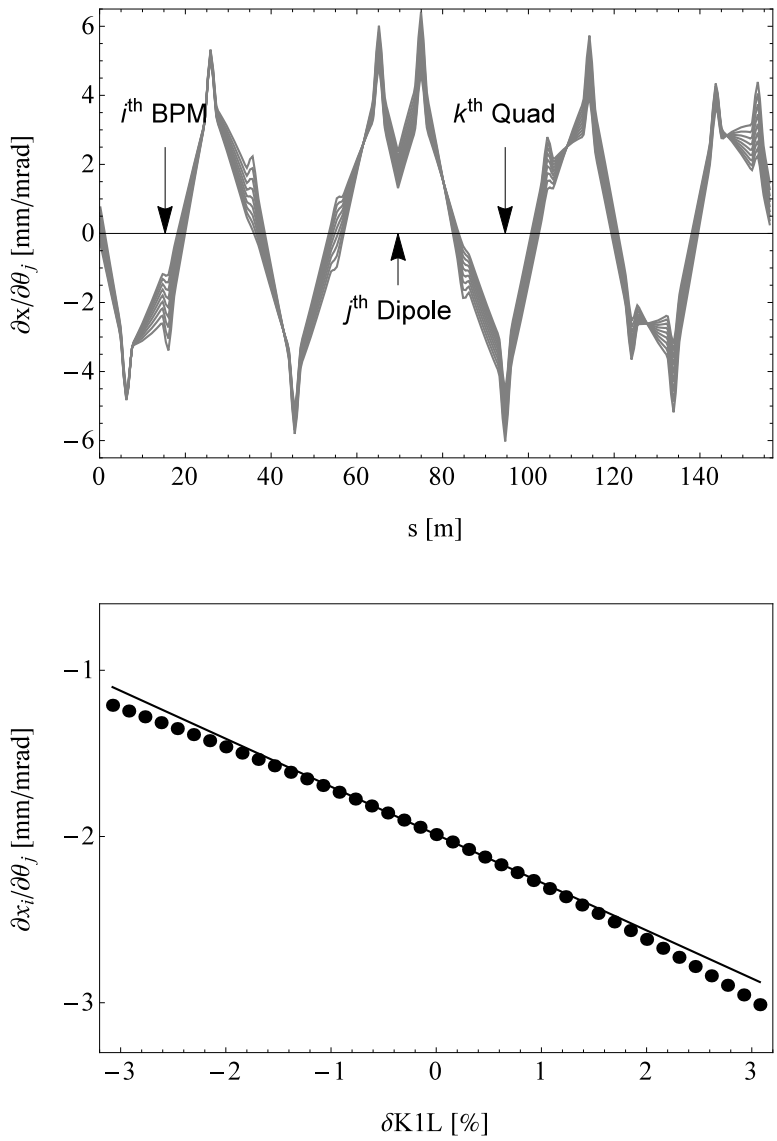

Figure 3.4: Figure A shows the calculated orbit response to a dipole perturbation in the CERN PSB when there is also a focusing error of varying magnitude in one quadrupole. Figure B shows the orbit position at a single BPM (located at the arrow in Fig. A) as a function of the quadrupole strength error and a linear fit. The orbit response is a nonlinear function of quadrupole strength, but a linear approximation is adequate for small focusing errors.

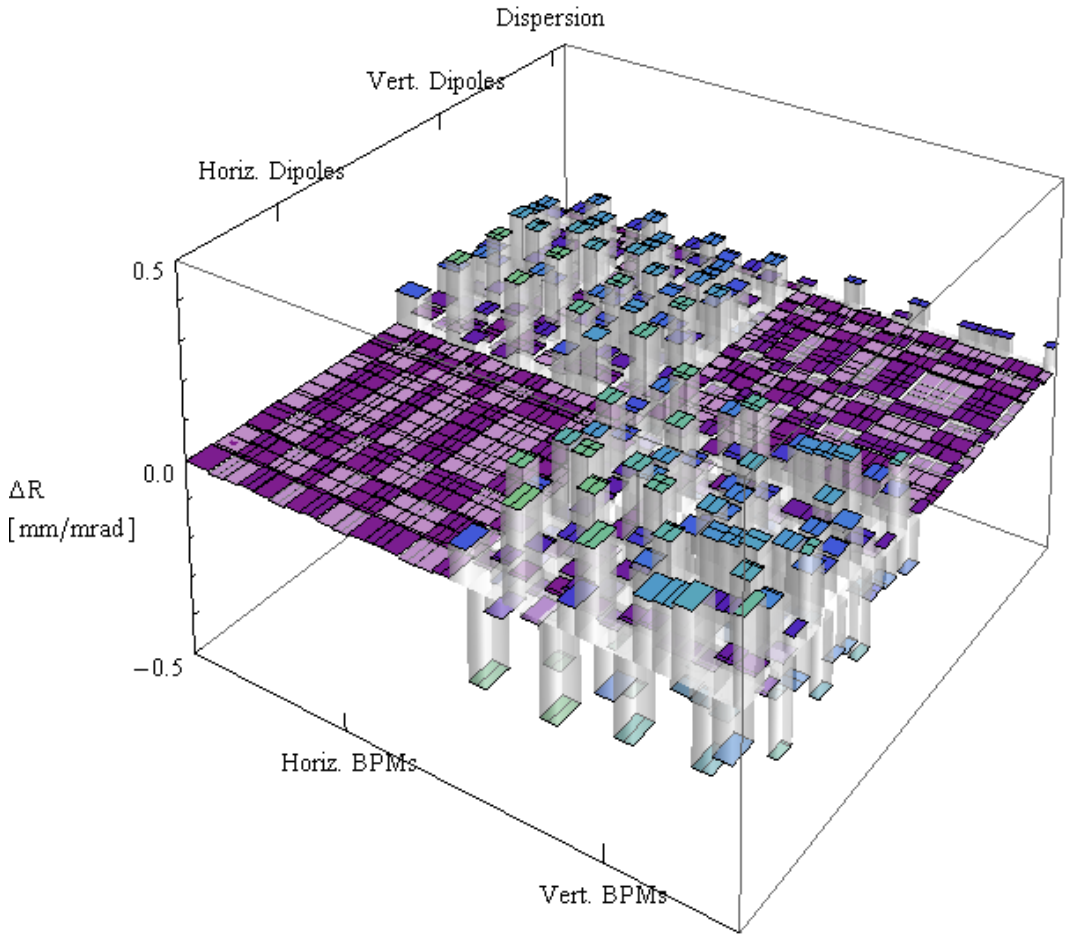

Figure 3.5: Simulation showing the change to the ORM when one quadrupole is rotated by 5 mrad around the s axis. The horizontal axes are indices of horizontal and vertical BPMs and dipoles, and the vertical axis ΔR is the difference between calculated $\partial x/\partial\theta$ or $\partial y/\partial\theta$ with and without the tilt error. The tilt error primarily affects the off-diagonal portions of the orbit response matrix (horizontal orbit response to vertical dipoles, and vertical orbit response to horizontal dipoles) because it introduces coupling between the transverse planes.

the response matrix is affected.

If there is a systematic error in either the calibration of all dipoles or the calibration of all BPMs, it is impossible to determine from orbit response measurements alone whether the fault lies with the dipoles or the BPMs, as is illustrated in fig. 3.8. If, for example, there is a scaling error in the BPM that causes it to read a position smaller than the real orbit position, then the slope of the orbit vs. kick linear fit will be too small. Likewise, if the dipole has a calibration error that causes it to produce a larger kick than we expect, the slope of the orbit vs. kick linear fit will also be too small. For horizontal plane, this ambiguity can be partially removed by including dispersion measurements (i.e. orbit response to beam momentum offset) as an extra column in the orbit response matrix.

3.1.3 Nonlinear least squares fitting

Nonlinear least squares fitting is used to find the set of model parameters (focusing errors, dipole and BPM calibrations and tilts) that minimizes the differences between the model predictions and the measured values for the orbit response matrix, weighted by the uncertainty of each measurement:

$$\chi^2 = \sum_{k=i,j} R_k^2 = \sum_{i,j} \left(\left(\frac{\partial z_i}{\partial \theta_j} \right)_{model} - \left(\frac{\partial z_i}{\partial \theta_j} \right)_{meas} \right)^2 \cdot \frac{1}{\sigma_{ij}^2} \tag{3.2}$$

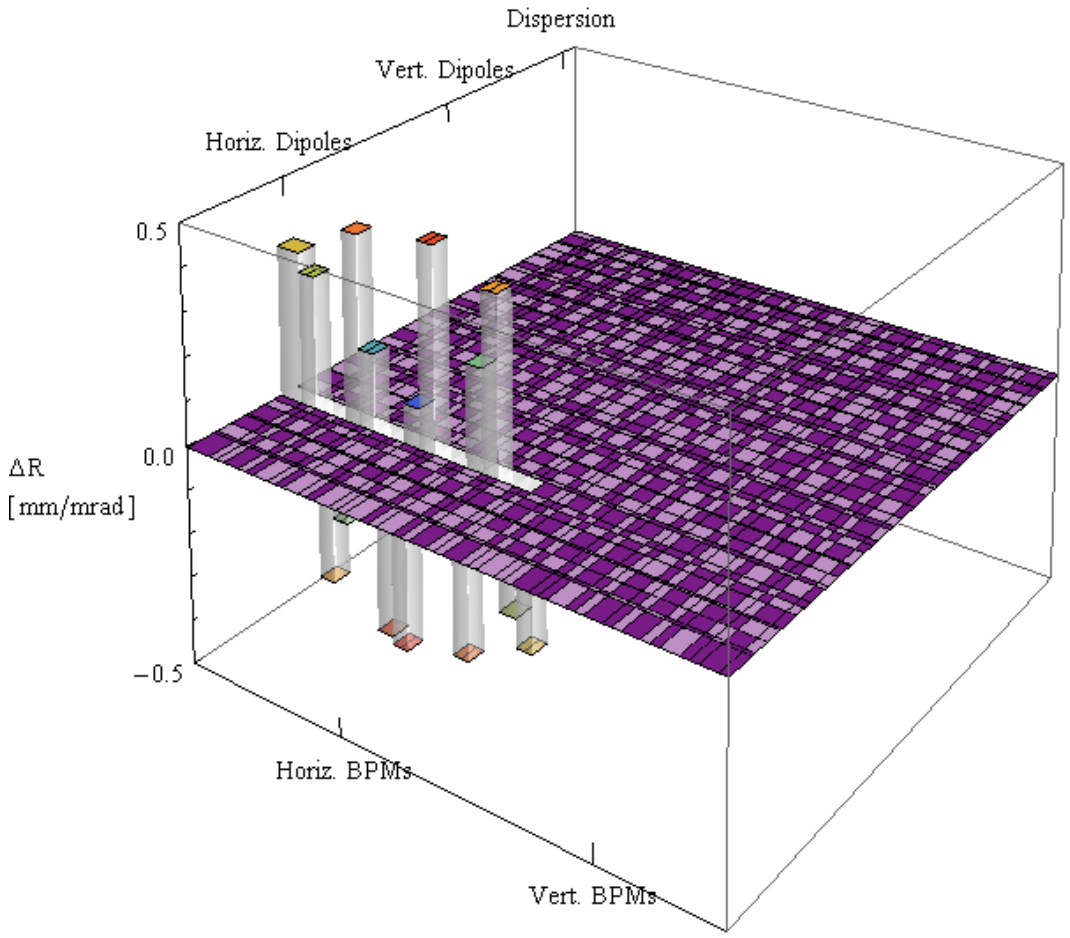

Figure 3.6: Simulation showing the change to the orbit response matrix caused by a 10% kick strength error in one of the orbit corrector dipoles. The horizontal axes are indices of horizontal and vertical BPMs and dipoles, and the vertical axis ΔR is the difference between calculated $\partial x/\partial\theta$ or $\partial y/\partial\theta$ with and without the tilt error. The dipole strength error primarily affects the same-plane response (horizontal orbit response to horizontal dipoles, and vertical orbit response to vertical dipoles) to the affected dipole.

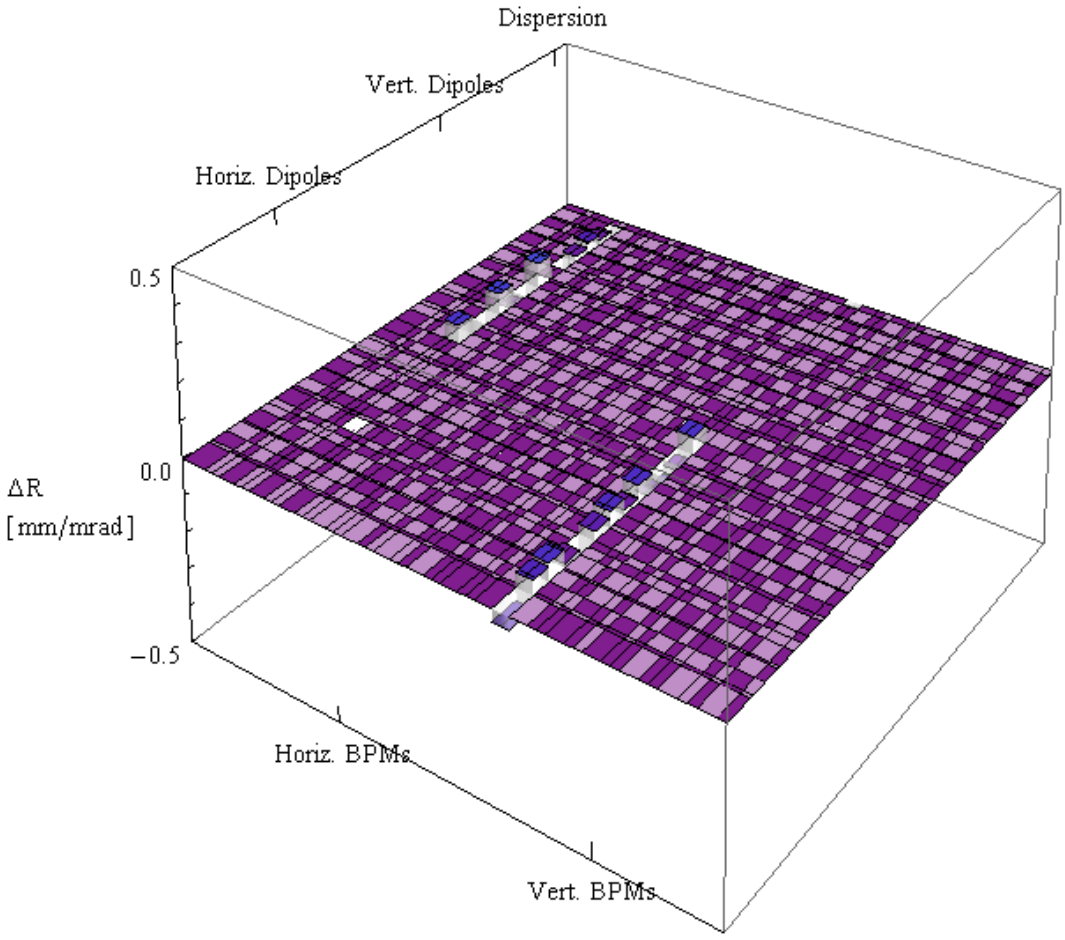

Figure 3.7: Simulation showing the change to the orbit response matrix when one BPM is rotated by 10 mrad around the s axis. The horizontal axes are indices of horizontal and vertical BPMs and dipoles, and the vertical axis ΔR is the difference between calculated $\partial x/\partial\theta$ or $\partial y/\partial\theta$ with and without the tilt error. The tilt error has no effect on the real beam dynamics in the machine, but it introduces an apparent opposite-plane response (horizontal orbit response to vertical dipoles, and vertical orbit response to horizontal dipoles) in the affected BPM.

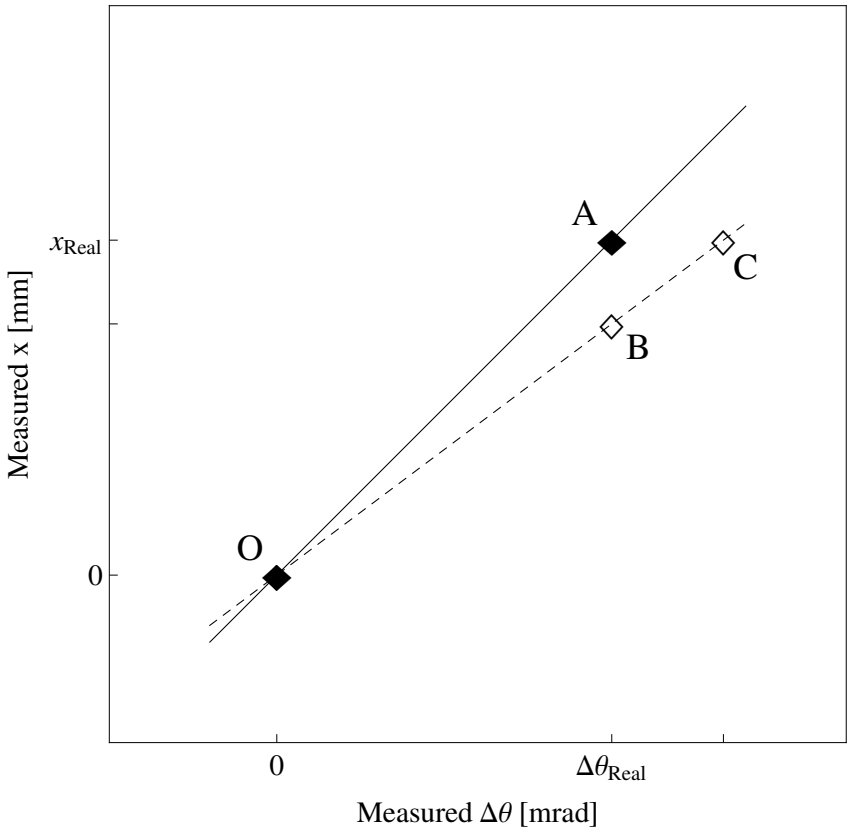

Figure 3.8: Illustration of the effect of dipole and BPM calibration errors on the linear fit of position vs. kick angle. If the calibration of the BPM and the dipole are accurate, then the measured orbit response will correspond to the slope of the line $\overline{OA}$. If the BPM has a scaling error and reads a position smaller than the real beam position, a smaller orbit response (corresponding to the slope of the line $\overline{OB}$) will be measured. Likewise, if the dipoles have a calibration error and the assumed strength is greater than the actual magnet strength, a smaller orbit response (corresponding to the slope of the line $\overline{OC}$) will be measured. If either all dipoles or all BPMs have a systematic calibration error, it is not possible to distinguish from orbit response measurements alone whether the error lies with the dipoles, the BPMs, or both.

$$\chi^2 = \sum_{i,j} R_{ij}^2 \tag{3.3}$$

$$= \sum_{i,j} \left(\left(\frac{\partial z_i}{\partial \theta_j} \right)_{model} - \left(\frac{\partial z_i}{\partial \theta_j} \right)_{meas} \right)^2 \cdot \frac{1}{\sigma_{ij}^2} \tag{3.4}$$

Here, z stands for both the horizontal and vertical orbit positions. In the case of the FNAL Booster, for example, the error vector $\vec{R}$ has $k = 9792$ elements, which come from measuring the orbit response to 96 dipoles (48 horizontal and 48 vertical) at 102 BPMs (51 horizontal and 51 vertical). This error vector is a function of the value of the set of variable model parameters $\vec{p}$. In the case of the FNAL Booster, the parameter vector $\vec{p}$ has $m = 492$ elements (48 normal quadrupole errors, 48 skew quadrupole errors, 96 dipole gains, 96 dipole tilts, 102 BPM gains, and 102 BPM tilts). The elements of the Jacobian response matrix $J_{km} = \frac{\partial R_k}{\partial p_m}$ are calculated numerically using the lattice model of the machine. We want to find a new set of model parameters that minimizes the error vector $\vec{R}(\vec{p})$:

$$\vec{R}(\vec{p_0} + \vec{\Delta p}) \approx \vec{R}(\vec{p_0}) + \overline{J} \cdot \vec{\Delta p} = 0$$

$$\overline{J} \cdot \vec{\Delta p} = -\vec{R}(\vec{p_0}) \tag{3.5}$$

The Jacobian matrix $\overline{J}$ is then inverted using singular value decomposition to solve for the set of parameters $\vec{\Delta p}$. It is generally necessary to iterate the fitting procedure since the dependence of the orbit response on quadrupole errors is nonlinear and therefore the Jacobian depends on the initial values of the quadrupole error parameters.

Fitting can generally be improved by making a careful choice of singular value threshold when inverting the Jacobian. Small singular values correspond to parameters that are poorly constrained by the measured data. Setting small singular values to zero helps to prevent arriving at a solution with excessively large parameter values that do little to improve the fit.

Ultimately the success of the LOCO method depends on the number of BPMs and dipoles available for the ORM measurements, the resolution of the BPMs, and the stability of the machine during the period when measurements are made. The fitting is most reliable when the system is highly over-determined, i.e. when there are many more measured data points than there are variable model parameters.

3.1.4 Error analysis

The standard errors for parameter values can be calculated from the Jacobian matrix J and the measurement errors $\vec{\sigma_R}$:

$$\vec{\sigma_p^2} = \overline{J}^T \cdot \overline{\Sigma_R} \cdot \overline{J} \tag{3.6}$$

where $\overline{\Sigma_R}$ is a diagonal matrix whose entries are the variances of the measured orbit responses $\vec{\sigma_R^2}$ [23].

This estimate of the parameter uncertainties assumes that the measurement errors are normally distributed, but this is not necessarily a valid assumption. Unknown factors such as nonlinearities in the BPM response at large transverse positions can result in a non-normal distribution of measure-

ment errors, so these parameter error estimates should be viewed as a lower bound. In addition, the choice of singular value threshold can have a large effect on the fitted parameter values.

It is not as simple to find an analytical expression for the standard error of the beta function distortions that correspond to a given set of model parameter standard errors, so a numerical simulation approach was used instead. Ten simulated data sets were analyzed, in which normally distributed errors (corresponding to the standard error of each measurement) were added to the measured responses and then LOCO analysis was repeated on each of the simulated data sets. Figure 3.9 shows the model parameter standard errors calculated for the CERN PS Booster using both of these methods. The gray lines show the standard error calculated from the Jacobian, using Equation 3.6. The black lines show the standard error of the mean for the parameter values found from the ten sets of simulated data. The standard errors for the model parameters found using these two methods are consistent.

Figure 3.10 shows the uncertainty in the horizontal beta function (A), the vertical beta function (B), and the horizontal dispersion function (C), calculated using numerical simulation. The histograms show $(\beta_0(s)-\beta_n(s))/\beta_0(s)$, which is the difference between the model optics functions obtained using the measured data and the functions obtained using $n = 10$ trials in which random errors had been added to the measured orbit response matrix. The relative errors for the calculations of optics functions from LOCO was found to be about 4%. These estimates of uncertainty must be treated as a lower limit,

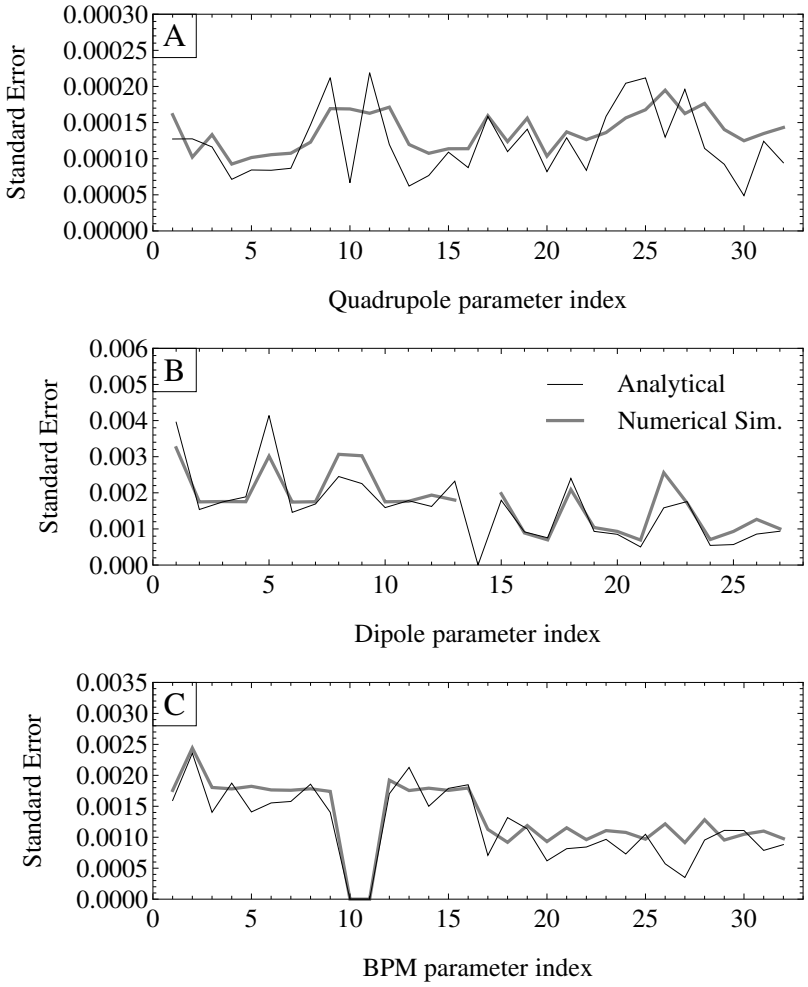

Figure 3.9: The gray lines show the standard errors for the parameter values from LOCO fitting in the CERN PSB, calculated analytically from the Jacobian (see Eq. 3.6). The black lines show the standard error of the mean for the parameters calculated from ten simulated data sets, in which random errors had been added to the measured orbit response matrix. See discussion in Section 3.1.4.

since the numerical simulation method assumes that measurement errors are normally distributed but that may not be true in the real machine.

3.1.5 Summary of LOCO method

The essence of the LOCO method is to adjust focusing parameters in the element-by-element lattice model of an accelerator in order to minimize the difference between the measured orbit response to dipole perturbations and the model predictions. This method is generally very effective for identifying focusing errors in the machine lattice because one can easily measure a large number of data points in the machine, and therefore the least-squares optimization problem is highly over-constrained. Once the lattice model includes a realistic estimate of focusing errors, it gives more accurate predictions for the optical functions everywhere in the ring.

There are two practical benefits from calibrating the lattice model using LOCO. First, if the main focusing magnets in an accelerator can be independently adjusted or if there is a sufficient number of corrector quadrupoles, it is straightforward to correct optics errors such as transverse coupling or beta beating using LOCO. In the case of transverse coupling, if the skew focusing error parameters used for LOCO are located within the skew quad corrector magnets in the real machine, the machine can be decoupled by setting the skew quad correctors with strengths equal and opposite to the errors found from LOCO. Likewise, if the normal focusing error parameters for LOCO are placed within the normal quadrupole corrector magnets, then the beta beating

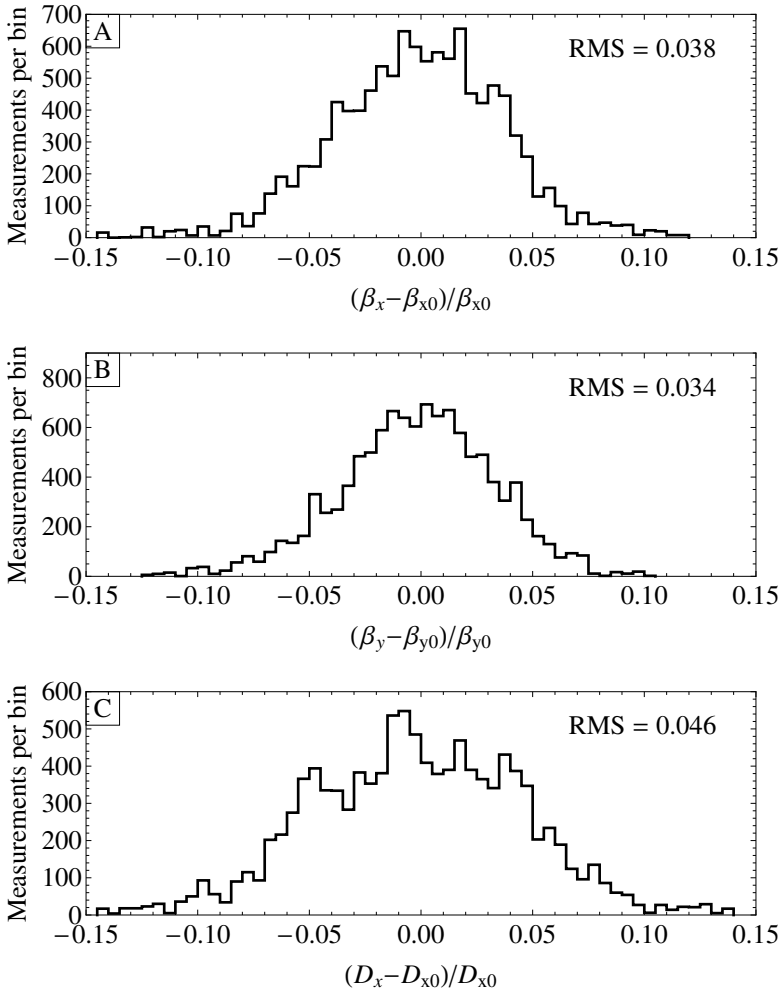

Figure 3.10: Deviation among ten trials of optics calculations in the PSB using LOCO, where each trial uses a simulated data set with random error added to the measured beam positions. Histograms show relative difference between twiss parameters from the measured data set and from the simulated data sets, at many longitudinal positions around the ring. (A) shows horizontal relative difference in horizontal beta function $(\beta_{x0} - \beta_{xn})/\beta_{x0}$, (B) shows relative difference in vertical beta function $(\beta_{y0} - \beta_{yn})/\beta_{y0}$, and (C) shows relative difference in horizontal dispersion function $(D_{x0} - D_{xn})/D_{x0}$. The RMS values are used as an estimate of the uncertainty of the beta and dispersion function calculations using LOCO (see Fig. 4.9)

can be corrected by setting the normal quad correctors with strengths equal and opposite to the normal focusing errors found from LOCO. These LOCO-based optics corrections were carried out in the FNAL Booster, as will be discussed in Chapter 4.

In machines where the main quadrupoles cannot be individually adjusted and there are not enough quadrupole corrector magnets to allow for beta beating correction, the results of LOCO calibration are still useful. The results of all beam dynamics simulations will be more accurate once there is a realistic distribution of focusing errors in the machine model. The errors found from LOCO allow for better modeling and understanding of more complicated beam dynamics effects, such as beam loss near resonances with intense, space-charge-dominated beams. This is the case with the CERN PSB, as will be discussed in Chapter 5.

3.2 K-modulation

The introduction of an error in the focusing strength of a quadrupole $k_1 l$ changes the betatron tune, as was discussed in Section 2.4. The size of this tune shift is proportional to the size of the quadrupole error and to the value of the beta function at the location of the quadrupole error (see Eq. 2.31). Measuring how the betatron tune changes in response to a change in the strength of a quadrupole magnet is therefore a straightforward way to measure the beta function at the location of the quadrupole magnet.

A strength of this method of measuring the beta function is that it is

model-independent; the accuracy of the results depend only on the accuracy of the tune measurement and the accuracy with which the quadrupole perturbation is known. A weakness of this method is that it only gives information about the values of the beta function at the location of corrector quadrupoles. It says nothing about how the beta function may be distorted in other regions of the ring or what focusing errors cause the distortions. Equation 2.31 holds only when there is no coupling between the transverse planes, so any coupling in the machine must be corrected before this method can be applied.

3.2.1 Measurement method

The measurements for K-modulation are done by changing the current to one quadrupole corrector magnet in the machine, exciting coherent transverse oscillations in the beam with a fast kicker magnet, and measuring the turn-by-turn trajectory with a BPM. The betatron tune before and after the quadrupole perturbation is calculated from a Fourier transform of the measured trajectory. This process is then repeated for each quadrupole corrector in the machine (48 in the case of the FNAL Booster).

Figure 3.11 shows the measured tune as a function of the strength of one quadrupole corrector magnet in the FNAL Booster. The crosses show the horizontal betatron tunes calculated from Fourier transforms of the horizontal turn-by-turn beam trajectories, which were measured during five beam pulses for each quadrupole setting. The solid black line is a linear fit of ν_x vs. $\Delta k_1 l$. The diamonds show the vertical betatron tunes calculated from vertical beam

trajectories, and the dashed black line is a linear fit of ν_y vs. $\Delta k_1 l$. The slope of each linear fit is proportional to the beta function at the location of the quadrupole magnet (see Eq. 2.31).

The tune resolution for a discrete Fourier transform is 1/N, where N is the number of turns sampled in the measured beam trajectory. In cases where the number of turns that can be used is limited, interpolation can be used to improve the tune resolution. For these measurements we used the FFT interpolation algorithm SUSSIX, which gives a tune resolution of $\sim 1/N^2$ to $1/N^{1.5}$ depending on the noise level in the BPM trajectory signal [24].

3.2.2 Error analysis

Uncertainty in the beta function calculated using K-modulation comes from two sources: the uncertainty in the measurement of the tune, and uncertainty in the strength of the quadrupole strength bump. The beta function calculated from the tune shift $\Delta\nu$ and the quadrupole perturbation $\Delta k_1 l$ is

$$\beta = 4\pi \frac{\Delta\nu}{\Delta k_1 l} \tag{3.7}$$

so the uncertainty in the beta function is

$$\sigma_\beta^2 = \left(\frac{4\pi}{\Delta k_1 l}\right)^2 \sigma_\nu^2 + \left(\frac{4\pi\Delta\nu}{(\Delta k_1 l)^2}\right)^2 \sigma_k^2 \tag{3.8}$$

where σ_ν^2 is the variance in the tune measurement, σ_k^2 is the variance in the focusing strength perturbation, and σ_β^2 is the variance in the calculated beta function.

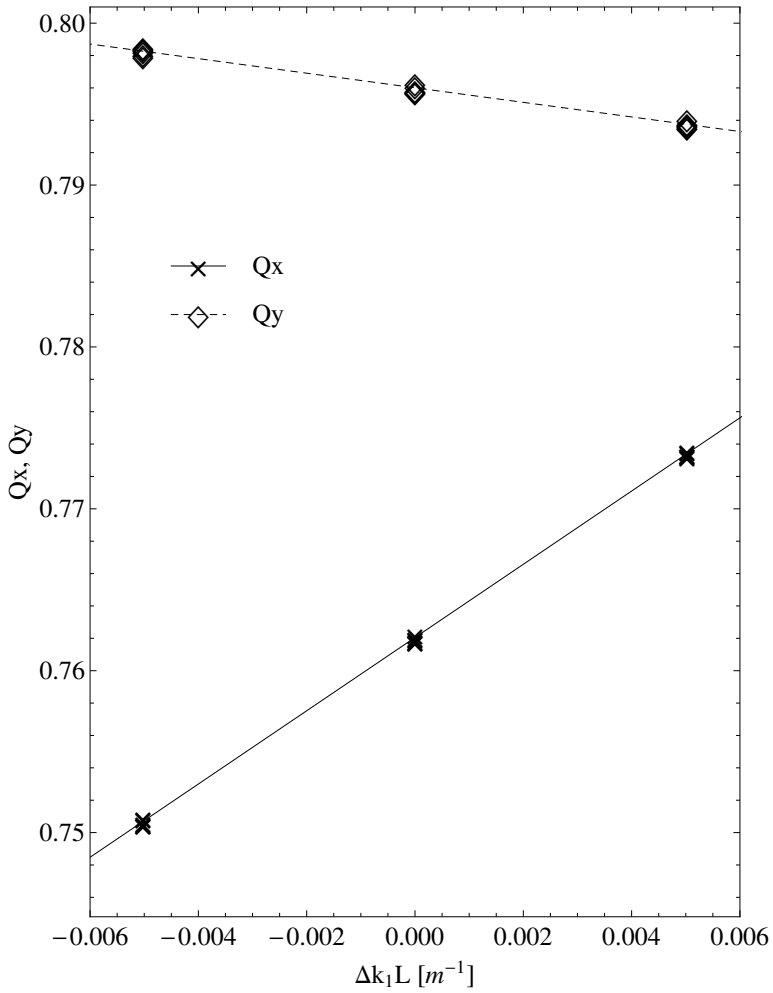

Figure 3.11: Example of measured tune as a function of the perturbation in one quadrupole corrector magnet. The crosses show the horizontal betatron tune, measured five times at each quadrupole setting, and the solid black line is a linear fit of ν_x vs. $\Delta k_1 L$. The diamonds show the vertical betatron tune, measured five times at each quadrupole setting, and the dashed black line is a linear fit of ν_x vs. $\Delta k_1 L$. The slope of each linear fit is proportional to the beta function at the location of the quadrupole magnet (see Eq. 2.31).

Figure 3.12 shows the measured tunes during 400 turns in the FNAL Booster, for five beam pulses. The tunes were calculated using the interpolated FFT algorithm SUSSIX, using sliding bins of 100 turns each; i.e. the tune shown for turn number 2000 is from an FFT of turns 2000-2099, the tune shown for turn number 2001 is from an FFT of turns 2001-2100, etc. SUSSIX calculates tunes with a resolution of $\sim 1/N^2$ (depending on the noise level in the trajectory measurement), so the expected tune resolution for these 100-turn calculations is $\sim$ 0.001 to 0.0001. However, the tune in the booster changes on short time scales, so the limiting factor in tune determination is the stability of the tune rather than the precision of the FFT. In order to minimize the effect of tune instability, only 100 turns were used for tune calculations. The estimated uncertainty of the tune measurements is 0.001.

The precision of the beta function measurement also depends on how precisely the quadrupole perturbation is known. The strength of the quadrupole magnet is calculated based on the magnet current setting and on the scaling factor for magnetic field produced per amp. The scaling factor was measured for all magnets before they were installed, and the standard deviation among magnets was found to be 0.43%.

Figure 3.13 (A) shows the absolute value of the difference between the magnet current setting and the value read out from the power supply. The current error in the power supply is larger the more quickly the current is ramped. Figure 3.13 (A) is a histogram of $|I_{set} - I_{read}|$ measurements for all magnets during the time period from 4 to 12 ms. The RMS difference between

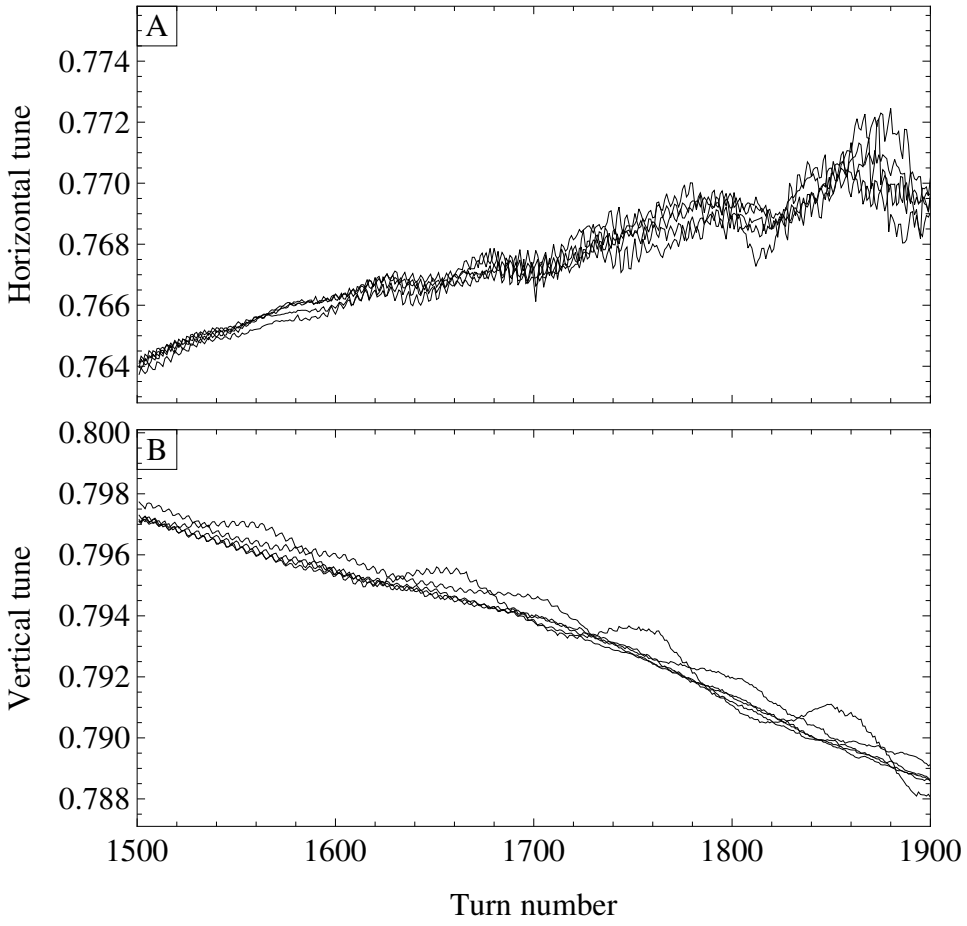

Figure 3.12: Measured horizontal (A) and vertical (B) tunes in the Booster for turns 2000 through 2250, which is the same time period analyzed for beta function measurements shown in Fig. 4.9. The tune was calculated using the FFT interpolation algorithm SUSSIX (see Ref. [24]), using sliding bins of 100 turns each. The expected precision of tune calculation with 100 turns using SUSSIX is $\sim 1/N^2 = 0.0001$, but in the Booster the tune changes by about 0.002 during those 100 turns. For beta function calculations the tunes were calculated using 100 turns, and the estimated uncertainty $\sigma_\nu = 0.001$.

the magnet current setting and reading is 0.11 amps.

3.3 Summary

In this chapter we have discussed two methods for measuring the beta function in a real machine. In the Linear Optics from Closed Orbits (LOCO) method, the response of the closed orbit to each of j dipole corrector magnets is measured at each of i BPMs in the machine, which makes up an orbit response matrix (ORM) of $i \times j$ measured data points. Least-squares fitting is then used to find the set of model parameters (focusing errors, BPM and dipole calibrations) that minimizes the difference between the measured orbit responses and the model predictions. If enough corrector quadrupoles are present, the focusing errors found from LOCO can directly be used for correcting beta beating. Calibration of the lattice model also makes the results of any beam dynamics simulations more accurate and can be useful for modeling complex beam behavior such as beam loss near resonances.

In the second method, K-modulation, the value of the beta function at the location of each corrector quadrupole is calculated by measuring the tune shift resulting from changing the focusing strength of that quadrupole. This method is model-independent, so the results are equally valid even if there are large discrepancies between the lattice model and the real machine. But this method provides no information about the behavior of the beta function anywhere in the ring except for where corrector quadrupoles are located, and it provides no information about what sort of focusing errors cause the optics

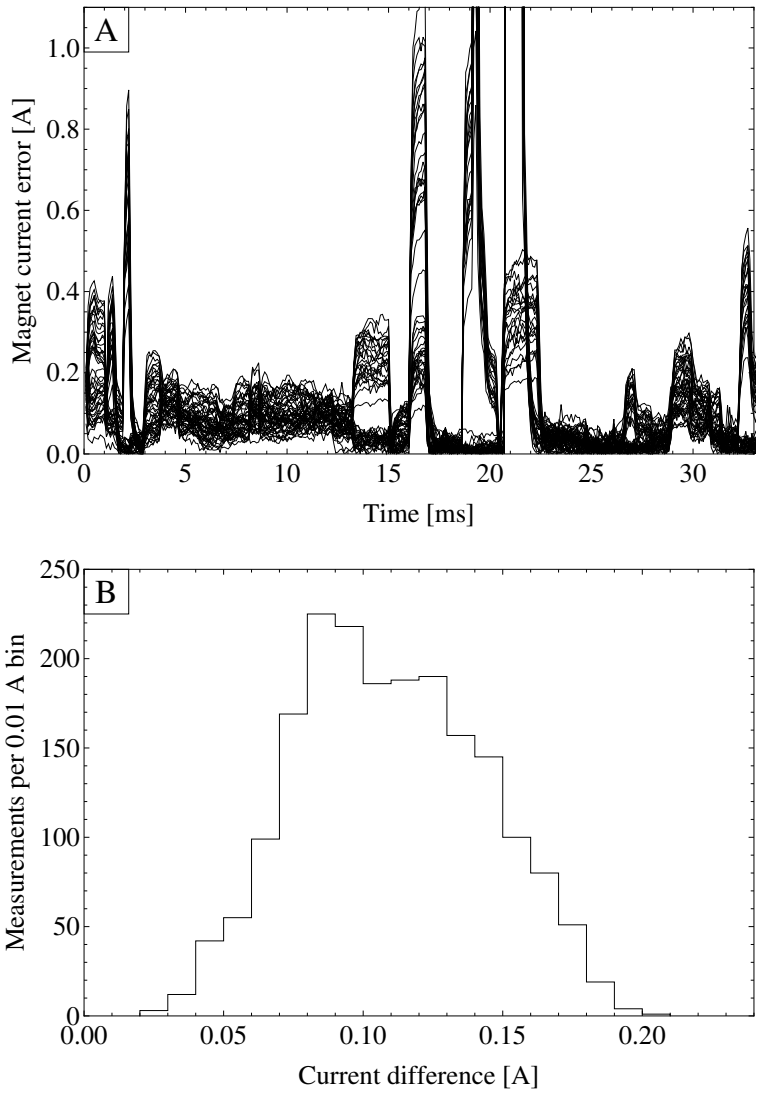

Figure 3.13: (A) shows the magnitude of the difference between desired magnet current and the power supply readout, $|I_{read} - I_{set}|$, throughout the 33 millisecond acceleration ramp for each of the Booster's 48 quadrupole magnets. The error in power supply current reading is roughly proportional to the rate of change of the magnet current with time. (B) shows a histogram of the magnet current differences during the time from 4 ms to 12 ms. The RMS error in the magnet current, $|I_{read} - I_{set}|$, is 0.11 amps.

distortions.

A precise measurement of the beta function is a first step for ensuring good performance in a real machine. Then, if the measured distortions are large, it may be necessary to correct them in order to reduce beam losses. The next two chapters will discuss the application of these techniques in the FNAL Booster and in the CERN PS Booster.

Chapter 4

Optics measurements in the FNAL Booster

This chapter discusses the measurement of optics in the FNAL Booster using the techniques described in Chapter 3, Linear Optics from Closed Orbits (LOCO) and k-modulation. Corrections for coupling and beta beating were also implemented.

Precise optics measurements and corrections had not been possible in the Booster until relatively recently, with the installation of the new corrector magnet system. Previous attempts had been made to implement LOCO [25] using the old set of correctors, and these measurements indicated that the focusing errors in the Booster's combined function magnets fell within design tolerances. But the limitations of the corrector magnet system made it impossible to make more precise measurements of the optics, or to make any corrections to observed optics perturbations.

The chapter begins with a description of the experimental setup and some of the technical details of the data collection process in the Booster. Section 4.2 describes the implementation of LOCO. Since it is necessary to correct transverse coupling before measuring the linear optics, we first discuss the implementation of transverse coupling corrections. We then show the

results of the lattice model calibration from LOCO analysis of orbit response measurements in the uncoupled machine and discuss the possible origins of model parameter errors. Section 4.3 describes k-modulation measurements in the Booster. The beta functions obtained using this method are presented in Section 4.4, along with those obtained using LOCO. And then in Section 4.5, we discuss the implementation of corrections for beta beating.

4.1 Description of experiment setup

In this section we give a brief description of the experimental setup. Further details about the hardware and software used for data collection can be found in Appendix 1.

The optics measurements described in this chapter were performed on beam pulses that were specially set up for machine studies. Both of the optics measurement techniques discussed in Chapter 3 are destructive, so these measurements are not made on beams that will be transferred to downstream machines. The dedicated study cycles on which these measurements are performed are extracted to a beam dump after they are accelerated in the Booster. These cycles are inserted among cycles that are destined for the various downstream machines, allowing machine studies to be conducted parasitically during normal operations without interfering with the high-energy physics experiments.

Before making optics measurements, one would ideally put the machine into a steady state in which the beam energy, magnet strengths, and all other

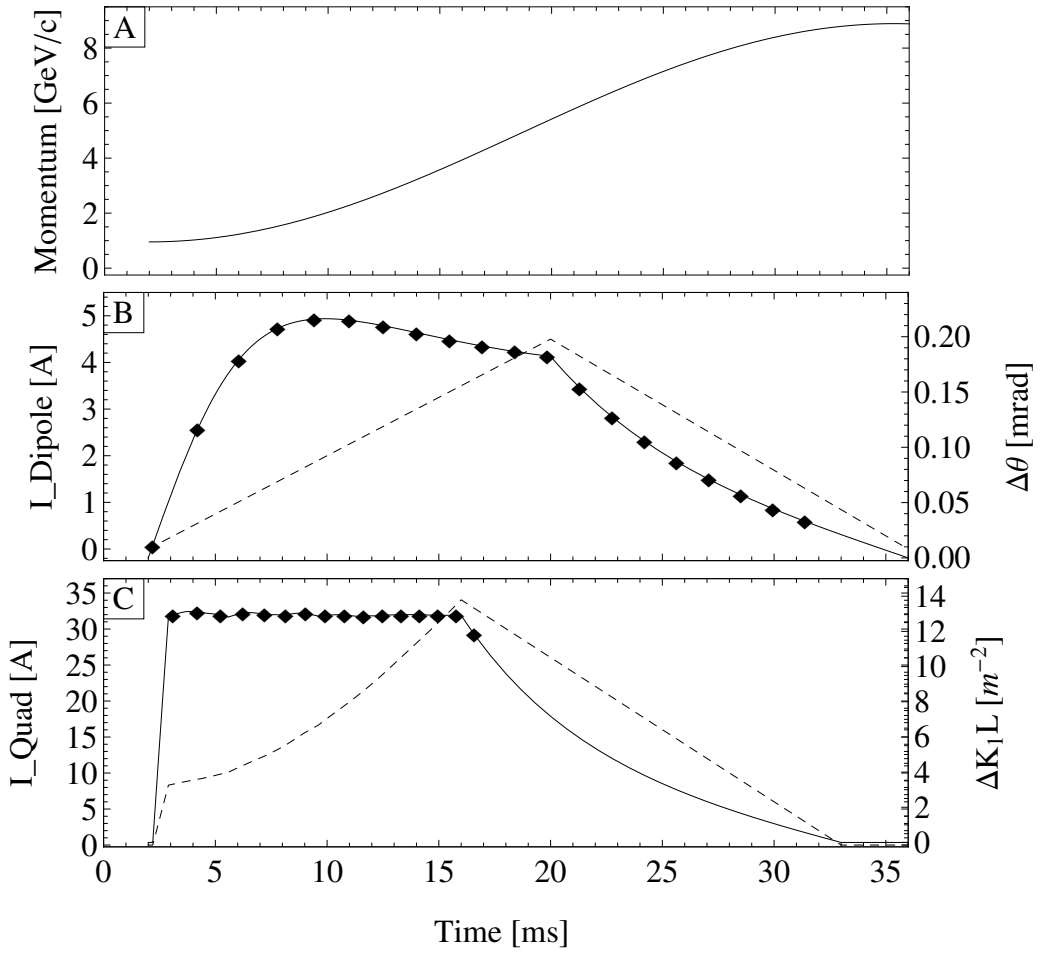

Figure 4.1: (A) Beam momentum throughout the acceleration ramp in the FNAL Booster. (B) Dipole magnet current ramp used for orbit response measurements (dashed line) and the corresponding angular kick produced by the magnet (solid line), which is directly proportional to magnet current and inversely proportional to the beam momentum. The black diamonds indicate times during the acceleration ramp at which orbit measurements were made. (C) Quadrupole magnet current ramp used for quadrupole modulation tune measurements (dashed line) and the corresponding focusing strength (solid line), which is directly proportional to magnet current and inversely proportional to the beam momentum. The black diamonds indicate times during the acceleration ramp at which tune measurements were made.

parameters are held constant. When the machine is in a steady state the beam position can be measured over a large number of turns, reducing the effects of noise in the BPMs and allowing for more precise determination of the closed orbit position. Likewise, the tune determination from an FFT is more precise when a large number of turns are used for the calculation. But since the Booster's magnets are powered on a resonant circuit it is not possible to alter the energy versus time ramp for the beam, so beam parameters such as closed orbit position and betatron tune are always changing. Beam position measurements must be limited to a relatively small number of turns during which the machine's parameters are approximately constant. These measurements are repeated at fixed intervals throughout the acceleration cycle.

Figure 4.1A shows the momentum ramp in the Booster during the 33 millisecond acceleration cycle. The dipole and quadrupole current perturbations used for orbit response and tune response measurements must also increase with time so that the effective strengths of the magnets stay approximately constant as momentum increases.

Figure 4.1B shows the current ramp used for the dipole magnet bumps for orbit response measurements (dashed line) and the corresponding angular kick $\Delta\theta$ (solid line). The black diamonds indicate the times at which orbit measurements were made, which were at fixed time intervals of about 1.5 milliseconds. The angular kick during the second half of the acceleration cycle is smaller than during the first half due to limitations imposed by the hardware controlling the magnets.

Figure 4.1C shows the current ramp used for the quadrupole magnet bumps for k-modulation measurements (dashed line) and the corresponding focusing strength $\Delta k_1 l$ (solid line) The black diamonds indicate the times at which tune measurements were made, which were at fixed intervals of 500 turns. The orbit and tune measurements do not always occur at the same time in the cycle because the orbit measurement system makes repeated measurements at fixed time intervals but the tune measurement system makes repeated measurements at fixed intervals of numbers of turns, and the revolution frequency increases as the beam is accelerated.

These studies were executed using Accelerator Scripting Language (ACL), which provides full control of reading and setting all hardware in the machine to allow for fast and accurate collection of large quantities of data.

4.2 LOCO method

Orbit response measurements and LOCO analysis were performed in the FNAL Booster as described in Section 3.1. The orbit response to 96 dipole orbit correctors (48 horizontal and 48 vertical) plus dispersion was measured at 102 BPMs (51 horizontal and 51 vertical), yielding an orbit response matrix containing 9894 data points. The 588 variable model parameters used in the LOCO fitting were normal and skew quadrupole errors, dipole calibration and tilt, and BPM calibration and tilt. The normal and skew quadrupole errors were modeled as thin imaginary "pseudo-quad" elements placed next to the corrector magnet packages in the machine lattice model, which allows for each

of the corrector quadrupole magnets to be used to compensate for the adjacent pseudo-quad error.

Orbit response measurements were first done on the machine in its normal operational configuration, in which there is significant coupling between the transverse planes. Coupling corrections were implemented based on these first LOCO results, and then the orbit response measurements were repeated with coupling corrections implemented. The following section describes the correction of transverse coupling and then discusses the model parameter errors found from LOCO analysis of the uncoupled orbit response matrix.

4.2.1 Correction of transverse coupling

The Booster normally operates with significant transverse coupling. To some extent this coupling was intentionally introduced, via empirical tuning, because it was observed that emittance exchange between the horizontal and vertical planes improves beam stability at high intensity.

Figure 4.2A shows the measured (thick gray line) and calibrated model (dashed black line) horizontal orbit response to a vertical dipole perturbation before the coupling was corrected. The calibrated lattice model contains a set of skew pseudo-quadrupole errors which are located next to the skew quadrupole corrector magnets, and with the addition of these errors the model reproduces quite well the observed opposite-plane beam response. In order to correct the coupling, the original settings of the skew quadrupole corrector magnets were replaced with strengths equal but opposite to the adjacent skew

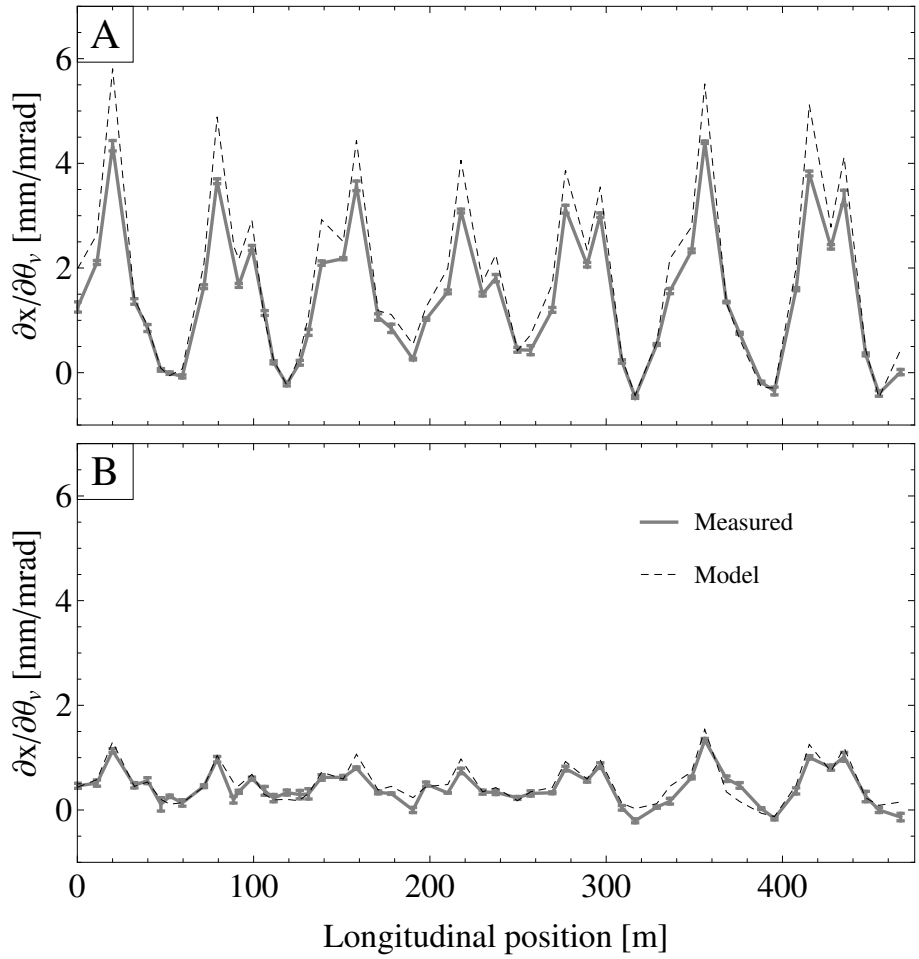

Figure 4.2: (A) shows the measured (solid gray line) and model (dashed black line) response of the horizontal closed orbit to a vertical dipole perturbation before coupling correction.(B) shows the measured (solid gray line) and model (dashed black line) response of the horizontal closed orbit to the same vertical dipole perturbation after coupling was corrected by replacing the original skew quad settings with values equal and opposite to the skew quad errors found from LOCO.

pseudo-quad errors found from LOCO. Figure 4.2B shows the horizontal orbit response to the same vertical dipole after the coupling has been corrected. The opposite-plane orbit response is greatly reduced.

Figure 4.3 shows the transverse coupling strength throughout the early part of the acceleration cycle, which was measured by varying the strength of the corrector quadrupoles to find the closest approach of the x and y tunes, as is shown in Fig. 2.14. These measurements were repeated while three different corrector magnet configurations were present in the machine. The solid line shows the coupling strength when the corrector magnets were in their typical operational settings, in which transverse coupling is strong at the beginning of the cycle. The dashed line shows the coupling strength after the coupling corrections found using LOCO were implemented. The dotted line shows the natural coupling of the uncorrected machine, measured during a special situation in which all corrector magnets were turned off. The machine is unstable without optics corrections in place, but it was possible to accelerate a very low intensity beam in order to make these measurements. Contrary to expectations, it was found that the transverse coupling in the bare machine is nearly as small as the coupling after corrections were implemented. Therefore the transverse coupling in the machine is not due to imperfections or misalignments in the main magnets, as was previously assumed. The coupling is caused largely by the settings of skew quadrupole corrector elements, with some additional contribution from misalignments to the corrector magnet packages.

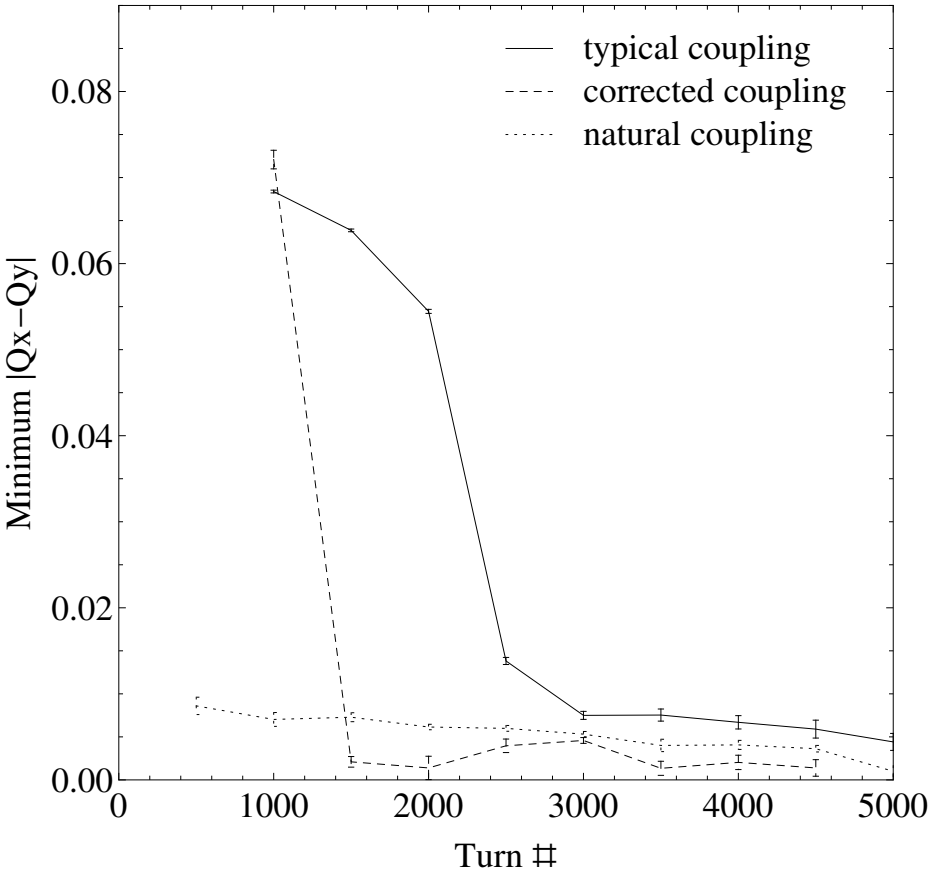

Figure 4.3: Measured coupling strength throughout the beginning of the acceleration cycle with three machine configurations: normal operational conditions (solid line), after coupling correction (dashed line), and the bare machine with no corrector magnets active (dotted line). The coupling strength was measured by varying the strength of the corrector quadrupoles to find the closest approach of the x and y tunes, as is shown in Fig. 2.14.

4.2.2 Fitting for model parameter errors

After transverse coupling was corrected, orbit response measurements and LOCO analysis were repeated on the uncoupled machine. This section discusses the model parameter errors found from LOCO analysis of the uncoupled orbit response matrix measurements.

Figure 4.4 shows the values for normal and skew focusing errors found from LOCO analysis. The error bars are calculated from the standard deviation among ten trials in which random error was added to each orbit response measurement (see Section 3.1.4). Although for LOCO fitting the focusing errors are treated as though they are localized next to the corrector magnet packages, in reality these focusing errors could be caused by any magnets anywhere in the ring. This distribution of errors localized in the corrector packages has the same effect on the linear optics as does the distribution of real focusing errors located throughout the ring.

Both the normal and the skew focusing errors have an RMS value of about 0.0006 m^{-1}, which is less than half of a percent of the nominal focusing strength of the main magnets ($k_1 l = 0.157\ m^{-1}$ for the focusing magnets, and $k_1 l = 0.167\ m^{-1}$ for the defocusing magnets). The scale of these errors is reasonable, considering that the measured gradient of the main magnets varies by several percent within the aperture area that the beam occupies, as is shown in Figure 1.8. A normal or skew focusing error of this magnitude could also be caused by feed-down effects, as discussed in Section 2.4, if the beam passes off-center through a sextupole corrector by about five millimeters.

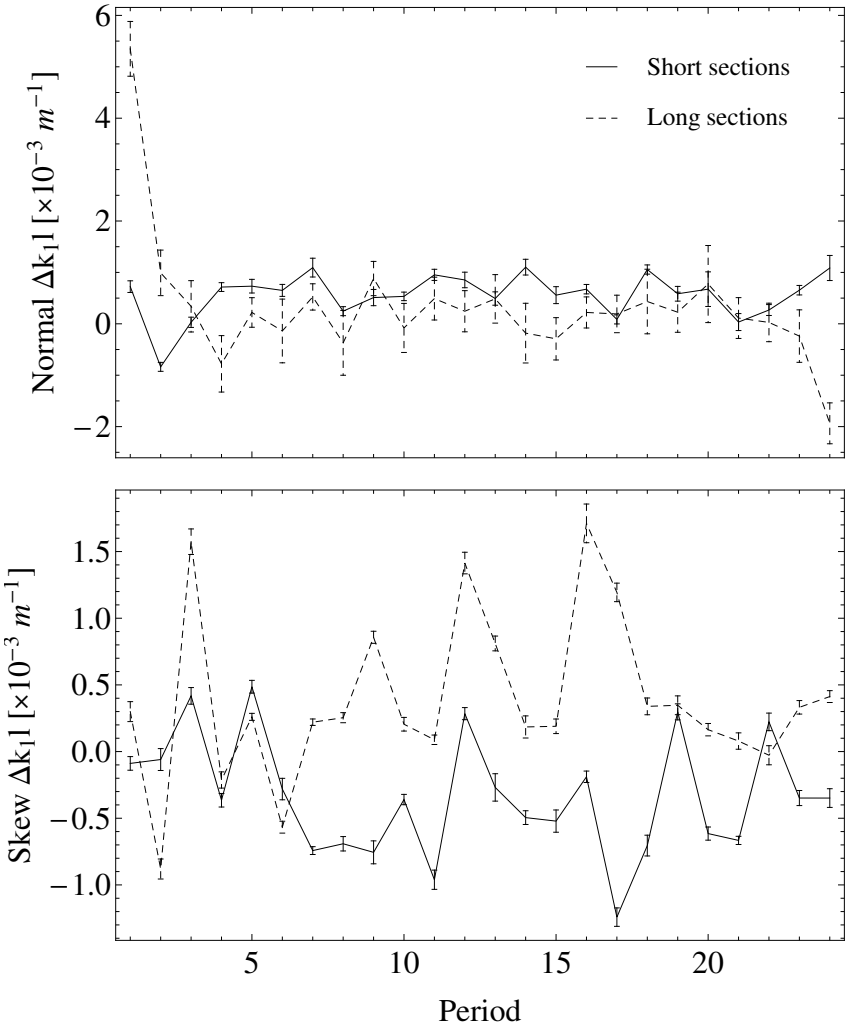

Figure 4.4: Fitted values for normal and skew quadrupole errors from LOCO, near the beginning of the acceleration cycle, at $t = 6$ ms. The solid line indicates values for the elements in short drift sections, and the dashed line indicates elements in long drift sections. The error bars correspond to the standard deviation among the results from ten trials in which random error was added to each orbit response measurement.

Figure 4.5 shows the values for dipole and BPM calibration errors found from LOCO analysis. The error bars are calculated from the standard deviation among ten trials in which random error was added to each orbit response measurement. The measured orbit response was found to be approximately 25% smaller than expected, indicating that a systematic calibration error exists for either the dipoles, the quadrupoles, or both. In this subsection we will examine possible explanations for this unexpectedly large systematic calibration error.

The size of the dipole kick used in orbit response measurements is calculated from the magnet's current setting and from test bench measurements of the magnetic field produced by a given current [26]. These measurements, which were performed before the magnets were installed, showed that the magnets were very uniform. The field per amp ratios measured for all dipoles have a standard deviation of 0.66 percent for horizontal dipoles and 0.58 percent for vertical dipoles.

In the machine, the field of these fast-ramping magnets is affected by eddy currents in the beam pipe [27]. Figure 4.6 shows the relation between the field produced by the dipole correctors outside of the beam pipe, $B_0(t)$, and the field inside the beam pipe, $B(t)$, which we expect to follow the form

$$\tau \frac{dB}{dt} + B(t) = B_0(t) \tag{4.1}$$

where τ is a time constant that characterizes the field lag. This time constant was measured experimentally by performing orbit response measurements with

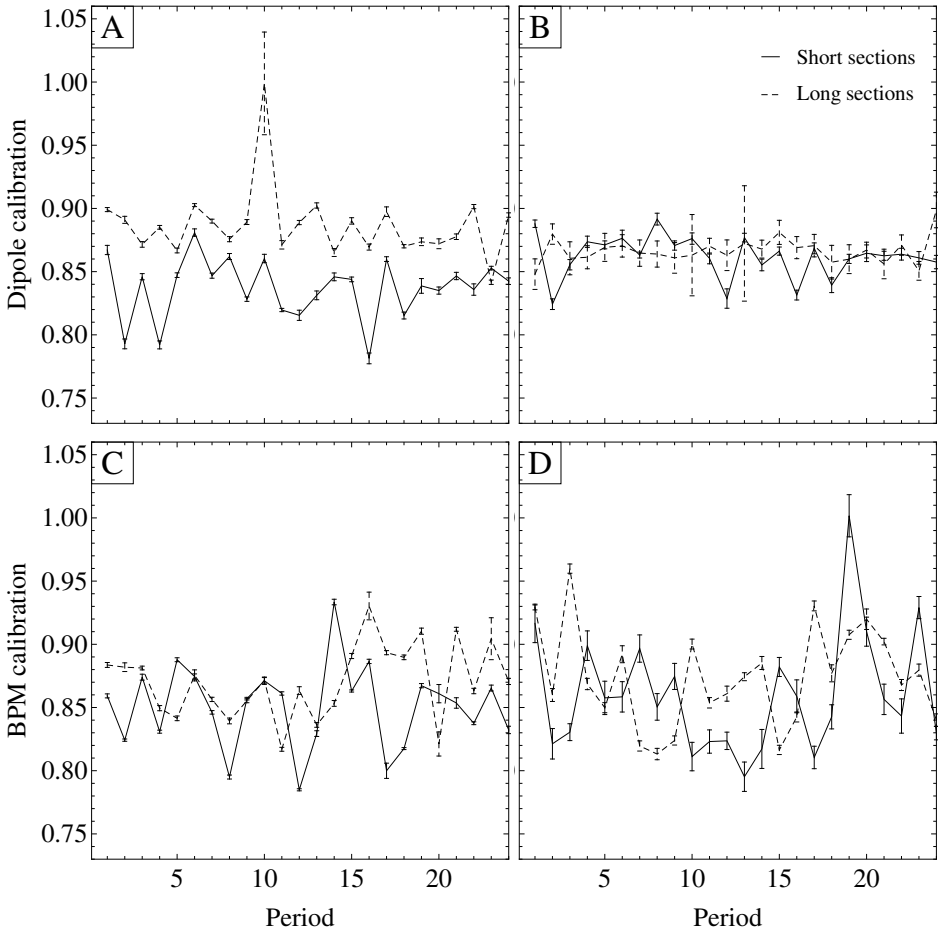

Figure 4.5: Fitted values for (A) horizontal dipole, (B) vertical dipole, (C) horizontal BPM, and (D) vertical BPM calibration errors from LOCO, near the beginning of the acceleration cycle, at $t = 6$ ms. The solid line indicates values for the elements is short drift sections, and the dashed line indicates elements in long drift sections. The error bars correspond to the standard deviation among the results from ten trials in which random error was added to each orbit response measurement.

different magnet current ramp rates, and then comparing the beam response in each case to determine the effective field felt by the beam. The eddy currents reduced the effective field by approximately 4%, and factoring these effects slightly reduced the apparent systematic calibration error observed during orbit response measurements.

In order to understand whether the systematic calibration error originates with the BPMs or with the dipoles, orbit response measurements were repeated using an ionization profile monitor (IPM). The IPM contains a microchannel plate inserted into the beam pipe. A voltage difference can be applied so that the residual gas that is ionized by the passing of the beam will drift to the microchannel plate. The transverse size and position of the beam are determined from a Gaussian fit of the ions counted in each channel [28]. The spacing between the channels is very well known, so it is highly unlikely that any calibration error will exist in the beam position given by the IPM.

Figure 4.7 shows the measured versus model prediction for orbit response to several dipoles. The black diamonds are the orbit response to fifteen dipoles, measured using the IPM. The gray dots are the orbit response to fifteen dipoles, measured using all BPMs in the ring. The gray dotted line has a slope of one. The gray dots lie roughly along a line whose slope is less than one, which is consistent with the earlier observation of a calibration error. The black diamonds lie along a line whose slope is very close to one; the measured and model orbit response are equal. This indicates that the calibration error lies with the BPMs, not with the dipoles.

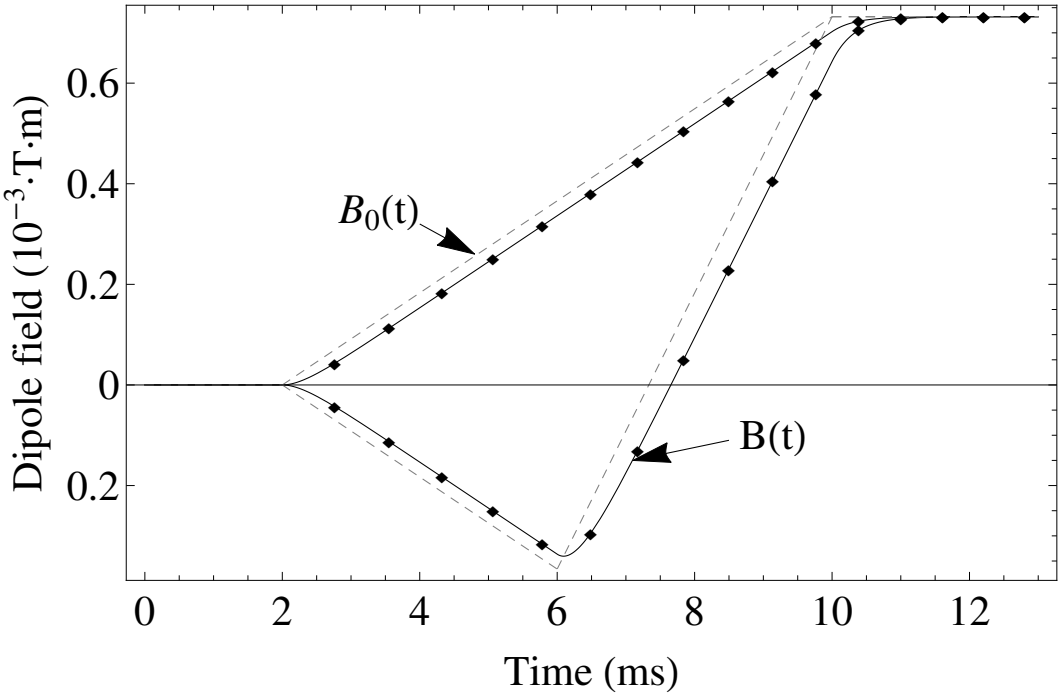

Figure 4.6: Dipole magnet ramps used to measure the effects of eddy currents on the field strength inside the beam pipe. The dashed lines show two ramp functions programmed into the magnets, one with a faster slew rate and the other with a slower. The diamond points indicate times in the acceleration cycle when orbit response measurements were made. The solid line shows the field acting on the beam, calculated by comparing the orbit response for slow vs. fast ramps and assuming that the relation between the magnetic field inside and outside of the beam pipe has the form of Eq. (4.1)

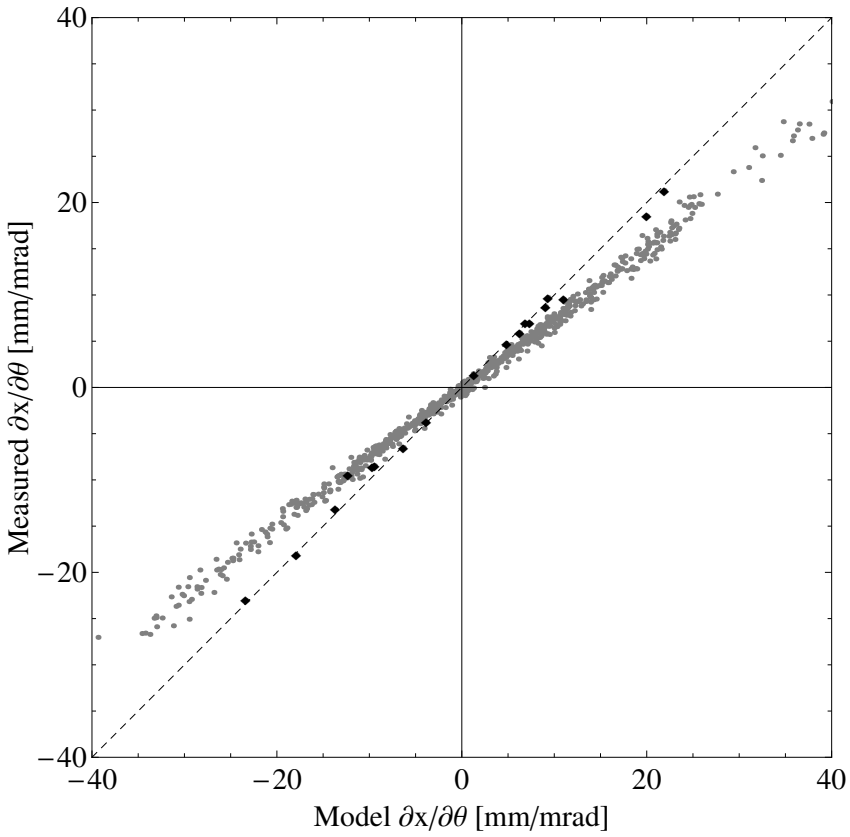

Figure 4.7: Comparison of measured and model orbit response, measured with BPMs and with an ionization profile monitor (IPM). The black diamonds are the orbit responses to fifteen dipoles, measured using the IPM. The gray dots are the orbit response to fifteen dipoles, measured using all BPMs in the ring. The dotted line has a slope of one. The gray dots lie roughly along a line whose slope is less than one, which is consistent with the earlier observation of a calibration error. The black diamonds lie along a line whose slope is very close to one; the measured and model orbit response are equal. This indicates that the calibration error lies with the BPMs, not with the dipoles.

Figure 4.8 shows the fitted values for the tilts (rotations around the s axis) for the horizontal dipoles, vertical dipoles, and BPMs. The error bars are calculated from the standard deviation among ten trials in which random error was added to each orbit response measurement. The horizontal and vertical pickup electrodes in the BPMs are in a single package, so a single tilt angle is assumed for each horizontal and vertical dipole pair.

4.2.3 Summary of LOCO results

Transverse coupling was successfully corrected using the skew quadrupole errors found from LOCO analysis. Orbit response measurements were then repeated on the uncoupled machine. The focusing errors found from LOCO fitting were of a reasonable scale, with an RMS value of less than 0.5% of the main magnet focusing strength. The measured orbit response was systematically about 20% smaller than expected, indicating a systematic calibration error in either the BPMs or the dipoles. Orbit response measured with an IPM were consistent with model predictions, which indicates that the calibration error is in the BPMs.

The beta functions obtained using LOCO will be discussed in Section 4.4, along with those obtained from k-modulation measurements.

4.3 K-modulation

After the transverse coupling in the Booster was corrected, beta function measurement were made using k-modulation, using the procedure dis-

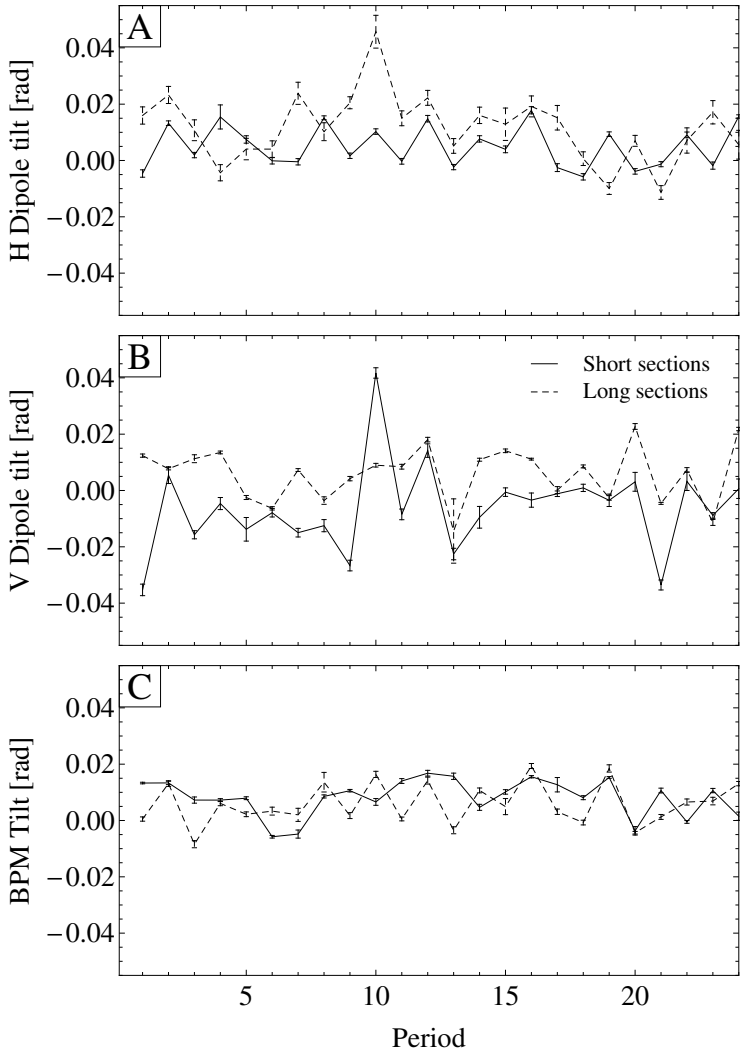

Figure 4.8: Fitted values for (A) horizontal dipole, (B) vertical dipole, (C) horizontal BPM, and (D) vertical BPM tilt errors from LOCO, near the beginning of the acceleration cycle, at $t = 6$ ms. The solid line indicates values for the elements is short drift sections, and the dashed line indicates elements in long drift sections. The error bars correspond to the standard deviation among the results from ten trials in which random error was added to each orbit response measurement.

cussed in Section 3.2. Measurements were made at 500-turn intervals during the first half of the acceleration cycle. At higher energy the fast kicker magnets are not strong enough to create a large coherent oscillation in the beam, and therefore tune measurements are very noisy. Since the machine's tune changes significantly on a timescale of a few hundred turns, the tunes were calculated using only one hundred turns of measured trajectory. Using such a small number of turns reduces the precision of the tune determination, but if more turns were used then the tune change during those turns would be larger than the tune resolution (see Fig. 3.12).

The beta functions obtained from k-modulation are shown in Section 4.4, along with those obtained using LOCO measurements.

4.4 Comparison of beta function measurements

Figure 4.9 shows the horizontal and vertical beta functions obtained from LOCO (gray band) and from k-modulation (black points). These measurements were made near the beginning of the acceleration cycle, two milliseconds after injection. The beta beating, $\delta\beta \equiv \frac{\beta-\beta_0}{\beta_0}$, is as large as 25% early in the cycle, and it decreases as the beam energy increases. This distortion is caused by the dogleg magnets, which is a set of four rectangular bending magnets that creates a closed orbit bump around the machine's extraction septum. The edges of these magnets have a focusing effect, which distorts the optical properties of the lattice. These magnets are powered with DC current, so their effective strength and the resulting beta beating decreases as the beam mo-

mentum increases. These magnets were predicted to have a significant effect of the optics [29], but this had not yet been confirmed experimentally.

Because the optics measurements made using LOCO and using k-modulation don't always happen at the same time during the acceleration cycle, it is not always possible to directly compare the results obtained using the two methods. But near the beginning of the acceleration cycle, where optics distortions are largest, the measurements made with both methods occur at the same time and so can be compared. Figure 4.10 shows a comparison of the beta functions obtained using LOCO and k-modulation measured at 2 ms and at 4 ms after injection. The histogram shows the difference between the beta functions obtained from LOCO, β_L, and the beta functions obtained from k-modulation, β_K, divided by the uncertainties added in quadrature, $\sqrt{\sigma_{\beta L}^2 + \sigma_{\beta K}^2}$. A total of 192 measurements is considered, which includes 48 measurements of the horizontal and 48 measurements of the vertical beta function made at the two time points. The mean is close to zero and the RMS is close to one, indicating good agreement between the two data sets.

4.5 Correction of beta beating

In theory, it should be as simple to correct beta beating using the results of LOCO calibration as it is to correct transverse coupling. In most machines the initial lattice model used for LOCO corresponds to the "ideal" optics and produces symmetric, regular linear optics functions, and LOCO calibration finds the set of small differences between this ideal optics and the

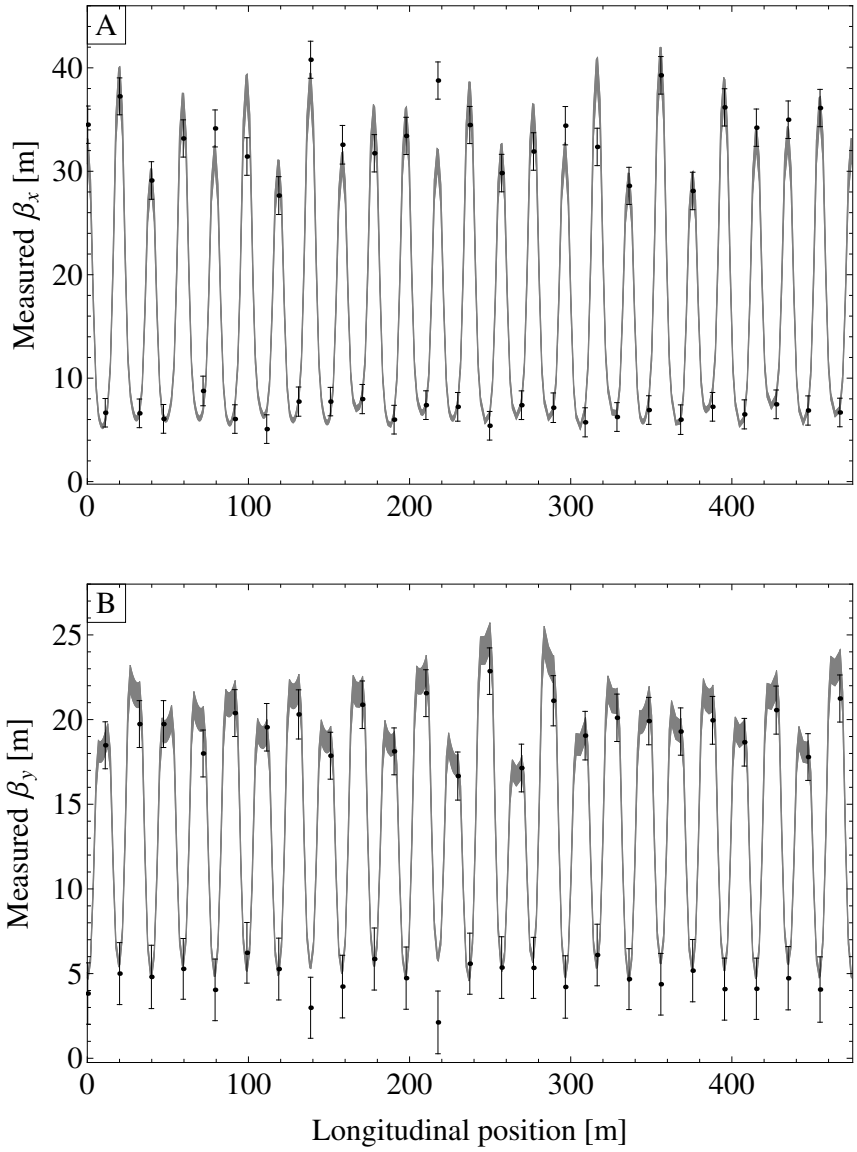

Figure 4.9: Beta function measured in the Fermilab Booster two milliseconds after injection. The black points show the beta function measured using quadrupole modulation, and the error bars indicate a one-sigma confidence interval. The gray band is a one-sigma confidence interval for the beta function given by the model after LOCO calibration. Error analysis is discussed in sections 3.1.4 and 3.2.2.

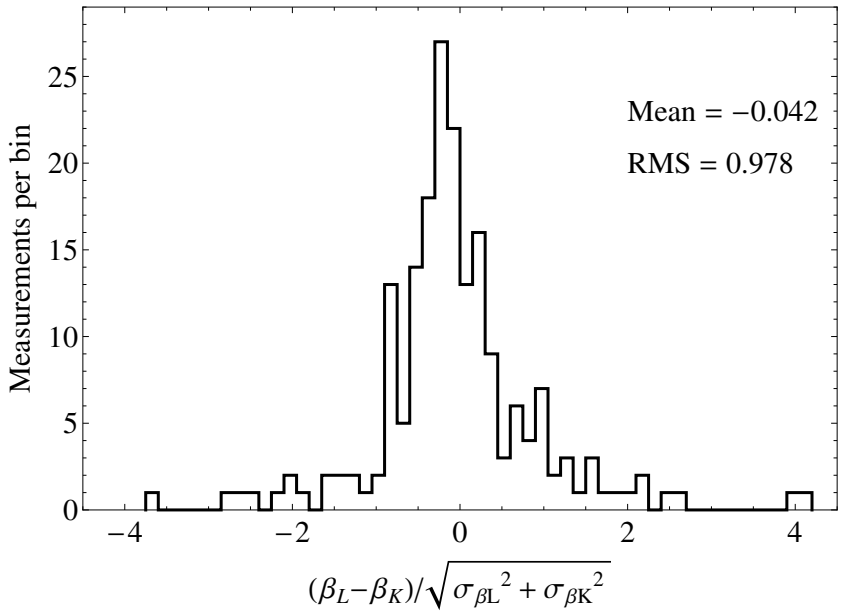

Figure 4.10: The histogram shows the difference between the beta functions obtained from LOCO, β_L, and the beta functions obtained from k-modulation, β_K, divided by the uncertainties added in quadrature, $\sqrt{\sigma_{\beta L}^2+\sigma_{\beta K}^2}$. A total of 192 measurements is considered, which includes 48 measurements of the horizontal and 48 measurements of the vertical beta function made at two times in the acceleration cycle, two and four milliseconds after injection. The mean is close to zero and the RMS is close to one, indicating good agreement between the two data sets.

optics of the real machine. If these differences are compensated for by setting the normal quadrupole corrector magnets with strengths equal but opposite to the adjacent skew pseudo-quadrupole errors found from LOCO, then the ideal, symmetric optics should be restored.

However, in the Booster, the observed beta beating is not caused by some random distribution of focusing errors around the ring. The main cause of the optics distortions is the edge focusing from the bending magnets in the extraction dogleg. This effect is included in the initial lattice model used for LOCO fitting, so the initial model already reproduces most of the beta beating observed in the real machine. In theory we could try to use an "ideal," symmetric model as the starting point for LOCO calibration in the Booster, rather than the realistic model that has the dogleg effect included. But in reality this approach does not work because the discrepancy between the initial model and the real parameters is too large, and the nonlinear least-squares fitting process gets stuck in some local minimum in parameter space and does not find a good solution.

Instead, the quadrupole settings used to correct beta beating were found using a trial-and-error approach. The calibrated lattice model was loaded into the lattice modeling program OptiM, which has a graphical user interface. The corrector quadrupole strengths were adjusted based on visual inspection to make the beta function predicted by the model was symmetric. These quadrupole settings were then loaded into the machine, and LOCO measurements were repeated.

Figure 4.11 shows the beta functions obtained from LOCO analysis, both before and after beta beating corrections were implemented. The gray band is a one-sigma confidence interval for the beta function before correction, and the black band is a one-sigma confidence interval for the beta function after beta beating correction. These measurements were made shortly after injection, when beta beating was most severe. The maximum beta distortion was reduced from about 25% to about 5%.

Figure 4.12 shows the maximum beta beating throughout the beginning of the acceleration cycle, when beta distortions were most severe. The dashed lines show the maximum horizontal (black) and vertical (gray) beta beating under typical operational conditions, before corrections were implemented. The solid lines show the maximum horizontal (black) and vertical (gray) beta beating after corrections were implemented using the corrector quadrupole magnets. The quadrupole corrector settings successfully corrected beta beating throughout the acceleration cycle.

4.6 Summary

This chapter discussed the measurement and correction of linear optics in the FNAL Booster. Until the relatively recent installation of the new corrector package magnets in the Booster, it had not been possible to measure optics with this degree of precision. Systematic correction of transverse coupling and beta beating had also not been possible before the installation of these magnets

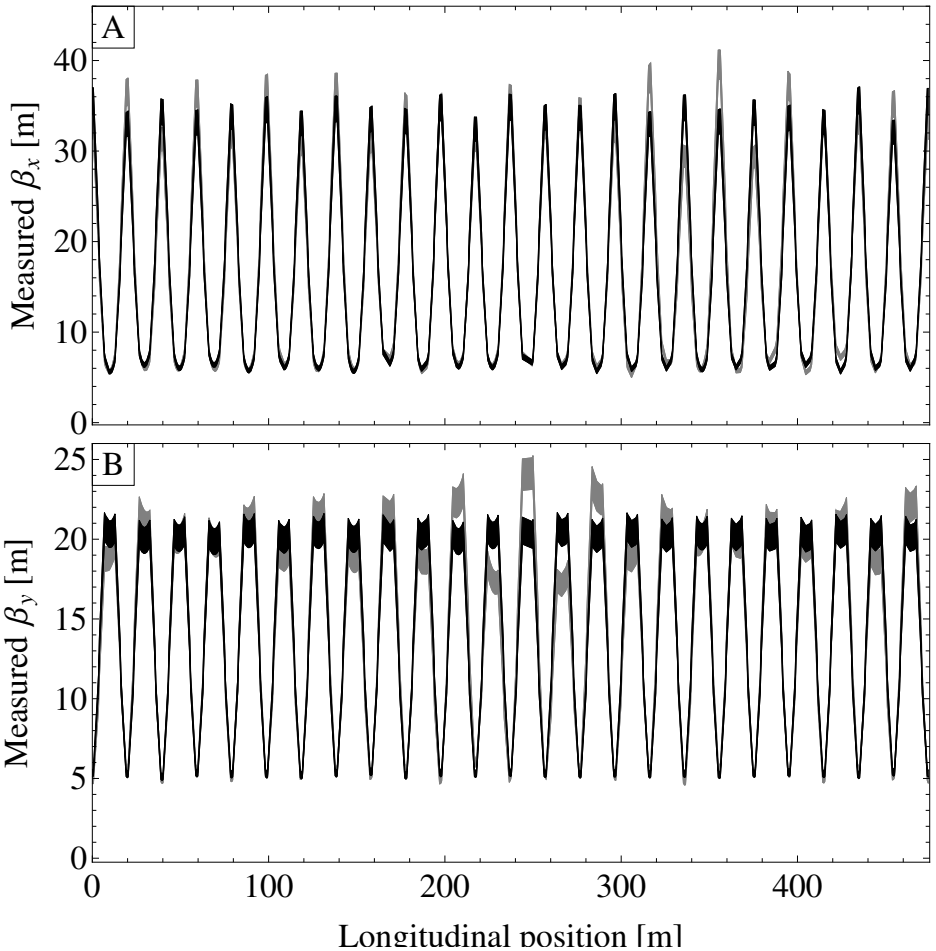

Figure 4.11: Beta function measurements in the Fermilab Booster, before and after beta beating corrections were applied. The gray band shows a one-sigma confidence interval for the beta function obtained from LOCO, measured two milliseconds after injection, with typical operational magnet settings. The black band shows a one-sigma confidence interval for the beta function obtained from LOCO, measured two milliseconds after injection, after beta beating corrections were implemented using the quadrupole corrector magnets. Error analysis is discussed in sections 3.1.4 and 3.2.2.

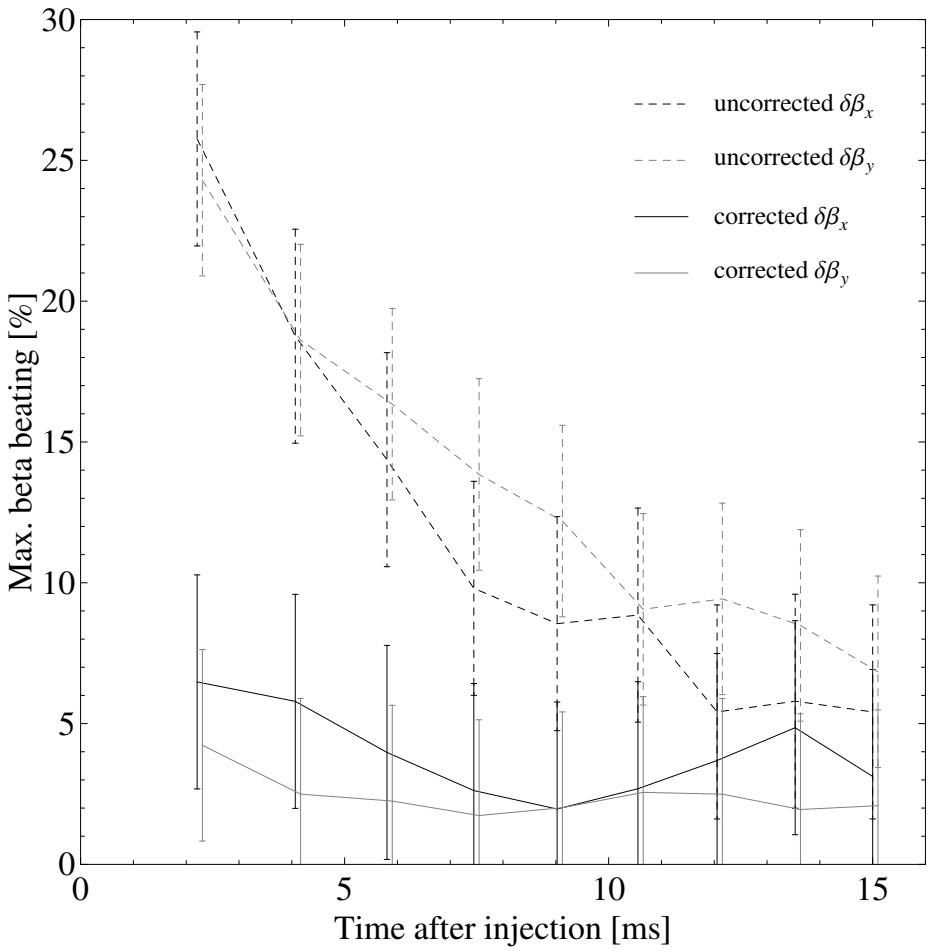

Figure 4.12: Maximum beta beating $\delta\beta \equiv \frac{\beta-\beta_0}{\beta_0}$ throughout the first half of the acceleration cycle, measured using LOCO. The dashed lines show the maximum horizontal (black) and vertical (gray) beta beating under typical operational conditions, and the solid lines show the maximum horizontal (black) and vertical (gray) beta beating after corrections were implemented using the corrector quadrupole magnets.

Before an accurate measurement of the beta functions could be made, it was necessary to correct transverse coupling. This was achieved by using the skew quadrupole corrector magnets to compensate for the skew pseudo-quad focusing errors found from LOCO. After coupling correction, k-modulation measurements were made and orbit response matrix measurements were repeated on the uncoupled machine.

The pseudo-quad focusing errors found using LOCO were not very large, having an RMS value of less than half of a percent of the nominal focusing strengths of the combined function magnets. The focusing errors could be caused by variation of the gradient in the combined function magnets, which was measured to be around one percent within the transverse aperture occupied by the beam. Focusing errors of this magnitude could also be the result of feed-down effects from the transverse offset of sextupole corrector magnets. The optics distortions caused by these errors is much smaller than that due to edge focusing in the dogleg bending magnets, which is the main cause of beta beating.

The measured beam response was about 20% smaller than the model predictions, indicating that there is a systematic calibration error in either the BPMs or the dipoles. Orbit response measurements made with an IPM indicate that the calibration error is in the BPMs.

The beta functions measured using LOCO and k-modulation agree within the uncertainty of the measurements. The maximum beta beating is 25% near the beginning of the acceleration cycle, and it decreases as the

beam energy increases. This is because the dogleg magnets which cause the optics distortion are powered with a constant current, so their effect becomes weaker as beam rigidity increases.

Beta beating was successfully corrected throughout the acceleration cycle, reducing the amplitude of the beta beating to about five percent. Presently these corrections have only been used during machine studies, but modifications to the control system are underway which will facilitate the implementation of these beta beating corrections during normal machine operations.

Chapter 5

Optics measurements in CERN PS Booster

In this chapter we present the results of linear optics measurements in the CERN PS Booster using the LOCO technique described in Chapter 3. This chapter begins with a description of how orbit response measurements were made in the PSB, which was slightly different from the method described in Chapter 3. In order to better understand how the focusing errors found using LOCO depend on the machine lattice settings, these measurements were made at three different working points, in which the betatron tunes were changed by a half or a whole integer. The second section shows the results of the LOCO fitting at multiple working points. The third section discusses error analysis and explores various ways that errors can be introduced in the fitting process, including the effects of including too many fitting parameters and the effects of faulty data. The last section describes how the focusing errors found using LOCO were used to improve the accuracy of simulations of beam losses near the half integer resonance. No beta beating corrections were made because a sufficient set of corrector quadrupoles was not available in the machine, but the observed perturbations were acceptably small.

5.1 Measurement method

The energy ramp of the PSB can be changed arbitrarily, so orbit response measurements were done during a long ($\sim$ 200 millisecond) plateau during which the beam energy and all other parameters were fixed. Figure 5.1 shows the beam energy (A), the dipole current (B), and the horizontal orbit at one BPM (C) throughout the acceleration cycle. Since all beam parameters are constant during energy plateau, position vs dipole kick can be measured continuously instead of at short discrete time intervals. These measurements were repeated with both positive and negative dipole current bumps.

Figure 5.2 is an example of one orbit response measurement in the PSB. The orbit was measured at 1 millisecond intervals during the 200 millisecond energy plateau while the dipole magnet current was varied, as is shown in Figure 5.1. The orbit response is calculated from a linear fit of the 200 values of position vs. kick measured during each beam pulse. This method results in a much more precise measurement because more data points are available, and because it eliminates the effects of random orbit variations from cycle to cycle.

An important goal of LOCO analysis in the PSB is to determine a realistic distribution of focusing errors that can be added to the lattice model to make multi-particle beam dynamics simulations more accurate. These simulations may investigate beam dynamics with various betatron tune working points, so it is useful to understand if and how the distribution of focusing errors changes when the quadrupole magnet settings change. In order to ex-

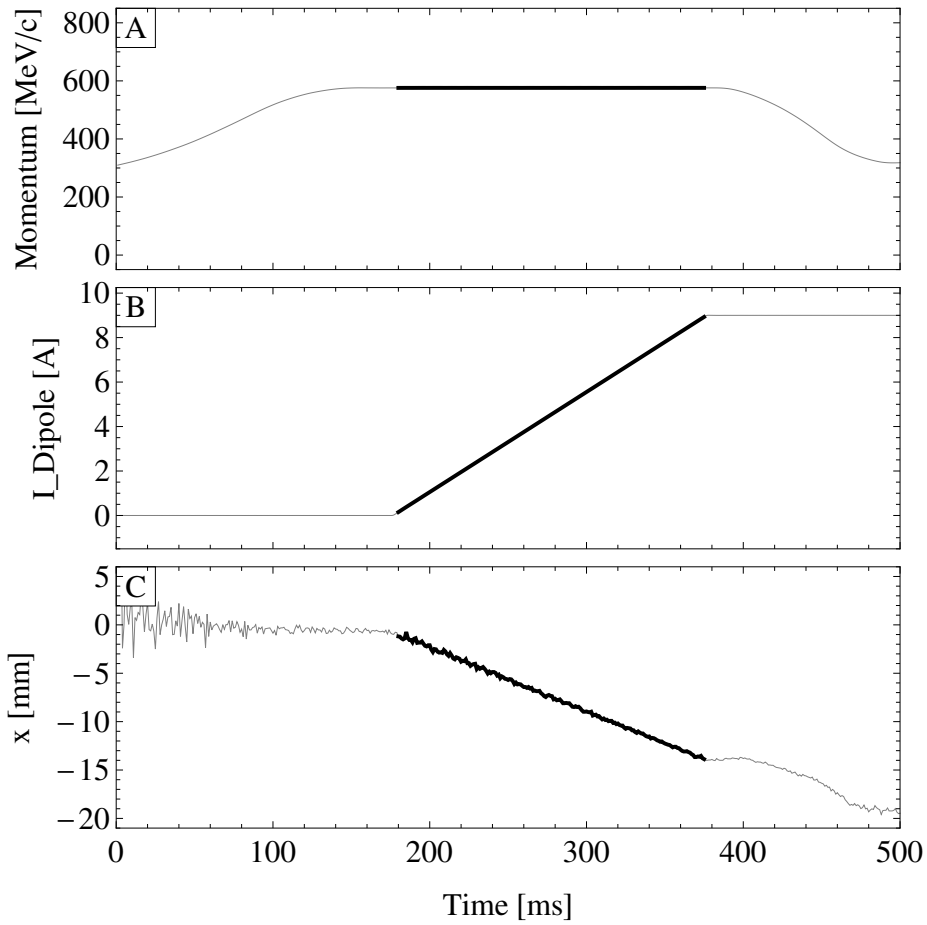

Figure 5.1: The gray lines show the beam momentum throughout the CERN PS Booster's $\sim$ 500 millisecond acceleration cycle (A), the dipole magnet current ramp used for orbit response measurements (B), and the closed orbit position measured at one BPM (C). The black line indicates the portion of the acceleration cycle during which an orbit response measurement was made. Measurements were repeated with both positive and negative dipole bumps.

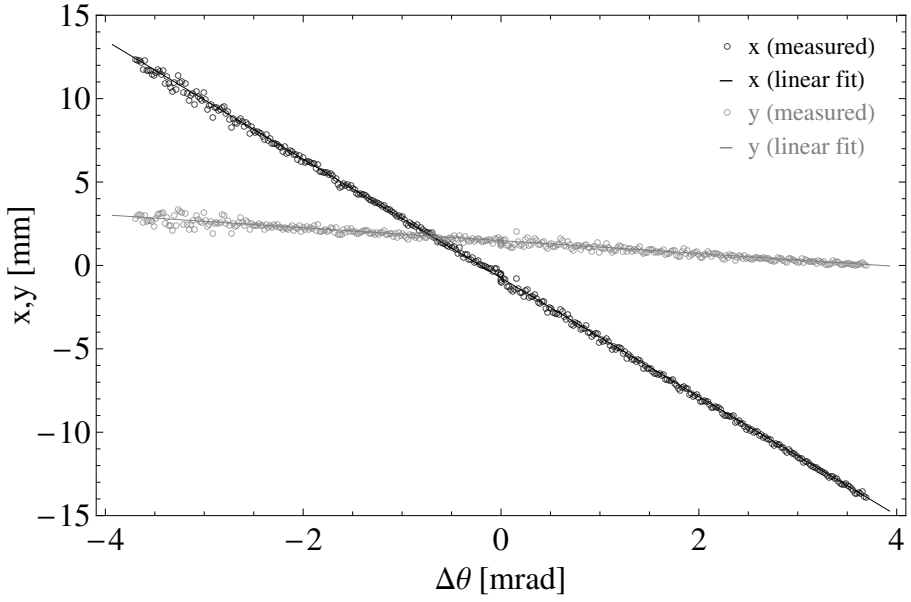

Figure 5.2: The black circles indicate the horizontal orbit position and the gray circles indicate the vertical orbit position measured at one millisecond intervals during the 200 millisecond energy plateau, as shown in Fig. 5.1. The black and gray lines are linear fits to the horizontal and vertical position vs. angular kick. The data shown here was collected during two beam pulses; the dipole magnet was ramped from 0 to +4 mrad during one beam pulse, and then ramped from 0 to -4 mrad during another beam pulse.

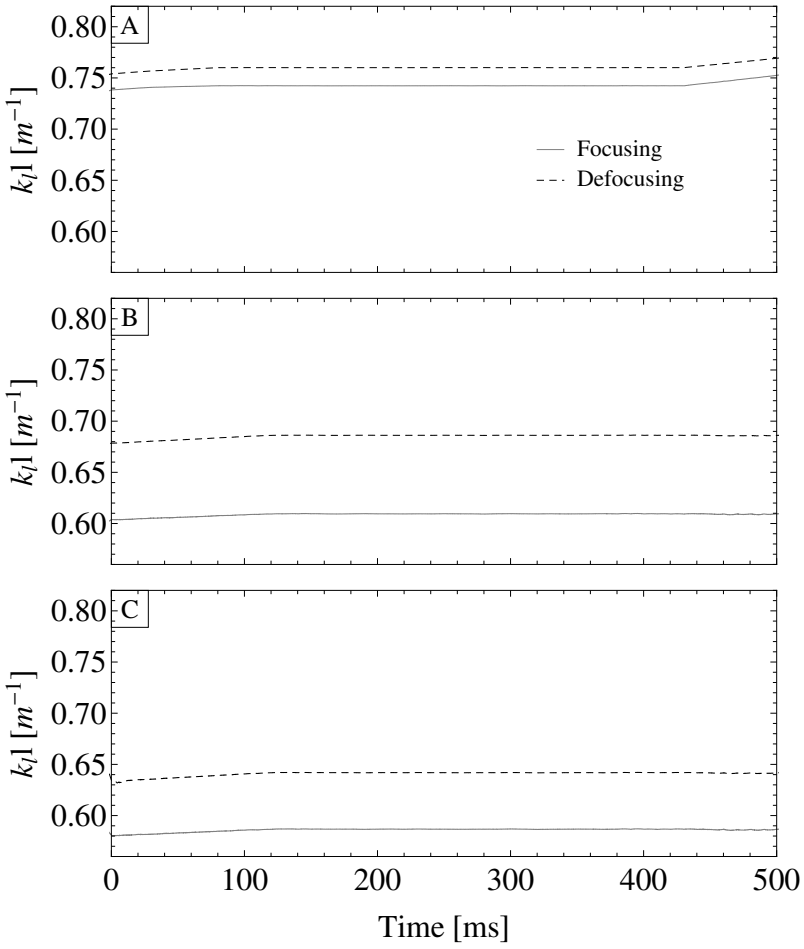

Figure 5.3: Focusing (gray line) and defocusing (dashed black line) triplet quadrupole strengths used during the ORM measurements made at three tune working points. (A) shows the quadrupole settings that produce tunes of $Q_x = 4.23, Q_y = 4.38$, which is a typical working point for the PSB. (B) shows the quadrupole settings that reduce the horizontal tune by one integer, producing tunes of $Q_x = 3.23, Q_y = 4.38$. (C) shows the quadrupole settings that reduce the horizontal tune by one integer and the vertical tune by a half integer, producing tunes of $Q_x = 3.23, Q_y = 3.88$.

amine how the focusing errors in the machine depend on the magnet lattice settings, three sets of orbit response measurements were made in which the machine lattice was altered to produce three different betatron tune working points. Figure 5.3 shows the strengths of the focusing and defocusing magnets that produce (A) the typical operational betatron tunes, (B) a configuration used only for these studies in which the horizontal tune was decreased by one integer and the vertical tune was unchanged, and (C) a second configuration used only for these studies in which the horizontal tune was decreased by one integer and the vertical tune was decreased by half an integer.

5.2 Fitting of variable model parameters

Nonlinear least squares fitting was performed for the CERN PS Booster as described in Section 3.1. The orbit response to 26 dipole orbit correctors (13 horizontal and 13 vertical) and dispersion were measured using 32 BPMs (16 horizontal and 16 vertical). Transverse coupling and opposite-plane orbit response to dipole perturbations are small in the PSB so only same-plane responses, i.e. horizontal orbit response to horizontal dipole kicks and vertical orbit response to vertical dipole kicks, were used in the least-squares fitting.

The PSB has only four pairs of independently-controllable quadrupole corrector magnets, and four focusing parameter variables do not provide enough degrees of freedom to obtain a good fit. Instead of using the corrector quads as the variable model focusing parameters, focusing errors were assigned to the 16 defocusing quadrupoles in the focusing triplets and the 16 pairs of focus-

ing quadrupoles in the focusing triplets. A single focusing error was assigned to the pair of focusing quadrupoles in each period because treating the two magnets independently resulted in degeneracy in the fitting and poor fit results, as will be discussed in the next section. The calibrations of the 26 orbit correctors and the 32 BPMs were also used as variable parameters. The orbit response matrices measured for each ring and at each tune working point were analyzed independently.

Figure 5.4 shows the resulting dipole and BPM calibrations for one ring of the PSB, calculated from the measurements made at the three different working points. Figure 5.5 shows the focusing errors and the resulting beta beating for the ring, calculated from the measurements made at the three different working points. Focusing errors found from LOCO are at most a few per mil of the nominal strength, which is in reasonable agreement with what we could expect based on the manufacturing tolerances and and field calculations for these magnets.

The maximum beta beating is less that 5%, which is acceptably small. No beta beating corrections are required. It is likely that corrections will be needed in the future, so it is beneficial to have established a method for optics measurements and corrections. As part of the intensity upgrades in the PSB, the injection scheme will be changed during the next few years, and this will inevitably introduce perturbations to the focusing lattice. It is likely that this change will result in beta beating that is large enough to affect the beam stability, so correction will be necessary.

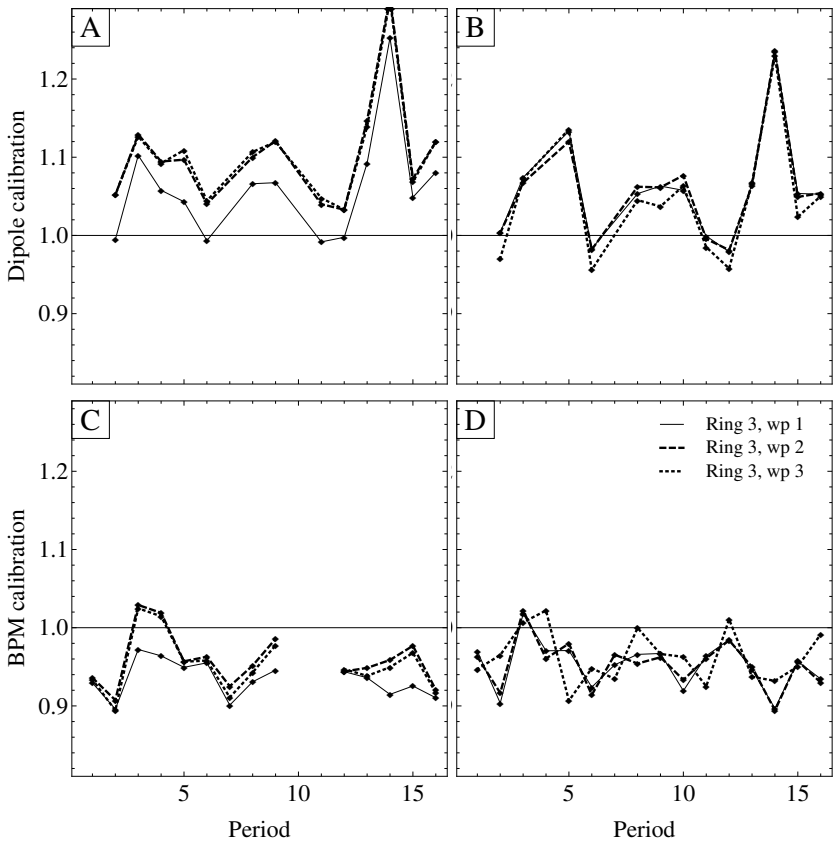

Figure 5.4: Calibration of (A) horizontal dipole correctors, (B) vertical dipole correctors, (C) horizontal BPMs, and (D) vertical PBMs from LOCO in Ring 3 of the PSB. The results of measurements made at three working points are shown.

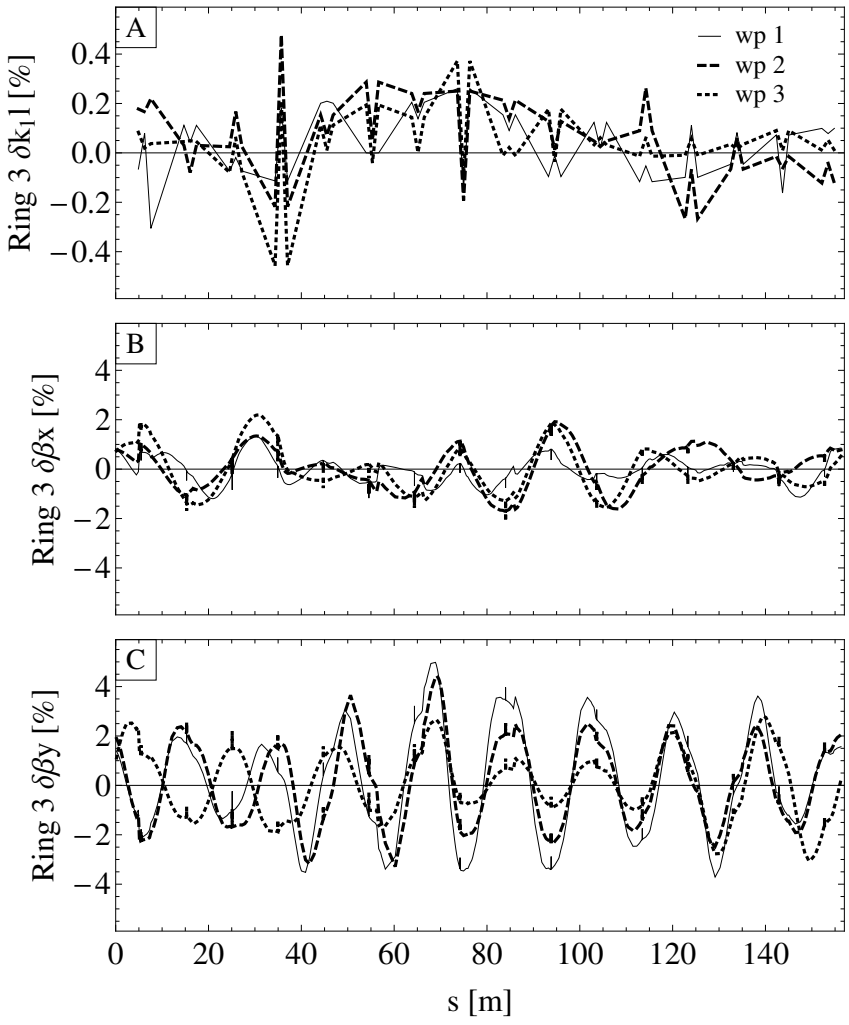

Figure 5.5: (A) shows the normal focusing errors found from LOCO in Ring 3 of the PSB. The results of measurements made at three different working points (see Fig. 5.3) are shown. (B) shows the horizontal beta function given by the model after LOCO calibration, and (C) shows the vertical beta function given by the model after LOCO calibration. The maximum beta beating is no more than 5% in any case, which is acceptably small. The beta beating propagates with a frequency of twice the betatron tune (see Section 2.4.4).

5.3 Error Analysis

Standard errors for the fitted parameter values were calculated analytically and using numerical simulation, as discussed in Chapter 3.1.4. The orbit response measurements in the PSB are extremely precise, and therefore the standard errors on fitted parameters are very small, on the order of about 10% for focusing errors and less than 1% for dipole and quadrupole calibration parameters (see Fig. 3.9).

Figure 3.10 showed the variation in optics parameters calculated from ten trials of simulated data, in which normal random errors were added to the measured orbit response matrix. The standard deviations, which are about 4%, are used as the uncertainty in the beta function calculation.

Close examination of the orbit response measurements shows that the orbit vs. kick measured by certain BPMs was not linear, as it is expected to be. Figure 5.6A shows an orbit response measurement made with a BPM located in period 10, which has a highly nonlinear response. It is likely that this nonlinear response was caused by beam loss upstream of the BPM; particles striking the BPM plates would affect the voltage signal, and therefore the calculated position. However, beam loss monitors were not available to confirm whether losses caused by the orbit distortions were responsible for the unusual BPM response.

Figures 5.6B and 5.6C show the reduced chi squared values for the linear fits of horizontal position vs. kick strength and vertical position vs.

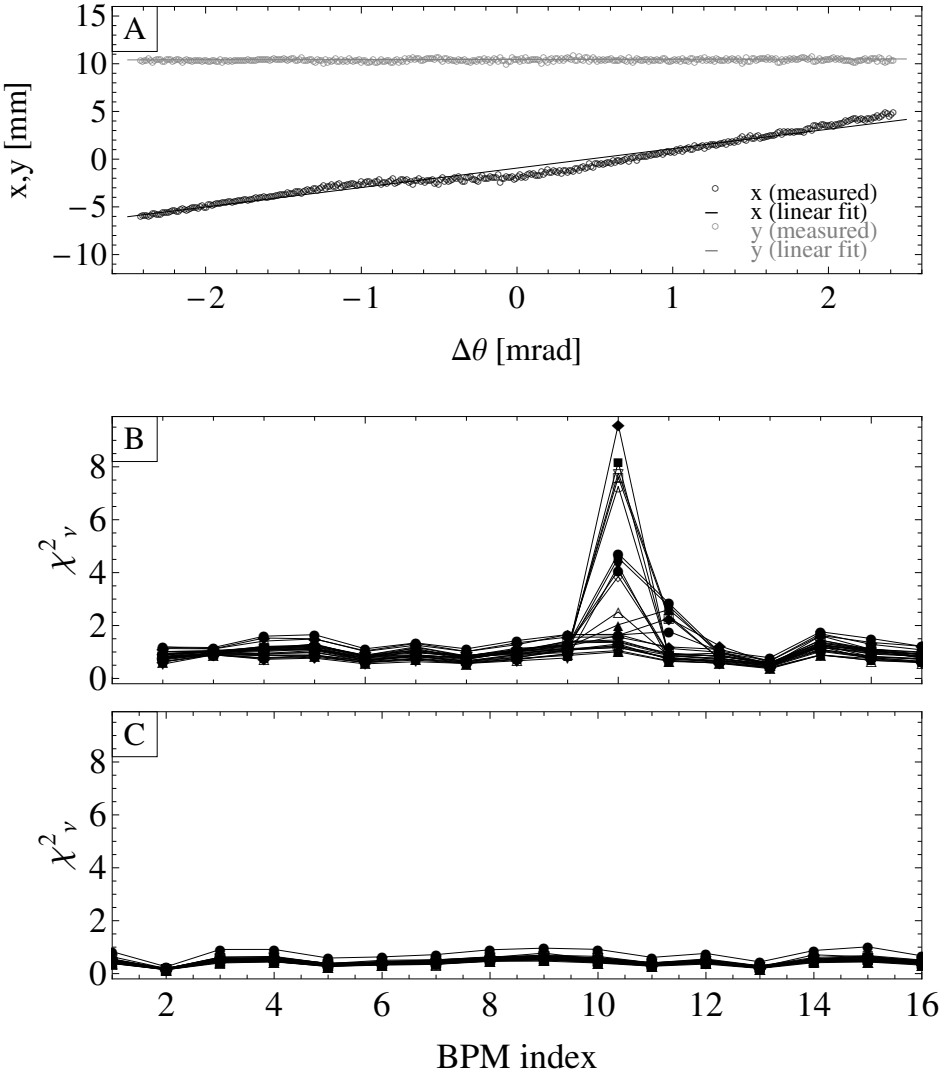

Figure 5.6: The horizontal (black circles) and vertical (gray circles) orbit positions measured with the BPM in period 10 as a function of kick strength. The black and gray lines are linear fits to the horizontal and vertical position vs. angular kick. The horizontal orbit response measured using this BPM is highly nonlinear. The 26 lines shown in (B) correspond to χ^2_ν for the linear fit of horizontal position vs. kick strength for each of the 26 dipoles, and (C) shows χ^2_ν for the linear fits of vertical position vs. kick strength. Horizontal BPMs in periods 10 and 11 were discarded because of the high values of χ^2_ν

kick strength. Each of the 26 traces corresponds to the fits to one of the 26 orbit correctors. For most BPMs the reduced chi squared value for the linear fit was close to one, indicating that a straight line was a good fit to the data. Measurements made with the horizontal BPMs in periods 10 and 11, which had high chi squared values, were discarded from the data set.

5.4 Application of LOCO Results

As was mentioned in Section 5.1, one of the main goals of LOCO analysis in the PSB is to characterize the distribution of focusing errors around the ring so that the lattice model may be made more accurate. Characterization of focusing errors is crucial for understanding the patterns and mechanisms of space-charge induced beam losses in the PSB because without these focusing errors in the model, multi-particle tracking simulations do not reproduce the observed patters of beam loss when the tune approaches a resonance. When the focusing errors found using LOCO are added to the model, the pattern of beam loss predicted by simulations closely resembles the observed pattern of beam loss.

Figure 5.7 shows the beam intensity as a function of time during the 160 MeV energy plateau in the beam. Thevertical tune is changed with time so that it approaches the half integer, which results in resonant growth of particle oscillation amplitude and beam loss [30]. The pink band shows the measured pattern of intensity as a function of time. The blue line is the result of a simulation with space charge (SC) effects included but no LOCO focusing

errors ($\Delta k_1 l$). The green line is the result of a simulation with no space charge effects included, but with LOCO focusing errors. The red line is the result of a simulation with both space charge effects and LOCO focusing errors included; in this case, the pattern of beam intensity vs. time closely resembles the measured values.

5.5 Summary

This chapter gave the results of optics measurements from LOCO in the CERN PS Booster. Orbit response measurements were carried out for all four rings of the PSB, and were repeated at multiple working points. The maximum beta beating in the machine is currently only about 5%, which is negligibly small. Although beta beating corrections are not necessary now, changes will be made to the lattice structure in the next few years which may introduce larger optics perturbations, so it is useful to have an optics measurement technique established so that beta beating corrections may be made in the future.

These orbit response measurements also provided an estimate of the distribution of focusing errors around the ring, which is useful for making beam dynamics simulations more accurate. The inclusion of these errors in simulating beam losses near the integer or half-integer resonances gave results that closely matched the observed beam loss in the machine. Understanding and accurately modeling beam dynamics at high intensities will be crucial in preparation for running the machine with nearly doubled intensity in the next

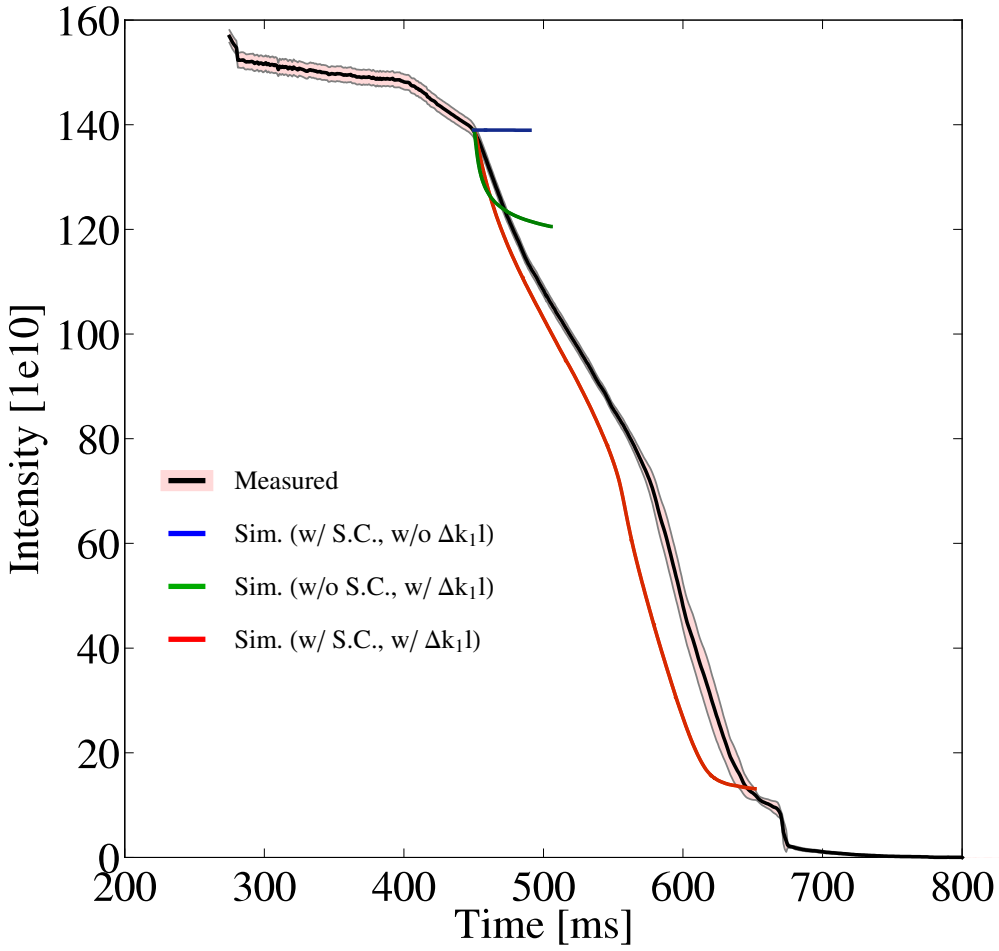

Figure 5.7: The beam intensity as a function of time when the vertical tune is near a half integer. The pink band shows the measured losses. The blue line is the result of a simulation with space charge (SC) effects included but no LOCO focusing errors ($\Delta k_1 l$). The green line is the result of a simulation with no space charge effects included, but with LOCO focusing errors. The red line is the result of a simulation with both space charge effects and LOCO focusing errors included. Image courtesy of V. Forte [30].

few years.

Chapter 6

Summary and Outlook

For physics research at the intensity frontier, it is necessary to maximize the number of particle collisions in a detector so that precise measurements of new particles and processes can be obtained within a reasonable amount of run time for the experiment. The collision rate is characterized by the luminosity, which is directly proportional to the number of particles in a beam and inversely proportional to the transverse size of the beam. Intensity and luminosity upgrades that are planned for both the CERN and FNAL accelerator complexes will require the Booster accelerators to accelerate more intense beams while maintaining a small beam size, and achieving this will require more precise control of the optics than was previously required in these machines.

The transverse motion of particles in an accelerator is controlled using a lattice of magnetic fields, which causes the ensemble of particles in a beam to undergo stable betatron oscillations around an ideal reference trajectory. The physical beam size is defined by both the beta function, which describes the maximum amplitude of the betatron oscillations as a funciton of longitudinal position, and the emittance. Imperfections in the focusing lattice cause a

distortion to the beta function which can be detrimental to beam quality for two reasons: irregularity in the beam size can lead to particles being lost in areas of the machine where the aperture is restricted, and beta function distortions combined with the highly nonlinear space charge forces among particles in an intense beam can lead to emittance dilution.

The beta function in an accelerator can be measured using the Linear Optics from Closed Orbits (LOCO) technique, in which the optical properties of the machine are inferred from the observed response of the closed orbit to dipole perturbations. We applied this technique in both the FNAL Booster and in the CERN PSB to make measurements of the beta function with much greater precision than had previously been possible in either machine. The ability to make precise optics measurements in either the FNAL Booster or the CERN PSB had previously been limited by the available hardware. When these machines were built, the intensity that they were expected to handle was at least an order of magnitude lower than the intensities that they will soon achieve. It was not necessary, when they were built, to include a system of corrector magnets that would allow for extremely precise measurement and correction of optics. An attempt was made in 2005 to measure optics in the FNAL Booster using LOCO, but because of the limited capabilities of the corrector packages available at the time, it was only possible to determine that the magnitude of focusing errors in the main magnets fell within the expected tolerances [31].

In the FNAL Booster, we successfully corrected the transverse coupling

using the results of LOCO analysis. The beta beating was measured to be as large as 30% near the beginning of the acceleration cycle, when the distortions caused by the extraction dogleg magnets are strongest. This beta beating was successfully corrected during machine studies. The next step for using these results to improve machine performance is to integrate the beta beating corrections into routine operations. This requires making changes to the hardware and software systems that control the corrector magnet packages in the machine, and these modifications are underway. Beta beating corrections alone did not reduce beam losses in the Booster, but this is not unexpected. Operations experts have empirically tuned numerous machine parameters to minimize losses, and this slow and careful tuning process will need to be repeated after beta beating corrections are implemented. One may expect that beam losses will be reduced after optics distortions are corrected and machine parameters such as closed orbit location are re-optimized.

In the CERN PS Booster, the optics measurements revealed that the beta function distortions are no more than about 5%, and presently this distortion does not seem to be large enough to cause any beam loss or emittance dilution. In the near future, however, the beam intensity will be approximately doubled and structural changes will be made to the machine's lattice so that an H- injection scheme can be implemented. These changes to the lattice may introduce perturbations to the beta function and the strong nonlinear space charge forces in the machine will exacerbate the effects of these perturbations, leading to beam loss and emittance dilution.

The procedures established in this dissertation will enable the machine optics in both the FNAL Booster and in the CERN PS Booster to be corrected as precisely as is necessary to maintain satisfactory beam quality after intensity upgrades are completed.

Appendix

Appendix 1

Hardware and software used for data collection and analysis in FNAL Booster and the CERN PS Booster

This appendix discusses the hardware and software used for collecting and analyzing data for optics measurements in the FNAL Booster and in the CERN PS Booster. This will include discussions of the corrector magnets and beam position monitors in each machine, and of the software used to facilitate data collection and analysis.

1.1 FNAL Booster multipole corrector packages

A system of corrector magnets is necessary in any accelerator in order to maintain beam stability, and if this system of magnets is strong and versatile enough it can also be an excellent tool for making optics measurements. Until several years ago, the FNAL Booster had a rather limited set of corrector magnets which were not strong enough to control the orbit at high energy. In anticipation of future higher-intensity operations, a set of 48 multipole corrector packages was installed in the FNAL Booster between 2007 and 2009. These magnets were intended to be powerful and versatile enough to be able

to meet any needs that may arise during the next decades of high-intensity operations. They have enough field strength and can slew fast enough to provide full control over the closed orbit, betatron tunes, and chromaticities throughout the acceleration ramp [12].

Figure 1.1 shows one of the FNAL Booster corrector packages before it was encased in a protective housing of epoxy and glass beads. The twelve sets of copper windings surrounding the twelve-poled steel core are powered in six circuits, arranged so that they produce six independently-controllable multipole fields: normal and skew dipole, quadrupole, and sextupole [32]. The strength of each multipole field as a function of current was measured on a test bench before the magnets were installed [26]. Each magnet package also contains an integrated beam position monitor (see Section 1.3).

Each of the six circuits in each of the 48 corrector packages is controlled through a CAMAC 473 card, which can be programmed with arbitrary current vs. time functions [33]. An example of the current vs. time function used during optics measurements was shown in Figure 4.1. The function is a linear interpolation between current settings specified for a set of predetermined time break points. In addition to this f(t) current ramp, each card can also be programmed with a constant scaling factor and with a constant DC offset. A controls system application allows the user to change a magnet's current ramp by entering new current values for each time break point in the ramp, or to change the DC offset or scaling factor. These settings can also be changed using Accelerator Command Language (ACL), a scripting language that allows

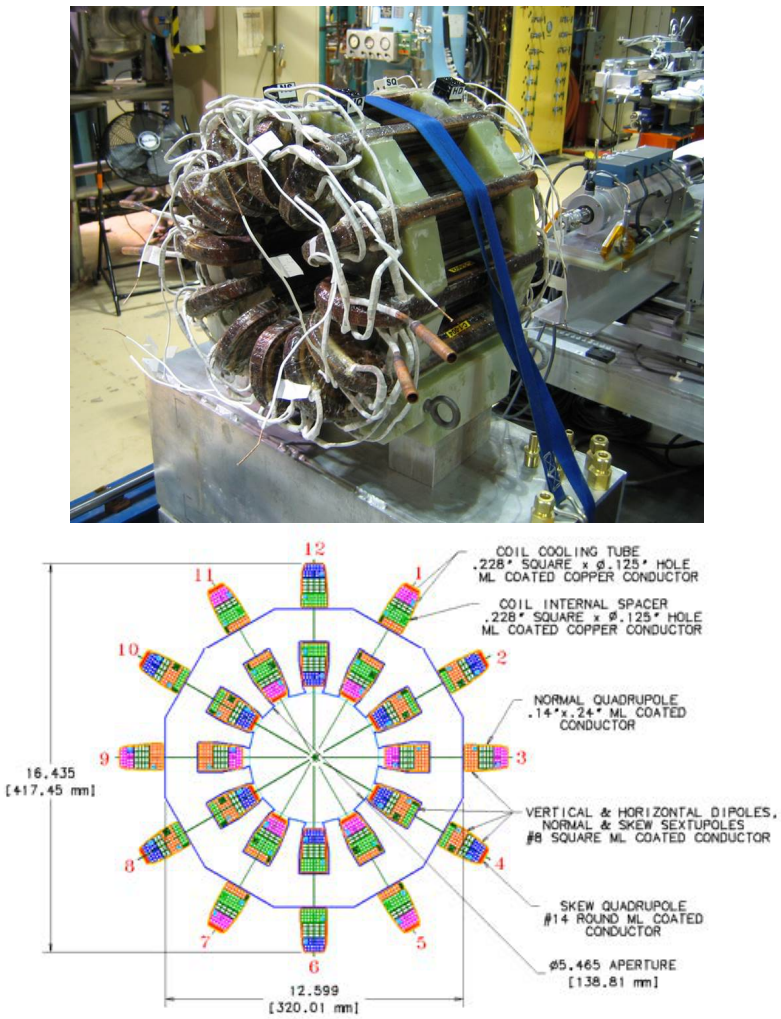

Figure 1.1: Top: One of the FNAL Booster's corrector magnet packages, before it was encased in a shell of epoxy and glass beads [32]. The twelve-pole steel core is wound with copper wire coils powered in six independent circuits, with the coils arranged such that each circuit produces an approximately pure multipole field. Bottom: Diagram showing how the various parts of the copper windings seen in the photo are grouped into six circuits, which circuits produce normal and skew dipole, quadrupole, and sextupole fields.

for full control of all hardware in the Booster (see Section 1.4.1). The settings for these magnets are defined separately for each event in the Booster's time line, meaning that magnet changes can be made during beam pulses that are dedicated to machine studies, while beam pulses that will be delivered to experiments remain unaffected. The large number of dipole and quadrupole magnets, along with the flexibility in how they can be powered, made them ideally suited for making optics measurements using LOCO or K-modulation methods.

1.2 CERN PS Booster correctors

The set of corrector magnets in the CERN PSB was installed in the early 1970's, and at that time it was not deemed necessary to have a system as sophisticated at that which is now in the FNAL Booster [34]. Each ring contains four pairs of normal quadrupoles and two pairs each of skew quadrupoles, normal sextupoles, and normal octupoles. Each of these pairs of multipole magnets is powered together in series. There is also a set of eight skew quadrupole, sixteen normal sextupole, and sixteen normal octupole correctors, with all eight or sixteen magnets of a given type being powered in series on a single circuit. Prior to the Long Shutdown of 2013-2014 the software controlling these magnets did not allow for separate settings for different beam events, so it was not possible to use for beam dynamics studies without disturbing batches of beam that were to be delivered to experiments. The limited number of available magnets, along with the limitations in how these magnets

were powered, did not allow for optics measurements using K-modulation in the PSB.

The dipole correctors in the PSB are more numerous and more flexible than the higher-order multipole correctors, with each ring containing thirteen horizontal and thirteen vertical dipole correctors. These magnets are all individually controlled by an FGC3 function generator, which allows the user to specify any arbitrary current vs. time function. Each of these dipole correctors is powered individually, and the function can be changed for different events within the timeline, so these magnets provide adequate flexibility for making optics measurement using the LOCO method in the PSB.

1.3 Beam Position Monitors

A beam position monitor (BPM) consists of a set of four pickups running parallel to the beam pipe, as shown in Fig. 1.2. The upstream ends of the electrodes have ports which lead out of the beam pipe, and the downstream end is terminated. When the beam passes, its image charge induces a voltage in each electrode. The Fermilab Booster is equipped with 51 BPMs which read the position in both the horizontal and vertical planes. 48 of these BPMs are integrated into the corrector magnet packages which are located in each long and short drift section, and the additional three BPMs are located in the extraction and collimation regions. Each of the CERN PS Booster's four rings is equipped with sixteen BPMs, which are located just downstream of the first magnet of the focusing triplet in each period.

The difference in voltages on a pair of parallel electrodes depends on both the beam's position and its intensity, and the sum of the voltages depends only on the beam intensity. The beam position in a given plane, normalized for variation in beam intensity, is calculated as

$$z = C \cdot \frac{V_A - V_B}{V_A + V_B} \tag{1.1}$$

where V_A and V_B are the voltages on the outer and the inner plates (for the horizontal plane) or on the upper and the lower plates (for the vertical plane). C is a scaling factor which is determined by the geometry of the BPM.

Figure 1.3 shows the voltage signals from the horizontal pair of pickups in one BPM in the FNAL Booster, read directly from the plates using an oscilloscope. Figure 1.3(A) shows a time duration slightly longer than the revolution frequency of the beam. Eighty-one of the 84 RF buckets are filled, and a voltage spike is visible when each of these 81 bunches passes the BPM. Figure 1.3(B) is a close-up of the area bounded by a rectangle near 0.2 μs in Figure 1.3(A). This figure shows the structure of the signal as four bunches pass the BPM with a spacing of 19 ns, or a frequency of 52 MHz. As a bunch approaches the upstream end of the BPM, part of the signal induced on the electrode by the image charge propagates out of the upstream port, which is seen as a positive voltage spike in Figure 1.3(B). In addition, part of the signal travels along the pickup, is reflected at the terminated downstream end, and then propagates with opposite polarity out of the upstream port, causing the negative voltage spikes seen in Figure 1.3(B).

Figure 1.2: Beam Position Monitor (BPM) from the FNAL Booster, consisting of four pickup electrodes running parallel to the beam pipe. The upstream ends of the electrodes have ports which lead out of the beam pipe, and the downstream end is terminated. When the beam passes, its image charge induces a voltage in each electrode. The difference in voltage on a pair of electrodes on opposite sides of the beam pipe is proportional to the transverse offset of the beam in that plane.

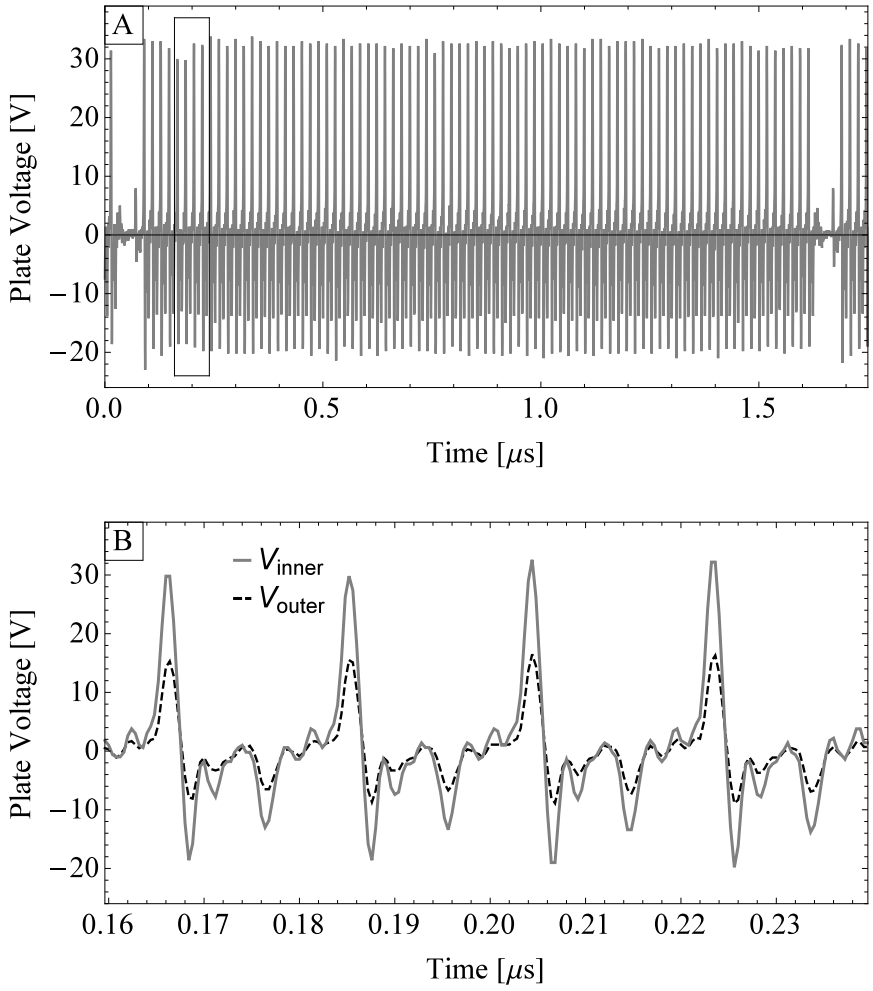

Figure 1.3: Voltage signals from the horizontal pair of pickups of one BPM in the FNAL Booster, read directly from the plates using an oscilloscope. (A) shows the voltage signal during a period of time slightly longer than the revolution period of the beam. Eighty-one of the 84 RF buckets are filled, and a voltage spike is visible when each of these 81 bunches passes the BPM. (B) is a close-up of the area bounded by a rectangle near $0.2\mu s$ in (A), showing the structure of the signal as four bunches pass the BPM. As a bunch approaches the upstream end of the BPM part of the signal propagates out of the upstream port, which is seen as a positive voltage spike in (B). Part of the signal travels along the pickup, is reflected at the terminated downstream end, and then propagates out of the upstream port with opposite polarity, creating the negative voltage spikes in (B).

The signal from each of the four ports will then go on to be processed in an RF module, where it is passed through a narrow-band filter to extract the components near the 52 MHz bunch frequency before the sums and differences of the voltages are calculated [35]. The relationship between the sum and difference signals and the transverse offset was measured on a test bench before the BPMs were installed. In these measurements, a current-carrying wire was used to simulate the proton beam, and the voltage response on each plate was measured as a function of the position of the wire. This measured relationship between beam position and V_{diff}/V_{sum} is written into a look-up table which is used to convert the BPM sum and difference signals to the corresponding position [36].

1.4 Controls system scripting for data acquisition

Beam-based measurements are more efficient if controls system scripting tools are available, allowing repetitive measurements to be made more quickly and with less chance of error. In this section we discuss the scripting of machine studies in the FNAL Booster and in the CERN PS Booster. All of the scripts used to collect the data discussed in this dissertation were written by this author.

1.4.1 Scripting with Accelerator Command Language in the FNAL Booster

Accelerator Command Language (ACL) is a scripting language that was developed for use in the FNAL accelerator complex [37]. It allows the user to either read or set values to any device in the accelerator control system, including beam position monitors, magnets, and any other hardware or diagnostic equipment in the machine. It also allows for control structures such as loops and if-then statements, so it can efficiently loop through repetitive measurements and handle any errors or exceptions that occur during the execution of a script. ACL was designed to be user-friendly and accessible to anyone with basic programming knowledge; no specialized knowledge of the controls systems is required.

Most of the beam-based measurements done in the Booster were highly repetitive, requiring the user to change the setting of a device (such as a dipole or quadrupole magnet), read the output from a set of diagnostic devices (such as beam position monitors) for several beam pulses, and then restore the original settings of the device that was changed. For LOCO measurements, for example, this process must be repeated 192 times because there are 96 dipole orbit corrector magnets, and positive and negative current bumps must be made for each magnet. These measurements were accomplished easily and relatively quickly in the Booster, with approximately two hours being required to make a full set of orbit response measurements. These measurements were all made using a special beam event dedicated to machine studies, which was

inserted into the Booster's time line between beams that were delivered to experiments.

The ACL scripts used for orbit response or tune response measurements have the same basic structure, looping through the following procedure for each corrector magnet in the machine:

1. Read current vs. time settings from CAMAC 473 card for the given magnet (for the beam dedicated to machine studies).

2. Calculate desired new current vs. time settings, based on user-supplied value for the magnitude of magnet current bumps to be applied.

3. Write new current vs. time settings to CAMAC 473 card (for the machine studies beam only).

4. Read BPM output (for the machine studies beam) and writes data to text file.

5. Continue recording BPM data each time the machine studies event occurs, until some user-defined number of beam pulses has been recorded.

6. Write the original current vs. time settings back to the CAMAC 473 card, then repeat for the next magnet.

Since ACL is so powerful, providing the ability to manipulate any and all hardware in the machine, care must be taken to prevent either damaging the

machine or accidentally leaving it in some unknown state. The following precautions are written into the ACL scripts to ensure the safety of the machine, and to ensure that the data collected is of good quality:

- The beam intensity is read each time the machine studies event is played. If the injection intensity is below a certain threshold, indicating that there is no beam in the machine, then the script pauses and resumes when the beam returns. This ensures that good data is eventually recorded even if beam is temporarily unavailable.

- If the intensity drops too much during the acceleration cycle, i.e. if a certain magnet current bump causes excessive losses, then the magnet current bump is removed and the loop continues to the next magnet. This prevents damage from the machine due to excessive losses. Since closed orbit position and betatron tune are affected by changes in beam intensity, this check also helps to exclude invalid data points.

- If a fatal error is returned by any device, i.e. if the BPMs fail to read properly, initial settings will be restored to magnets before exiting.

ACL scripts were also used at the start of the machine studies to read the values of all relevant machine parameters, ensuring that the state of the machine was well-known. Parameters such as the settings of all magnets in the machine, the voltages of RF cavities, and the radial feedback settings were were then incorporated into the lattice model of the machine so that it described the real machine as precisely as possible.

ACL scripts were also used to control hardware in ways that the usual console applications were not equipped to handle. For example, even though it is possible to make each of the new quadrupole corrector magnets follow a unique current vs. time ramp, this functionality is not yet used in normal operations. In order to make each magnet follow a unique current ramp, which was necessary for coupling corrections and for beta beating corrections, an ACL script was used to write the new current vs. time ramps to the CAMAC 473 cards for each magnet. The console application is currently be upgraded to allow the quadrupole magnets to be set individually, which will facilitate the incorporation of these beta beating and coupling correction methods into normal operations.

1.4.2 Scripting with MATLAB and JAPC in the CERN PS Booster

The CERN PS Booster does not have a native scripting language which was designed to provide full control over all devices in the machine. However, some tools do exist that can be used to facilitate machine studies. The Java API for Parameter Control, or JAPC, is a framework developed at CERN which can be used to build Java applications that control accelerator devices [38]. MATLAB classes have been written which interact with JAPC, allowing the user to read and set accelerator devices using a MATLAB script [39]. These tools do not amount to a self-contained, user-friendly system, though, and a significant amount of detailed knowledge of the controls system is still needed in order to make full use of these scripting tools.

Given the complexity of the scripting tools and the relatively small set of measurements involved, I did not attempt to fully automate the orbit response measurement process. Instead I wrote MATLAB scripts which retrieved data from all relevant devices (beam position, magnet current, beam intensity, etc.) while changes to the dipole magnet current adjustments were made manually, using the console application designed for this purpose. This process was less efficient than if the magnet settings were changed automatically using a scripting language, but the use of the MATLAB/JAPC tools to retrieve data from the BPMs and other diagnostic devices still saved a considerable amount of time.

1.5 Data analysis

This section discusses the steps involved in extracting useful information about the optics from the raw data collected during machine studies in the FNAL Booster and in the CERN PS Booster. Unless otherwise specified, the data analysis was done by and the codes used were written by this author.

1.5.1 LOCO

The first step in data analysis for LOCO was to make a linear fit of the measured beam position vs. kick strength for all dipole-BPM pairs in the machine, which was done in Mathematica. Figure 3.2 shows an example of the raw position measured as a function of dipole kick strength and the linear least-squares fit in the FNAL Booster. The slope and standard error of the

linear fit for all BPM-dipole pairs (i.e. the measured Orbit Response Matrix) were then written into a text file in a format suitable for the next step of the analysis.

The analysis of the measured Orbit Response Matrix was done following the LOCO method developed by Safranek [21]. For the FNAL Booster, the LOCO analysis was implemented using scripts written in tcl, Octave, and the lattice modeling code *elegant* [40] by A. Petrenko. To improve processing time and integrate better into the controls system, these scripts were later converted to MADX and C++ by C. Y. Tan [41]. For the CERN PSB, the LOCO analysis was implemented using scripts written by this author in Python and the lattice modeling code MADX [42].

In both of these implementations of LOCO, the method is the same. First, the magnet settings from the real machine are written into the lattice model of the machine so that the initial model is as accurate as possible. Then the orbit response matrix is calculated using this model, as well as the Jacobian of this orbit response matrix (i.e. change in orbit response per change in variable model parameter, such as focusing magnet strength or dipole calibration). Then the Jacobian matrix is inverted using Singular Value Decomposition in order find the set of variable model parameters that minimizes the difference between the measured and the calculated orbit responses (see Section 3.1.3). This new set of parameters is then placed in the lattice model, and the fitting is iterated to ensure that the solution converges. Once the fit has converged, the optics parameters given by the calibrated model are assumed to correspond

to the optics parameters of the real machine.

1.5.2 K-modulation

The data analysis for K-modulation measurements in the FNAL Booster was much simpler than the LOCO analysis. The first step was to calculate the betatron tunes from the measured beam trajectories using the FFT algorithm SUSSIX [24], developed by F. Schmidt and R. Bartolini. In order to facilitate this step, the ACL script used for K-modulation measurements writes the beam position data to a file with a format appropriate for SUSSIX. The tunes output from SUSSIX were then analyzed in Mathematica, where a linear fit of betatron tune vs. quadrupole magnet strength was done. An example of the measured tunes vs. quadrupole strength and the linear fit was shown in Figure 3.11. The value of the beta function at the location of each quadrupole was then calculated from the slope of the linear fit, as described in Section 3.2.

Bibliography

[1] S. Heinemeyer et al. Handbook of LHC Higgs Cross Sections: 3. Higgs Properties. *arXiv:1307.1347*, 2013.

[2] L. Rossi and O. Brning. High Luminosity Large Hadron Collider A description for the European Strategy Preparatory Group. Technical Report CERN-ATS-2012-236, CERN, Geneva, 2012.

[3] W.J. Stirling. private communication.

[4] P. Limon. The optimum energy of the really large hadron collider sited at Fermilab. *eConf*, C960625, 1996.

[5] R. Webber. A Plan for Delivery of 8-GeV Protons through 2025 at Fermilab. Technical Report Beams-doc-3781-v2, FERMILAB, 2011.

[6] G. Rumolo, S. Aumon, W. Bartmann, H. Bartosik, A. Huschauer, V. Raginel, and H. Timko. Summary of the LIU beam studies review. Technical Report CERN-ATS-Note-2012-083 PERF, CERN, 2012.

[7] F.G. Garcia and W. Pellico. FNAL Proton Source High Intensity Operations and Beam Loss Control. *arXiv:1409.0039*, 2012.

[8] E. Prebys, C. Ankenbrandt, W. Chou, A. Drozhdin, P. Kasper, J. Lackey, N. Mokhov, and R. Webber W. Pellico, R. Tomlin. Increasing the in-

tensity of the fermilab booster. In *Proc. Particle Accelerator Conference (PAC'03)*, pages 2936–2938. JACoW, 2003.

[9] B. Worthel. The Booster Rookie Book. Technical Report Beams-doc-1022-v1, FERMILAB, 2004.

[10] E. L. Hubbard. Booster synchrotron. Technical Report FERMILAB-TM-0405, FERMILAB, 1973.

[11] P. Yoon, P. Kaspers, B. Oshinowo, and J. Lackey. The understanding and analysis of the booster magnet survey data. Technical Report Beams-doc-2491-v1, FERMILAB, 2006.

[12] E.J. Prebys, C.C. Drennan, D.J. Harding, V. Kashikhin, and J.R. Lackey. New corrector system for the Fermilab Booster. In *Proc. Particle Accelerator Conference (PAC'07)*, pages 467–469. JACoW, 2007.

[13] K. Hanke and K. Schindl. The PS Booster hits 40. *CERN Cour.*, 52(7):33–37, 2012.

[14] Alfred M Asner, Giorgio Brianti, M Giesch, and K D Lohmann. The PS booster main bending magnets and quadrupole lenses. In *3rd International Conference on Magnet Technology*, 1970.

[15] D. Edwards and M. Syphers. *An Introduction to the Physics of High Energy Accelerators*. John Wiley & Sons, Inc., 1993.

[16] J. Tanabe. *Iron Dominated Electromagnets: Design, Fabrication, Assembly and Measurements*. World Scientific Pub. Co. Inc., 2005.

[17] K. Wille. *The Physics of Particle Accelerators: An Introduction*. Oxford University Press, 2001.

[18] B. C. Brown. Field quality issues in iron dominated dipoles at low fields. *eConf*, C960625, 1996.

[19] S. Y. Lee. *Accelerator Physics*. World Scientific Pub. Co. Inc., 2004.

[20] F. Willeke and G. Ripken. *Methods of beam optics*. DESY, Hamburg, 1988.

[21] J. Safranek. Experimental determination of storage ring optics using orbit response measurements. *Nuclear Instruments and Methods in Physics Research Section A: Accelerators, Spectrometers, Detectors and Associated Equipment*, 388(12):27 – 36, 1997.

[22] M. Minty and F. Zimmermann. *Measurement and Control of Charged Particle Beams*. Springer, 2003.

[23] W. Press, S. Teukolsky, W. Vetterling, and P. Flannery. *Numerical Recipes 3rd Edition: The Art of Scientific Computing*. Cambridge University Press, 2007.

[24] R. Bartolini and F. Schmidt. SUSSIX: A computer code for frequency analysis of non-linear betatron motion. Technical Report CERN SL/Note 98-017 (AP), CERN, 2005.

[25] X. Huang. *Beam Diagnosis and Lattice Modeling of the Fermilab Booster*. PhD thesis, Indiana State University, 2005. FERMILAB-THESIS-2005-29.

[26] E.J. DiMarco, D J Harding, V.S. Kashikhin, et al. Test results of the AC field measurements of fermilab booster corrector magnets. In *Proc. European Particle Accelerator Conference (EPAC'08)*, pages 2347–2349. JACoW, 2008.

[27] P. Arpaia, Marco Buzio, Giancarlo Golluccio, and G. Montenero. Eddy current modeling and measuring in fast-pulsed resistive magnets. In *Instrumentation and Measurement Technology Conference (I2MTC), 2010 IEEE*, pages 1078–1081, 2010.

[28] J. Amundson, J. Lackey, P. Spentzouris, G. Jungman, and L. Spentzouris. Calibration of the FNAL booster ionization profile monitor. *Phys.Rev.ST Accel.Beams*, 6:102801, 2003.

[29] W. Chou, A. Drozhdin, P. Lucas, and F. Ostiguy. Fermilab booster modeling and space charge study.

[30] V. Forte, E. Benedetto, and M. McAteer. CERN PS Booster space charge simulations with a realistic model for alignment and field errors. In *Proc. 5th International Particle Accelerator Conference (IPAC'14)*, pages 1624–1626. JACoW, 2014.

[31] X. Huang, J. Safranek, and G. Portmann. LOCO with constraints and improved fitting technique. *ICFA Beam Dyn.Newslett.*, 44:60–69, 2007.

[32] A. Makarov et al. Design and fabrication of a multi-element corrector magnet for the Fermilab Booster. *IEEE Trans. Appl. Supercond.*, 18:334–337, 2008.

[33] D. McArthur. CAMAC 473 quad ramp controller. Technical Report Beams-doc-2361-v3, FERMILAB, 2007.

[34] G. Baribaud, P. Bossard, G. Nassibian, K. H. Reich, K. Schindl, J. Vlogaert, and F. Vlker. The new PSB multipole magnet system. Technical Report CERN-PS-BR-77-42, CERN, 1977.

[35] R.E. Shafer, R.C. Webber, and T.H. Nicol. Fermilab energy doubler beam position detector. *IEEE Transactions on Nuclear Science*, 28(3):2290–2292, 1981.

[36] R. Webber. Calibration of the booster BPM system. Technical Report Beams-doc-2085, FERMILAB, 1986.

[37] B. Hendricks. ACL introduction. Technical Report Beams-doc-4091-v2, FERMILAB, 2012.

[38] V. Baggiolini et al. JAPC - the Java API for Parameter Control. In *Proc. International Conference on Accelerator and Large Experimental Physics Control Systems (ICALEPCS'05)*, 2005.

[39] G. Sterbini and D. Gamba. Private communication.

[40] M. Borland. Recent progress and plans for the code *elegant*. In *Proc. International Computational Accelerator Physics Conference (ICAP'09)*, 2009.

[41] C.Y. Tan. LOCO for Booster. Technical Report Beams-doc-4536-v1, FERMILAB, 2014.

[42] W. Herr and F. Schmidt. A MAD-X Primer. Technical Report CERN-AB-2004-027-ABP, CERN, 2004.